Semi-Stationary Shoulder Bobbin Tool (S^3BT): A New Approach in High Speed Friction Stir Welding

Vom Promotionsausschuss der
Technischen Universität Hamburg - Harburg
zur Erlangung des akademischen Grades
Doktor-Ingenieur (Dr.-Ing.)
genehmigte Dissertation

von
Peer-Jorge Scupin

aus
Kiel

2015

Gutachter:

Prof. Dr.-Ing. Norbert Huber

Prof. Dr.-Ing. Michael Rethmeier

Vorsitzender des Prüfungsausschusses:

Prof. Dr.-Ing. Wolfgang Hintze

Tag der mündlichen Prüfung:

29.04.2016

Zusammenfassung

Das Doppelschulterwerkzeug für Rührreibschweißen wurde bereits im originalen Patent W. Thomas et al. in 1991 eingeführt. Die beiden Werkzeugschultern werden durch einen Stift verbunden, der zum einen als Konstruktionselement dient und zum anderen in das Material eindringt und den Werkstoff transportiert. Dabei rotieren die Schultern und der Stift mit derselben Drehzahl in eine Richtung. Durch diese Anordnung benötigt der Prozess keine Unterlage für die Abstützung der Prozesskräfte und ist zum Verschweißen von Profilen geeignet. Da die Kräfte für den Fügeprozess von den Schulterelementen aufgebracht werden, können die Anforderungen an die Steifigkeit des Handhabungssystems reduziert werden. Diese Art Rührreibschweißen wurde in der Luftfahrt- und Industrie für Schienenverkehr mit begrenztem Erfolg eingeführt. Eine der größten Herausforderungen des Konzepts ist der erhöhte Wärmeeintrag durch die beiden Schulterelemente in Verbindung mit der begrenzten Wärmeabführung durch die reduzierte Spannvorrichtung. Dieses führt zu einer Verschlechterung der Microstruktur des verschweißten Materials und als Folge zu schlechteren mechanischen Eigenschaften der Verbindung.

In jüngerer Vergangenheit wurde eine Rührreibschweißvariante vorgeschlagen, um diesen Nachteilen zu begegnen. Diese Studie beschäftigt sich mit unterschiedlichen Konzepten für das Rührreibschweißen mit geregelten Doppelschulterwerkzeugen. Unter den vier getesteten Varianten zeigte das semi-stationäre Doppelschulterwerkzeug gute Resultate in der Reduktion der auftretenden Reaktionskräfte in Kombination mit industrietauglichen Schweißgeschwindigkeiten bei reduziertem Wärmeeintrag.

Für die Schweißversuche wurden ein neues, voll geregeltes Handhabungssystem und Schweißwerkzeuge entwickelt und gebaut. Die Entwicklung der Werkzeuge wurde von CFD-Simulation begleitet. Für die Zusammenführung der Versuchsergebnisse mit den Ergebnissen aus der Simulation wurde ein analytisches Modell eingeführt, welches die Energien in der Rührzone des Werkzeuges betrachtet. Die eingeführten analytischen und numerischen Modelle wurden in den Versuchen validiert. Darüber hinaus wurden die Schweißnähte mechanisch untersucht.

Im Rührreibschweißen mit Doppelschulterwerkzeugen wurde die kinetische Energie des Materialflusses auf der Gegenlaufseite des Werkzeuges als kritische Größe in der Simulation für die experimentelle Durchführbarkeit erkannt. Die Untersuchungen deuten darauf hin, dass diese Energie den Materialfluss initialisiert und zwingend notwendig für den stabilen Schweißprozess ist. Mit diesem Wissen konnten Schweißgeschwindigkeiten von 3000 mm/min erreicht werden. Diese Geschwindigkeit repräsentiert Faktor fünf der maximalen Geschwindigkeiten in der Literatur. Dabei wurden eine durchschnittliche Zugfestigkeit von 92% des Grundmaterials und maximale Werte von mehr als 95% zum Grundmaterial nachgewiesen. Darüber hinaus konnten die Schwingungsamplituden reduziert werden. Weil die mittleren Kräfte nun im Bereich von Knickarmrobotern liegen, erweitert diese neue Doppelschulterwerkzeugvariante den industriellen Einsatzbereich.

Abstract

The Bobbin Tool Friction Stir Welding (BT-FSW) concept has been mentioned in the original FSW patent by W. Thomas et al. in 1991. This original concept was based on a double shoulder tool using the probe as an assembly element. Both shoulder and probe rotated in the same direction and with the same speed. BT-FSW does not require backing bars and is ideal for hollow profiles. Moreover, the process forces required for the consolidation of the joint are delivered by the two shoulders, reducing the mechanical requirements of the handling system. This form of BT-FSW has been employed with limited success in space and railway industries. The main limitation of the original concept was the excessive heat generated by both shoulders combined with limitations in heat extraction from the joint area. This led to an excessive degradation of the joint microstructure and a consequent loss in mechanical properties.

More recently a variant of the BT-FSW process has been proposed, aiming at a reduction of the heat input. From this starting point, the present study reports results of preliminary experiments with different approaches of self-reacting BT-FSW. Among the four new tested process variants, the Semi-Stationary Bobbin Tool (S^3BT) process variant has shown good results in reducing handling forces in combination with considerable high welding speeds and low energy inputs.

A new fully controlled and unique experimental BT-FSW system with a new set of welding tools was created for the experimental programme. The development of tool designs was supported by CFD simulation with implemented viscosity as a function of shear rate and temperature. To correlate the experiments with simulation results, an analytical model was introduced, which balances energy fluxes during welding processes. The analytical and numerical modelling has been validated by the welding experiments. The joints have been subjected to mechanical testing.

In BT-FSW process variants, the mechanical power of the incoming kinetic energy of the mass flows into the weld zone has been identified as a critical value in the modelling to indicate the experimental feasibility. With this knowledge a welding speed of 3000 mm/min has been achieved. This speed represents factor five to the reported values in literature. Mechanical testing showed average ultimate tensile strength of 92% of the base material and maximum archived tensile strength of 95%. While increasing the welding speed, the amplitudes of forces have been reduced. Since the mean values of the process forces are in the present range of articulated arm robots, this new BT-FSW variant broadens the field of industrial application of the process.

Symbols and Abbreviations

3D	Three Dimensional
A	Material parameter for aluminium alloys
A_{adj}	Adjunct matrix
A^{2}SLM	Asymmetric Analytic Shear Layer Model
AS	Advancing Side
ASLM	Analytic Shear Layer Model
BC	Boundary Conditions
β	Rotational angle around the tool z-axis
BT	Bobbin Tool
BT-FSW	Bobbin Tool Friction Stir Welding
CFD	Computational Fluid Dynamics
CNC	Computational Numeric Control
C_p	Specific heat capacity
δ	Contact state variable
φ_{axis}	Angle of the fifth robotic axis
φ_{WCS}	Angle of the work piece coordinate system
φ_{weld}	Angle of the welding direction
Diameter 1	Diameter through SZ in the centre of the probe
Diameter 2	Diameter through SZ on the trailing side of the probe
DP	Decentralized Peripherals
dr	Normal distance to the probe surface
dz	Normal distance to the shoulder surface
$\dot{\bar{\varepsilon}}$	Effective strain rate
$\dot{E}_{kin2}$	Kinetic energy flow of $\dot{m}_2$
$\dot{E}_{kin3}$	Kinetic energy flow of $\dot{m}_3$
F	Force Vector
F_{gap}	Gap force in between shoulders of the BT
FSW	Friction Stir Welding
$F_{s\,Nom\,i}$	Nominal Gap Force i
$F_{s\,max}$	Maximal Gap Force
F_x	Force in x-direction; against welding direction
F_y	Force in y-direction; perpendicular to welding direction
$\vec{g}$	Gravitational vector
$\dot{\gamma}$	Shear rate
HAZ	Heat Affected Zone
HMI	Human Machine Interface
HZG	Helmholtz-Zentrum Geesthacht GmbH
$\sinh^{-1}$	inverse hyperbolic sin law
k	Thermal conductivity
L	Representative length of Reynolds number
ln	natural logarithm
$\dot{m}_1$	Incoming mass flow of material to be welded
$\dot{m}_2$	Mass flow on the AS in counter direction to incoming $\dot{m}_1$
$\dot{m}_{3\,deposit}$	Part of $\dot{m}_3$ deposited on the trailing side of the probe
$\dot{m}_3$	Mass flow passing on the RS

μ	Coulomb friction coefficient
η	viscosity
n	Stress exponent
$\vec{\nabla}$	Nabla operator
NC	Numeric Control
n_i	Rotational speed i
ω	Angular velocity
ω_{matrix}	Angular velocity of the material matrix
ω_{tool}	Angular velocity of the tool
p	Pressure
$p^{`}$	Transformed vector
PID	Proportional–Integral–Derivative
PLC	Program Logic Controller
Q	Heat
Q_a	Activation energy for high-temperature deformation
q_l	Line-energy
q_{total}	Total heat input
R	Gas constant
R_*	ASLM variable: shear layer outer boundary radius
R_{Probe}	Radius of probe
$R_{sl\,max}$	Upper limit for variable shear layer radius
$R_{sl\,\max AS}$	Upper limit for variable shear layer radius on AS
$R_{sl\,\max RS}$	Upper limit for variable shear layer radius on RS
$R_{sl\,min}$	Lower limit for variable shear layer radius
$R_{sl}(\beta)$	Variable shear layer radius
Re	Reynolds Number
R_{Ref}KE	Relative to Reference Kinetic Energy
R_{Rot}KE	Relative Rotating Kinetic Energy
ρ	Normalized coordinates of ASLM
ρ	Density
RPM	Rotation Per Minute
RS	Retreating Side
S^3BT	Semi-stationary Shoulder Bobbin Tool
S^3BT-FSW	Semi-stationary Shoulder Bobbin Tool Friction Stir Welding
$s_{i\,max}$	Maximum limit of controlled gap size
$s_{i\,min}$	Minimum limit of controlled gap size
σ	Tensile stress
$\bar{\sigma}$	Flow stress
SLS	Stationary Lower Shoulder
SRBT	Self-reacting Bobbin Tool
SRBT–6 mm	Conventional SRBT process variant with a 6 mm probe diameter
SRBT–7 mm	Conventional SRBT process variant with a 7 mm probe diameter
SSBT	Stationary Shoulder Bobbin Tool
SSBT-stepped	SSBT process variant with the stepped probe design
SSBT-straight	SSBT process variant with the straight probe design
SSFSW	Stationary Shoulder Friction Stir Welding
SUS	Stationary Upper Shoulder
SZ	Stirred Zone
T805	PKM T805 parallel kinematic robot
T	Temperature

t^*	Frozen time of the stationary “Frozen Rotor Study”
τ	Shear stress
$\tau_{friction}$	Shear stress induced by friction
τ_{yield}	Shear stress as a function of the yield stress of the material
t_i	Input parameter time for welding spindle
TMAZ	Thermo-mechanically Affected Zone
T_p	Thickness of the work piece
$\vec{u}$	Velocity in x-direction
$\vec{U}$	Velocity in direction of welding speed
UTS	Ultimate tensile strength
$\dot{V}$	Volume flow
v_{matrix}	Velocity of the material matrix
v_{tan}	Defined orbital velocity from analytical shear layer model
v_{tool}	Orbital velocity of the tool
WCS	Work Piece Coordinate System
Z	Zener-Hollomon parameter
ζ	Normalized coordinates of ASLM

Contents

1. Introduction and Motivation

Friction Stir Welding (FSW) is a solid state welding process invented in 1991 by Wayne Thomas [2, 3]. Since then, the process has been further developed and derivations have been invented. Depending on the configuration, the process can have great advantages compared to fusion welding. The heat input can be reduced and, therefore, the thermal degradation of the material in the weld zone is lowered. Friction stir welds have usually mechanical properties close to the base material. This is reflected through superior behaviour in tensile and fatigue testing. Furthermore, the FSW process allows to weld materials which are not suitable for fusion welding, and also to produce dissimilar welds.

As an ongoing megatrend, lightweight design in the transportation industry is demanding new approaches. Reducing weight is recently accomplished by smart material mix applications. With the use of different materials, new joining techniques became focus of the industry. While traditional joining techniques are focused on cycle time, robustness and cost efficiency, new demands require also environmentally friendliness and low energy. Friction stir based techniques fulfil these new demands, as well as produce welds with superior mechanical properties according to static and fatigue strength, hardness and ductility. The flexibility of welding dissimilar and non-weldable materials also becomes an option through these processes.
On the downside, the introduction of the new processes into the automotive industry is limited at the time. Exotic high class sports cars, such as the Audi R8, the Mercedes SL and the Ford GT40 contain some structural elements produced by the FSW process. Even though the process can be considered cost saving due to no use of consumables during the welds, especially the cost intensive and large equipment in combination with the limited welding speeds are keeping the process away from large volume production in the automotive industry. As one step to solve these limitations the KR500 Kuka robot equipped with DeltaN FSW technology was introduced into the market in 2012 [4]. With this handling system familiar to bigger production sites, the FSW process was applied in large scale production by Apple Inc. for computer housing [5]. This example shows how high the dependency of the successful application is on a turnkey ready solution of familiar handling equipment. Yet, the applicability of the DeltaN solution is limited, because the forces are still high and the tolerances of the work pieces are too demanding.

For increasing the application of FSW in large scale production, a handling system which is cheap and reliable to industry must be capable to conduct the FSW process without limitations. Regarding this purpose, there is no adequate process variant available at the moment. Either the forces are too high for the handling system, the welding speeds are limited or the application itself is limited. Basically it is necessary to reduce the forces to the range of articulated robots, and at the same time achieve high welding speeds. One approach to reduce forces is the bobbin tool FSW process variant. With this tool concept the axial forces which are necessary to consolidate the weld are applied by the tool. The work pieces are clamped between two tool shoulders connected by the probe. Welding of hollow profiles, such as a longitudinal member for integral subframe in a passenger car as shown in Figure 1 becomes possible. Especially under the consideration of crash relevance, the mechanical properties of friction stir welding seams close to the base material can be a great advantage.

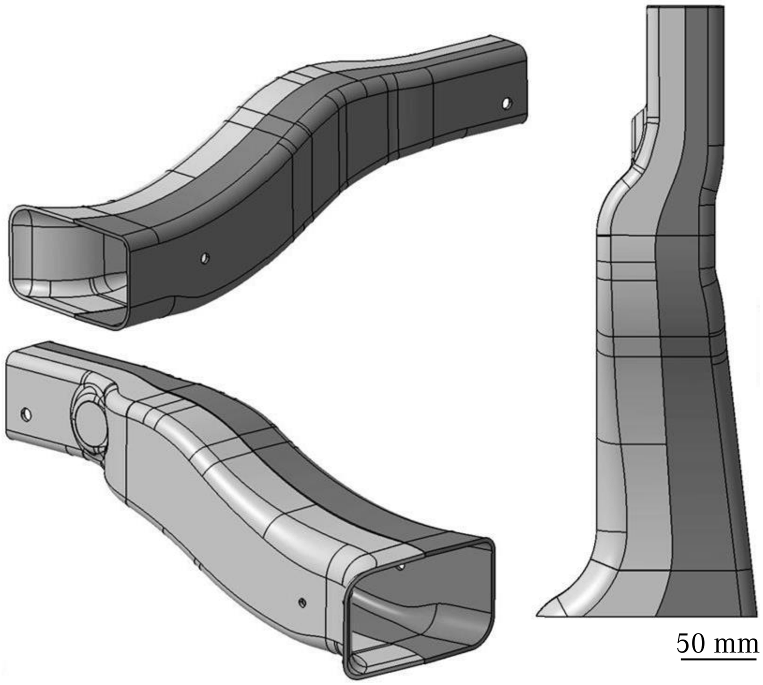

Figure 1. Longitudinal member for integral subframe in a passenger car in courtesy of Daimler AG [7].

Previous works studied new tool designs to improve the performance of the process. Threadgill [6] stated in 2010 that “New (tool-) designs tend to differ only in detail, and it is unlikely that further variation on these will lead to significant improvements in the performance of the process or the properties in the welds, although benefits related to specific applications are likely”. The motivation of the present study is to address the knowledge gap mentioned above, emphasizing a deeper comprehension of the ongoing mechanisms in the weld zone. The alternation of an existing process variant to a new process variant is the chosen approach. Based on the industrial demands, the feasibility study of the new process variants is accompanied by numerical simulation, in order to understand observed phenomena in the experimental procedures. Main focus is the further understanding of the material flow and its initiation, as well as the related forces during the process.

2. Objectives

The main objective of the present work is to develop a FSW process variant which is more suitable for articulated arm robots. For this purpose, the following improvements in the known FSW processes are aimed:

- Reduction of the forces that are responsible for oscillating deviation of the handling system from the welding path and consequent failure in the consolidation of a weld;
- Increase of the welding speeds and reduction of the heat inputs.

Furthermore, the welding process should compensate work piece tolerances considering height and thickness changes. To fulfil these industrial demands, the following milestones were defined:

- Build a welding spindle and handling system capable of conducting the process variants;
- Develop tool design for the process variants;
- Develop numerical models for each process variant;
- Conduct baseline experiments with known process variants to validate handling system and welding spindle;
- Conduct experiments with other process variants and evaluate the results;
- Determine a dominating indicator for the different behaviour of the process variants with the focus on material flow and process forces;
- Focus on most promising process variant and evaluate produced welds.

A successful process development depends on a deeper understanding of the mechanisms involved in the consolidation of a weld. For this purpose; this work will be supported by process modelling, which will be also used for understanding of observed phenomena. The main scientific objectives of this interchanging method between experiments and simulation are to explain the different behaviours of the process variants and to find an indicator for the experimental feasibility.

3. Literature Review

3.1 FSW Process Variants

With the correct equipment and the right parameters, the process appears very elegant as stated by Zettler in 2010: “The complexity of the process is not seen easily. Spectators and newbies are often amazed by the simplicity and seeming effortlessness of the welding procedure. But in truth the factors of good quality joint – or better a joint at all – are depending on complex situation in the welding zone” [8].

This section describes the FSW process variants and related studies to introduce the environment of the present work.

3.1.1 Conventional Friction Stir Welding: The Single-sided Process

The conventional FSW process consists basically of three steps: the plunge of the rotating tool, the weld along the joint line and finally the pull back of the tool. For some materials, a dwell time is necessary in the plunge phase to achieve a preheating of the tool and the work pieces [9]. In Figure 2 some definitions of the conventional FSW are indicated. An axial force is applied by the handling machine on the tool, which consists of a probe and a shoulder. For the counterforce a backing anvil underneath the welded part is needed. Due to the simplicity of the tool design in the conventional process, increased stiffness on the handling system is demanded to guide the tool and keep the process in stable conditions.

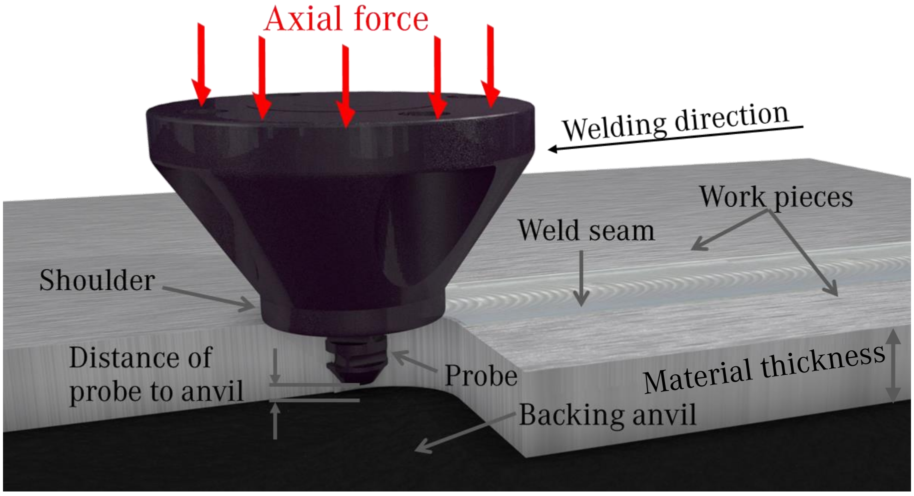

Figure 2. Important definitions of the conventional Friction Stir Welding process.

Special attention should be drawn to the distance in between the probe and the backing anvil, which correlates to the insertion depth of the tool. If this distance is too small, the shoulder of the tool plunges into the work pieces and the probe contacts the backing anvil, resulting on the weld of the work pieces with the anvil. When the distance is too big for the tool to achieve a penetration, the weld seam is not fully consolidated and the so called “root defect” occurs. It must be emphasized that this distance is controlled during the process by the axial force applied on the tool in combination with the rotational and welding speed. An oscillating axial force during the process can lead to variations of this distance between the probe and the backing anvil. Furthermore, thickness variations of the work pieces can lead to the formation of root defects or to the welding of the work pieces to the anvil. In the case of excessive forces, the plasticized material is forced to leave the weld zone as toe flash, and material loss can occur.

Völlner proposed a division of the handling systems for FSW into four groups, according to the amount of investment [10]. As a first group, specialized machines have the best capability of conducting FSW, but are also the most cost intensive handling systems. They are used in welding research labs around the world and there are some manufacturers available [11-14]. The second group consists of transformed CNC machine centres, and the third group of parallel kinematics such as the Tricept used in the present study. With the use of proper equipment, the advantage of high welding speeds with the single-sided FSW process must be mentioned; such as reported in literature with 10 m/min for aluminium alloy [15].

As a last group of handling systems, there are the serial kinematic systems, such as the articulated arm robots used by Völlner [10]. Their successful application on the conventional FSW process was reported in literature [10, 16, 17], and also transferred into industrial solutions [18]. The insufficient stiffness of the articulated arm robots limits the welding speed and brings challenges on the stabilization of the process along the joint line. As long as reduced forces are used, the industrial robots show to be well applicable to conventional FSW processes. This can be observed in low force FSW such as welding of polymers [19].

Another advantage of the articulated arm robots is the possibility of three dimensional (3D) welding. Applications of 3D welding with the single-sided process are reported frequently [4, 10, 18]. Even though, they are not implemented in large scale industrial application because of limited welding speeds achieved. All the attempts with articulated arm robots indicate the general preference for these handling systems in large scale industrial application. This interest is due to their high degree of variability in combination with low costs. As a particular advantage of this variability, industrial robots can be used for other tasks if there is no necessity for welding jobs anymore. For example they can be used as pick and place robots.

Considering the high loads and the high welding speeds necessary for industrial application, the conventional FSW process is limited to the use of specialized equipment. For these reasons it was necessary to alter the original process in order to allow the application with the fourth group of handling systems.

3.1.2 Stationary Shoulder FSW

Stationary Shoulder FSW (SSFSW) processes are mentioned in recent literature [20-25] and systems for industrial production are available [4, 26]. With the solution from Kuka Robotic GmbH the first application in large scale production was achieved: Apple Inc. is producing the housing of the iMac with the SSFSW process [5]. The stationary shoulder shows an improvement when compared to the conventional FSW mainly in two ways concerning the forces. First, the axial movement of the shoulder diving into the material is limited, because of its stationary condition. The contact or welding to the anvil, mentioned in Section 3.1.1 for the conventional process, only occurs in rare welding conditions for the SSFSW, because the material underneath the stationary shoulder is not softened and supports the pressure from the tool. Therefore the axial forces have not to be controlled as exactly, because higher forces have little effect on the position of the stationary shoulder. This is different from the behaviour of the rotating shoulder in the conventional FSW process. Second, the stationary shoulder stabilizes the handling system during the plunge and preheat phase through static frictional contact of the tool with the work pieces.

In SSFSW only the probe of the tool is rotating. Comparing the tool concept of conventional and SSFSW at a same rotational speed, the sole rotation of the probe in SSFSW leads to a reduction of the orbital velocity on the outside radius of the rotating parts. Due to the reduction of the orbital velocity, the rotational speed can be increased for the SSFSW without reaching the physical limit of the active centripetal force on the material. As a result from this and the missing contact of the rotating shoulder to the work piece, the side forces are reduced. As a further advantage, the diffusion process induced by the pressure of the stationary shoulder on the trailing side of the probe supports the consolidation of the weld. On the surface of welded material this is called “hot ironing” effect. The positive effects of SSFSW were reported by several authors [20, 21, 27, 28]. With the SSFSW process variant, the 3D applications are possible, but very limited in radii of the welding path and welding speed.

3.1.3 Bobbin Tool FSW Process

In the past years the focus of the FSW society is directed more onto the bobbin tool (BT). The Figure 3 presents the main definitions of this tool. The main difference of this process is that the anvil of the conventional FSW process is replaced by a second shoulder element. The probe extends through the work pieces. The second shoulder element, the lower shoulder, is mounted at the lower end of the probe. The process description is given for the different process variants in Section 3.1.4.

Recently there are more sources available on BT-FSW, even though the tool design was already mentioned in the original FSW patent from Wayne Thomas [2]. Hilgert described the process and the modelling of the process [1, 29-34]. Welding was also conducted by Neumann and Li [35, 36] at the HZG. Other papers have been published in the beginning of the last decade [37] and with an increasing magnitude more recently [38-48]. The process is also frequently described in books and compendia [22, 49]. The bobbin tool FSW (BT-FSW) process has great advantages in comparison to the conventional FSW process: since the axial forces are kept inside the tool, as indicated in Figure 3, they do not have to be applied by the handling machine. Therefore, the stiffness of the machine can be reduced to a level which is still sufficient to keep the tool on the joint line and handle the radial forces of the process. With the forces kept away from the handling system, the use of BT is a common approach in literature to minimize the handling equipment [38]. The main disadvantage of this process occurs from the same reason the main advantage does: the gap force, which is the main axial force in BT-FSW, is kept inside the tool. The probe is the most vulnerable part of this configuration, because it has small dimensions and operates under elevated temperature and high load conditions.

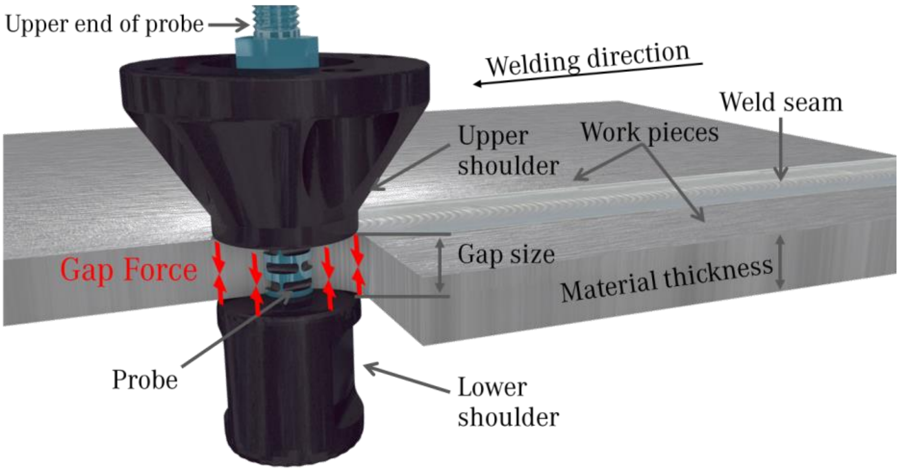

Figure 3. Important definitions of the bobbin tool FSW process.

The advancing side (AS) and the retreating side (RS) during the welding process are shown in Figure 4 (a). The combination of the rotation of the tool and the welding direction defines the AS and the RS. These definitions are done in agreement with the milling and the conventional FSW process. Yet, the BT-FSW process is different to single-sided FSW processes. While at a single-sided process the position of the shoulder can be adjusted with any tilt angle, at the BT-FSW process this correction can be done for one shoulder, but the adjustment influences both shoulders as shown in Figure 4 (b). Due to this characteristic, a bending of the probe leads to one tilted shoulder, which cannot be compensated by such path adjustments.

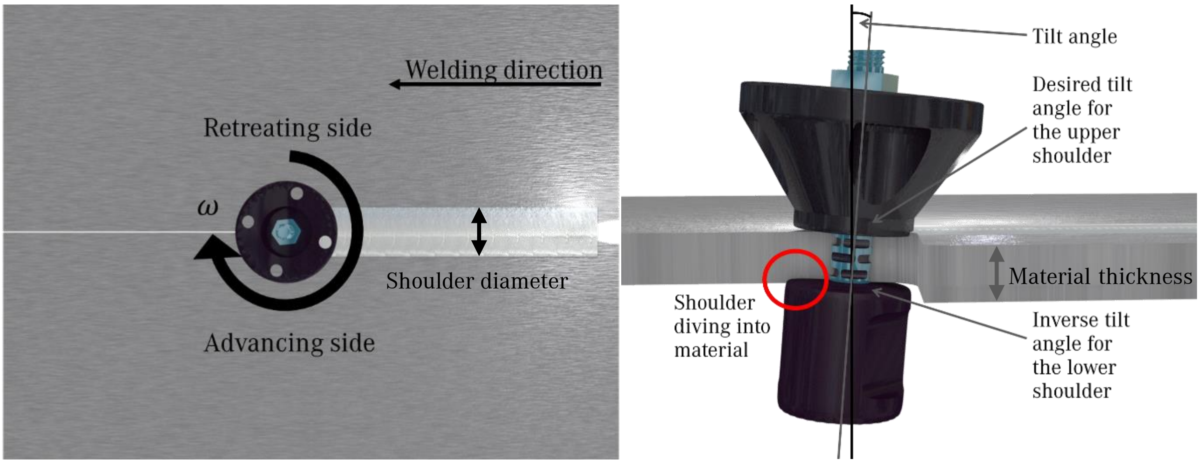

(a) (b)

Figure 4. Definition of (a) advancing and retreating side and (b) tilt angle in BT-FSW.

In the BT-FSW process, there are three loads which have the highest influence on the probe. First, there are radial forces resulting in bending and as second there is a torque. The third load, the axial force is superpositioned to the radial forces and the torque on the fragile probe. The bending are mostly caused by the rigid solid material in front of the probe. Furthermore, the radial forces increase because of the frictional forces opposite to welding direction aroused by the contact state between the lower shoulder and the work pieces. Additionally the Magnus-Effect in between two opposing movements of fluids creates transverse forces which add to the bending [50]. The torque is applied to the probe due to the transportation and the contact between the probe's surface and the plasticized material as in the conventional process. In BT-FSW an additional torque from the lower shoulder increases the loads applied to the probe. To fit the probe to the elevated load conditions, increasing the diameter is a common approach for BT-FSW. This increase is limited by the physics, as a consequence from the ratio of probe diameter and sheet thickness, the rotational speed and the welding speed, which are subjected to a window of welding parameters. Moreover, if the probe diameter increases, the volume of material which has to be transported around the probe also increases, since the profile of the probe which is driven through the material is increased.

As described the mechanical load is of complex nature. One of the challenges of the BT construction is to create a probe with a homogenous stress distribution under the process loads that can induce sufficient material transport. This homogenous stress distribution can be achieved by smooth surfaces in the area of high strain, which coincides with the process zone. As a contrast, the design should provide features to guide and initiate the material flow around the probe. Non-featured tools have resulted in disadvantages in the welding experiments [51]. Comparable results were also observed during the present work. The features on the tool surface can become obsolete only with very low welding speeds. Sued et al. [39] suggested that vertical and horizontal flow movements contribute to the welds which are mostly depending on the tool geometry. Since the rotation of an unfeatured tool can only provide horizontal flow movement, features are a necessity.

One difficult aim to achieve in known BT processes is finding a set of corresponding parameters of welding travelling speed, rotational speed, and gap force. The resulting process parameters are gap size (mm), torque (Nm), power (kJ/s), line-energy (kJ/m), and welding pitch that is the ratio between welding speed and rotational speed (mm/rev) [52, 53]. An analysis of the resulting parameters can give in most cases an indication of the quality of the obtained weld. The line-energy q_{Line}, which is given in Equation (1), is comparable to the heat input in fusion welding processes [1]. This parameter can be calculated using the torque M, angular velocity ω, and welding speed u.

$$q_{Line} = \frac{M\,\omega}{u} \tag{1}$$

The typical double V-shape of the stirred zone (SZ) in BT-FSW is shown in Figure 5. The thermo-mechanically affected zone (TMAZ) and the heat affected zone (HAZ) are also indicated.

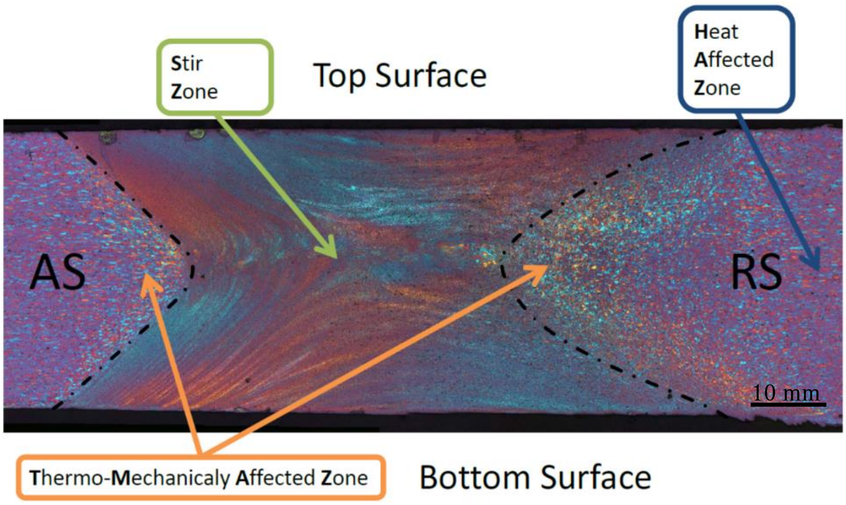

Figure 5. Zones in a BT-FSW cross section macrograph [1].

The BT-FSW process presents a unique challenge according to the thermal situation during welding. The heat input is increased in comparison to the single-sided FSW. The lower shoulder produces additional heat on the surface of the material and in the transported volume in vicinity [29]. Besides that, the lower shoulder works as a reduced heat sink when compared to the anvil in the conventional FSW process. Since the diameter of the probe is increased as well as the probe is extended through the work piece, the active surfaces on the probe are also increased. The sum of these characteristics leads to elevated heat input and temperatures during the welding process in BT-FSW and can cause a deterioration of the material in the weld zone.

The performance of the BT concept is limited regarding welding speed when referred to the conventional process. For 6082-T6 aluminium alloy, maximum welding speeds of 50 to 600 mm/min were reported in sources [39-41, 44]. Until a welding speed of 300 mm/min, the welds were described as defect free. Higher welding speeds achieved in tensile tests 68% strength of the base material. It was also observed that the welds were thicker on the RS and thinner on the AS compared to the base material.

There are some industrial solutions offered for BT-FSW, as listed by Neumann [36]. However, to the author's knowledge there is no large scale industrial application of the process. Furthermore, there are no welds reported in literature achieved by an industrial robot equipped with a BT-FSW solution. Some approaches for industrial robot application were made by the LaFT from 2004 to 2009 [54-56] and Völlner supported the theoretical benefit of the process to the application on articulated arm robots [10].

3.1.4 Derivatives of the Bobbin Tool FSW Process

The focus of this work are the BT-FSW process variants. The different tool concepts of the BT-FSW process variants are explained in this section.

3.1.4.1 Fixed-gap Bobbin Tool Process Variants

A fixed-gap BT can be constructed in two ways. The simplest approach is a monolithic tool manufactured in one piece with a fixed-gap between the shoulders. In the case of the adjustable BT it consists out of more parts. The gap of the tool can be adjusted before the process and, once set, it is fixed during the welding. The process parameter gap size must be known before the weld or be found trying different tool adjustments. In literature, welding with a fixed-gap tool is the common approach due to the simplicity of the equipment [36, 38, 42, 44, 46, 57]. This tool concept was also used for the previously mentioned achieved welding speeds [39, 40, 44, 58]. Even steel welds were conducted using this concept [59].

During the process, thermal expansion is responsible for elongating the probe and also the welded material. The tool and the welded material have different thermal expansion coefficients. This difference leads to challenges in the fixed-gap process, because the correct gap size changes with the temperature conditions along the welding path. At the starting phase of the process the tool needs to be inserted into the material. With the gap adjusted to the right size for the process conditions at elevated temperatures, the run into the material can generate high forces. Figure 6 (a), (b), (e), and (f) show the main steps of the fixed gap process[1]. Basically, the same adjustment of the gap cannot be suitable for the run-in and for the welding.

---

[1] Figure 6 (c) and (d) are valid only for the self-reacting process introduced in section 3.1.4.2

3.1.4.2 Self-reacting Bobbin Tool FSW Process Variant

In the self-reacting bobbin tool (SRBT) process variant the distance of the shoulders is adjustable during the welding process. Often the name self-reacting tool is mistaken as another term for BT [6, 59], but this is not the case. Self-reacting bobbin tool is a force controlled bobbin tool according to the FSW standard ISO 25239 [60]. This way, it is possible to compensate differences between the thermal expansions of probe and welded material, and also thickness variations of the material. A step by step introduction of the conventional SRBT process is given in Figure 6, where (a) and (b) show the tool and the two work pieces with the run-in notch. In Figure 6 (c) and (d) the run-in and the start of the process can be found. These steps present the basic differences between the fixed-gap and the self-reacting concept that are a controlled run-in and a controlled heat up phase with the conventional SRBT. The tool can be moved in between the work pieces into the run-in notch without contact. By pulling up the lower shoulder or –depending on the used system – moving down the upper shoulder, the preheat phase can be conducted and the welding process can be started, as seen in Figure 6 (c) to (f). Due to the complexity and specialization of the equipment the SRBT is limited to few reports [1, 29, 31, 35, 37].

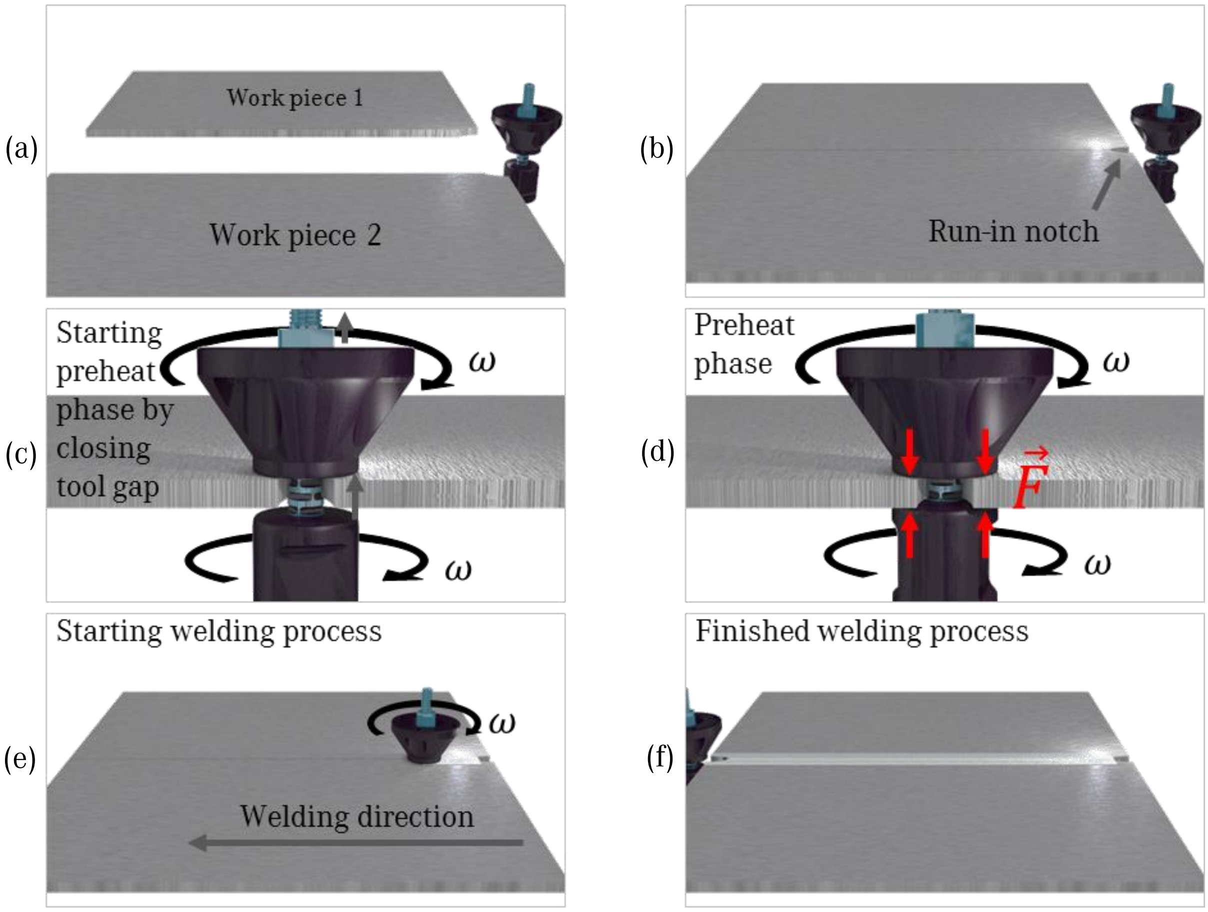

Figure 6. FSW process with self-reacting bobbin tool consisting of (a) work pieces and tool, (b) run-in notch, (c) starting welding sequence, (d) preheat phase, (e) starting welding process and (f) finished welding process.

3.1.4.3 Stationary Shoulder Bobbin Tool Process Variant

Hilgert focused his research on the conventional SRBT process [1]. During his work, he developed the idea of a stationary shoulder bobbin tool (SSBT) process variant [32]. The main idea of this tool concept is to keep both shoulders standing still and only rotate the probe. As a result, the frictional energy should be developed on the surfaces of the probe. The aims are to produce the energy where it is essential for the process and overcome the challenges of the increased orbital velocity on the outer radius of the shoulder. The idea of a semi-stationary shoulder process is included in the patent of Hilgert et al. [32], and the claim of the patent is focused on the full stationary shoulder approach. The upper shoulder of the patent was described as an exception “In einer dazu alternativen, bevorzugten Ausführungsform ist der Stift frei um die Drehachse drehbar mit dem ersten Schulterelement verbunden.” [32], and therefore a semi-stationary process is published, but not patented with this patent. Suda et al. [61] studied the feasibility with different stationary shoulder configurations, but the study did not include any information about the tools and used welding parameters.

3.1.5 Tatsumaki Process

The Tatsumaki process is similar to the BT-FSW process. In the concept of the Tatsumaki process the BT is divided into two separate parts. One part functions as a conventional tool on the upper side, yet with a probe penetrating through the complete thickness of the work piece. The other part of the tool consists solely of the lower shoulder with a recess which is driven by a separate actuator. The lower end of the probe of the upper shoulder is placed in the recess of the lower shoulder. Welds have been successfully conducted with this concept. Welding speeds of 500 mm/min on AMX602 magnesium alloy with 4 mm thickness and 4000 mm/min on AA5052 aluminium alloy with 3 mm thickness have been achieved [58, 62]. An advantage of the process is that the angles of the shoulders are adjustable individually. Moreover, the tensile stress on the probe occurring in BT-FSW is applied by the machine. As a disadvantage for large scale industrial application, the machine for the upper shoulder must have similar specifications to a conventional FSW machine. As another limitation compared to BT-FSW, there must be an additional drive for the lower shoulder, which is working parallel to the first machine. This demands a second part of the handling system also with similar specifications to a conventional FSW machine. Furthermore, the work piece must be accessible from both sides and the handling system must be built around the working space. With an increase of complexity of the equipment, the advantages of the conventional FSW are combined with some advantages of the BT-FSW in the Tatsumaki process.

3.2 State of the Art Equipment at the Helmholtz-Zentrum Geesthacht

The state of the art handling system at the Helmholtz-Zentrum Geesthacht at the starting point of the present study was the FlexiStir machine. The machine is described by Hilgert [1] and is capable of controlling the SRBT process variant. In previous studies SRBT and SSBT tool sets were developed.

3.2.1 SRBT

A SRBT consists mainly of the probe and the shoulders. The lower shoulder is commonly screwed on the probe and secured by additional elements. These elements must be carefully designed, since their clearance should not affect the tasks during the welding process and also should be sufficient for not blocking the tool due to different thermal expansion. Furthermore, the disassembly must be possible after the welding process and especially after tool failure or process forces exceeding the tools capability.

One of the major challenges of the tool design used before this study was the disassembly of the tool after welding. Hilgert [1] described this difficulty as a result of the wear of the torque transmitting ring shown in Figure 7. In the previous design the lower shoulder was secured with a ring designed to block the rotational degree of freedom. The design used flat surfaces on the probe, as indicated in Figure 8 (a), to lock the rotational degree of freedom in tight fit manor. During the process the ring was pushed into the threads of the probe. After the welding process the torque transmitter was indented by the threads of the probe as shown in Figure 7 by Hilgert [1]. The fluted surface in Figure 7 was originally the flat surface for the torque transmission and was not supposed to be in contact with the threads. These indents blocked the axial removability of the torque transmitter and damaged the threads of the probe. Often disassembly was not possible without destroying parts of the tool.

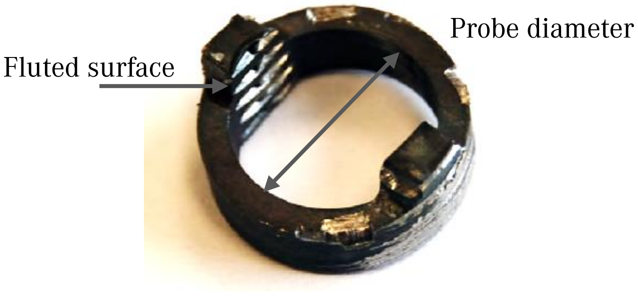

Figure 7. Damaged torque transmitting ring. Adapted from [1].

3.2.2 SSBT 1st Generation

The basic construction of the first SSBT is similar to the SRBT design. The most important changes were the missing features on the upper shoulder and the fully new construction of the lower shoulder. As seen in Figure 8 (c) the lower shoulder is supported by bearings. The bearings were mounted on a bearing support shown in Figure 8 (b), which was inserted in the shell of the lower shoulder. The axial force was transmitted through the shell onto the upper bearing onto the bearing support to the threads of the probe. The torque of the shoulder was transmitted by two radial setscrews, which extremities were pressed against the flat surface of the probe. The bearing support was fixed in rotation by two setscrews. The design of the probe remained unchanged from the conventional SRBT in the first SSBT.

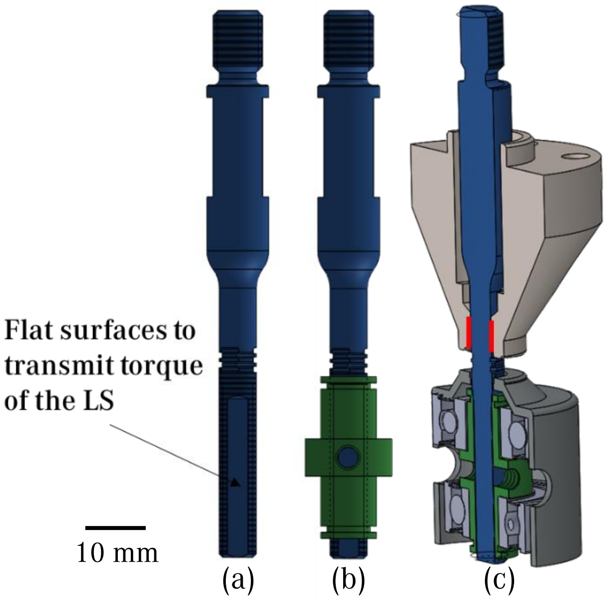

Figure 8. Original probe concept with (a) flat surfaces, (b) original bearing support and (c) as an assembly of the original stationary shoulder bobbin tool.

3.3 Stop Action and Marker Material Experiments

There are two general experimental approaches to visualize flow during FSW experiments. One approach is to stop the process during the welding, and the other is to use marker material to analyse the flow pattern of the embedded marker (or tracer) material in a post-weld condition. These methods can also be combined. Most published work focuses on the formation of the typical FSW pattern, the onion rings or on the evaluation of horizontal flow during conventional FSW [63, 64]. For BT-FSW few experimental flow research is available. Chen et al. [41] researched the fixed-gap BT process variant with a welding speed of 300 mm/min on AA6082 in T6 temper condition with a thickness of 12 mm. Major deposition of material from the AS on the RS was reported. Also, the influence of vertical flow in the results was evident.

For the conventional single-sided FSW process there is a variety of studies available in literature. Colligan published in 1999 one of the first works on the topic with stop action technique and tracer material [66, 67]. In Figure 9 the influence of the thickness level and also of the initial position of the marker material on the pattern on the trailing side of the probe can be observed. At 85% thickness level of the work pieces (positions 1 to 4) the influence of the rotating shoulder is more present distributing the marker material. A correlation between the initial position on the leading side and the final position on the trailing side is hard to establish. At the mid-thickness level of 55% of the work pieces (positions 5 to 8) the material transport appears to be laminar. A dependency of the final position on the initial position of the marker material is present. The marker material on the AS (position 5) shows a behaviour not as distinct as the material on the RS (position 8). Furthermore, the differences in the SZ for different tool geometries were correlated with the shape of the tool surfaces: flats were observed to be responsible for transporting material around probe and threads for downwards flow in conventional FSW. This is especially important for the transporting mechanism. The transport can be divided in the typical stirring of the material around the probe and the extrusion of the material on the RS. Arbegast [68] divided weld zone into different flow-depending sub-zones. In general conventional FSW flow is different to BT-FSW, because the flow underneath the probe does not occur in BT-FSW.

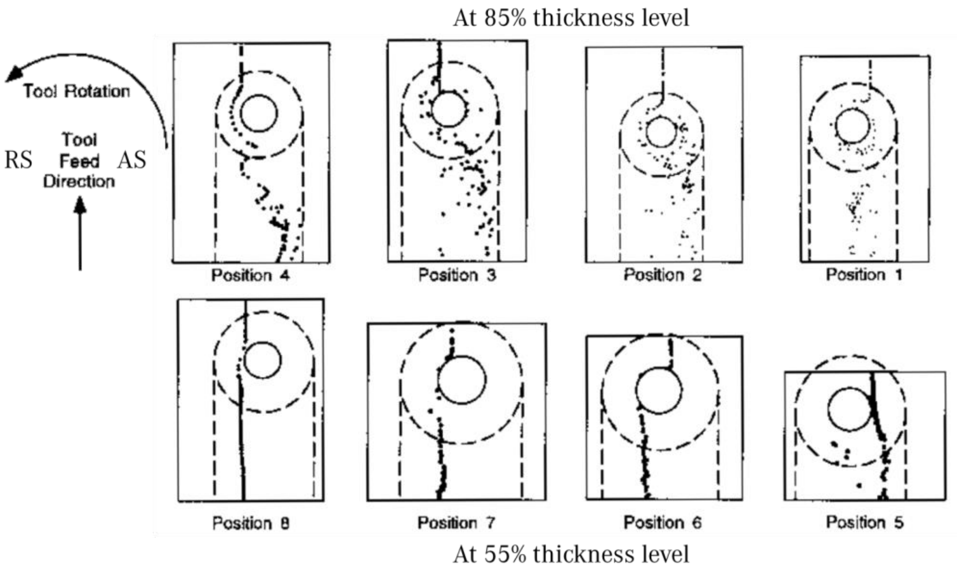

Figure 9. Marker material experiments conducted in thickness level 85% and 55% of the work pieces and advancing at different positions on the leading side. Adapted from Colligan [65].

Zettler's work involved stop action technique as well [69, 70]. An asymmetry of the SZ was reported by the author for several welds. Ti-powder with the particle size 20-62 μm was used to compare a Triflat probe and a threaded round geometry probe. As a result the flow was observed as dependent on the probe geometry. Especially the horizontal flow appeared to be influenced by the machined surface of the probe. A material transport over 360° was also reported. Guerra et al. [71] showed that the material approaching the AS rotates around the probe before it is placed on the trailing side. Also the influence of the shoulder was shown dominating the SZ in about one third of the thickness of the work pieces. Reynolds and Seidel [72, 73] focused on forces in the evaluation of the welding experiments. The research was conducted with marker material experiments and furthermore with CFD simulation. The shape of the influenced marker material can be seen in Figure 10. The position of the marker material in the vicinity of the shoulder is presented in Figure 10 (a). In contrast the marker material in mid-thickness level which is influenced by the probe is given in Figure 10 (b). These shapes are also found in the research of Schmidt and Hattel [74, 75], who introduced discretized shear layers - or flow zones - as an analytical model for the marker material experiments. Additionally, a sticking contact condition in between the probe and the welded material and a continuous flow in counter direction on the AS of the probe was proposed.

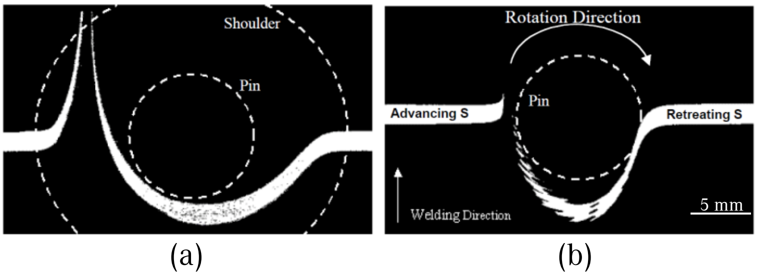

(a) (b)

Figure 10. Flow pattern observed from marker material experiments (a) in the vicinity of the shoulder and (b) in mid-thickness [73].

Chen et al. [76-78] investigated the formation of the FSW pattern and the shear layers during the welding process. A cross section along the mid-plane of the weld in stop action technique is shown in Figure 11 [76]. During the welding procedure the probe failed and a missing flow on the AS can be observed in point S. The deposition of material on the trailing side of the probe is incomplete and ceasing at point E. The consolidation of the weld seems to proceed in discrete deposited layers. A similar behaviour on the AS was observed with unthreaded tools by Lorrain [79]. Further investigation on the flow can be performed with CFD simulation, as covered in Section 3.4.

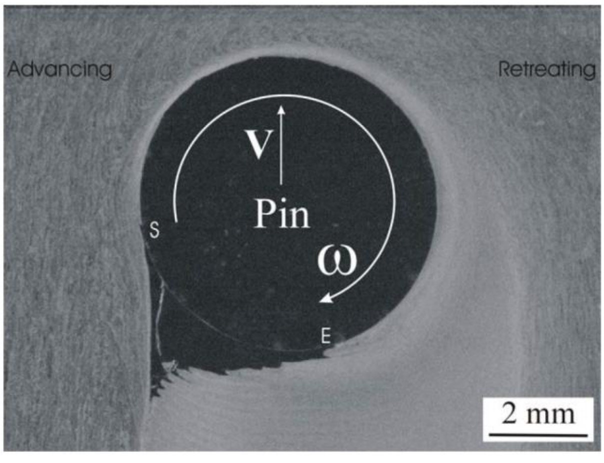

Figure 11. Stop action with a broken probe and insufficient flow conditions [76].

3.4 Flow Modelling

Flow modelling on conventional single-sided FSW is described in literature by several authors [80-85]. Yet, for BT-FSW there are limited studies available [31, 41]. As mentioned the experiments for flow are mostly describing the conventional single-sided FSW process as stated in Section 3.3. Hence the corresponding CFD simulation in these studies is also done on the conventional FSW process. Still, this CFD modelling with particle tracing resulted in similar flow to the described in the previous Section 3.3. The typical flow pattern presented in Figure 9 was found as well in the simulation of Zhang [86-88]. The flow patterns in Figure 10 were successfully simulated by various researchers [89-92] and the flow around the probe with the flow line patterns was presented in Hilgert's work and also in literature [1, 93, 94]. The asymmetry of the marker material pattern between the AS and the RS was shown in various studies [83, 85, 95-97]. Furthermore, a continuous flow on the AS was reported in these sources. Especially in binti Sataruddin's work continuous flow close to the probe was found [83]. The asymmetry and the continuous flow on AS cause a higher strain gradient on the AS, as stated by Zhang et al. [98, 99] and Pashazadeh et al. [100].

The effect of transverse speed was studied by Zhang et al. [101]. A maximum welding speed of 240 mm/min for AA6061-T6 was achieved in the experiments. Yet, computational problems occurred with higher welding speed in CFD simulation. Zhang et al. [102] concluded in another work that an enhanced material flow is a positive effect of increased welding speed. This study included welding speeds up to 142 mm/min.

Regarding the viscosity of the welded material there are different approaches pursued in literature. Positively mentioned viscosity models are based on the constitutive law of flow stress by Shepard [103-105]. The viscosity models used in the present work are also based on this law and frequently used [1, 50, 72, 86-88, 90-92, 97-101, 106-108]. This effective viscosity is further introduced in Section 5.3.1. Additionally, there are other descriptions of viscosity available. The classical Coulomb model or a modified version of the model was used [81, 82, 85, 86, 89, 90]. The power law is used for FSW CFD simulation [85] and a pseudo frictional flow model was developed as a corresponding viscosity to the heat source modelled by Schmidt [95]. This viscosity depends on temperature and shear stress and uses the ultimate tensile stress (UTS) as a function of temperature as main material parameter.

Hilgert started with a Lagrangian formulated CFD model with the geometry features of the probe of the imported CAD [1]. The model used an input of results from an Eulerian formulation as initial values. Starting time dependent models with the full rotational and welding speed and fully active viscosity model can lead to convergence problems of the solver. For this instance it is necessary to ramp up the experimental parameters and also the effective viscosity before beginning the evaluation of the state received from the experiments. In Hilgert's experiments the welding speed was limited to 120 mm/min and the maximum rotational speed was 600 rpm for the CFD simulation. A higher gradient in the shear rate and temperature field can result in even higher difficulties to achieve convergence for models with viscosity functions based on the constitutive law of flow stress. Since the welding and the rotational speed are higher and the temperature field is smaller, the time dependency was not followed in the present work.

3.5 Working Surface Pairs & Channel Support Structures Model

To understand the technical system and make a difference between important components and surfaces to the ones which have no influence on the purpose of the technical system, a systematic abstraction can be helpful. One of the models is the element model of “working surface pairs & channel support structures” [109, 110]. This model conjuncts the layout and function of a technical system. In the present work the functional surfaces are referred to as “active surfaces”. Furthermore, if there is an interaction between a pair of contact surfaces, it will be referred to as “contact channel”.

3.6 Summary and Conclusions

Since the invention of FSW different attempts to reduce forces and increase welding speed have been made. The BT was already included in the original patent. The main advantage of the BT-FSW is that the axial forces are kept inside the tool and not applied as loads to the handling system. The resulting forces in axial direction are close to zero regarding the handling system. As a consequence a high tensile stress is also applied on the probe in elevated temperature environment. The probe is therefore the most demanded part of the BT and for this reason the axial forces which can be applied during the welding process are limited. Furthermore, the resulting radial forces are reported to be high. The focus of recent research is on the BT-FSW, on SSFSW and also on the Tatsumaki process variant. While the BT-FSW is limited in welding speed, SSFSW is limited in welding profiles. The Tatsumaki process variant is reported to achieve high welding speeds, but the equipment is highly specialized and complex. Additionally the work pieces must be accessible from top and bottom side. In order to weld hollow profiles and achieve elevated welding speeds, the approach of BT-FSW in combination with a stationary shoulder is chosen for further research. To reduce forces the flow initiation at the start and during FSW should be investigated and a concept fulfilling the demands established.

4. Setup and Experimental Procedure

The present work starts with the idea of stationary shoulder BT-FSW and ends with the evaluation of the received welds. As a preparation phase the hardware was set up. The development of a welding apparatus, the configuration of the process variants, the development of the welding tools, and the choice of the material for the welding experiments were done. Then the baseline experiments were proceeded with the known conventional BT process variant. The experiments for the process development of the other process variants were conducted with the coordinate search algorithm. The last step of the work included further experimental procedures focused on supporting the proposed argumentation from the simulation and on the comparison of the different process variants.

4.1 Base Material AA6082-T4

The aluminium alloy AA6082 is a commonly used material for FSW. Welds with this material have been reported in several publications [51, 52, 111-113]. Furthermore references of welded AA6082-T6 with the bobbin tool process are available [39-41, 44, 45]. The hot deformation behaviour of AA6082 has been studied by Spigarelli et al. and Zhang et al. [108, 114], which give necessary material parameters for the modelling. In the present work, all experiments on the new T805 welding system are conducted on AA6082-T4. It is also a widely used precipitate hardened alloy in the industry [115, 116]. The nominal composition is 1Si0.65Mg0.2Fe0.52Mn. From the EDX analysis on the datasheet of the delivered material, the chemical composition of the alloy is given in Table 1 [117]. The addition of Manganese is responsible for raising ductility. Mechanical properties of this alloy are highly influenced by common welding processes [115, 116, 118].

Table 1. Chemical composition of AA6082-T4 aluminium alloy as delivered

AA6082	**Si**	**Fe**	**Cu**	**Mn**	**Mg**	**Cr**	**Zn**	**Ti**	**Others Single**	**Others Sum**	**Al**
Spec. min [%]	0.7	-	-	0.4	0.6	-	-	-	-	-	-
Spec. max [%]	1.3	0.5	0.1	1.0	1.2	0.25	0.2	0.1	0.05	0.15	-
Actual [%]	0.8	0.16	0.06	0.42	0.7	0.01	0.02	0.03	0.01	0.03	Bal

Backlund et al. [119] reported that the friction stir welded material AA6082-T4 could be fully recovered according to the hardness profile after artificial aging for 3 hours at 185°C. The base material in T4 temper condition with thickness of 4 mm was reported to achieve 138 MPa yield strength, 244 MPa tensile strength and an elongation of 18.8% in the tensile testing. After artificial aging, 285 MPa yield strength, 360 MPa tensile strength and an elongation of 9.9 % were presented for the same alloy by Mishra et al. [16].

4.2 Development of the Tricept T805 Bobbin Tool Welding Spindle

In the beginning of this study, the experiments for BT-FSW at Helmholtz-Zentrum Geesthacht were conducted on the FlexiStir machine which is described by Hilgert [1]. Due to the challenges of the stationary shoulder BT processes, soon the necessity of a new handling system became present. The experimental investigation of the new process variants continued after finishing the development and building of a unique welding spindle. The new system is presented in Figure 12.

It shows a PKM T805 Robot equipped with this spindle suitable for the conventional SRBT FSW and for all the stationary shoulder process variant. For the new welding system the tasks of the mechanical configuration of the welding spindle, the interface for operation, the implementation for the sensor, the transmission and data recording between the robot and the spindle, and the programming of the system were completed.

Figure 12. Tricept T805 robot with bobbin tool spindle.

4.2.1 Mechanical Configuration of Tricept T805 BT Welding Spindle

The mechanical setup of the PKM Loxin T805 is a five axes parallel kinematics. Three of the five axes are arranged parallel and control the fist of the robot. The main advantage of this system is the high stiffness in comparison to an articulated arm robot. As mentioned, the welding spindle was added to the robotic system. The spindle has two actuators: one for the rotation of the main drive, which is rotating the tool. The other one is for controlling the translational movement of the gap in between the tool shoulders.

The main demands to the new welding spindle were to operate the system with a rotating upper shoulder and also with a stationary upper shoulder. In Figure 13 (a) the spindle is shown with the stationary shoulder configuration and in Figure 13 (b) with the setup of the rotational upper shoulder. Also the movement of the lower shoulder is demonstrated. The rotation of the drive for the gap control is converted into axial movement with a screw drive. Through a lever the axial movement is transmitted onto the shaft of the spindle, indicated red in Figure 13 (b). The rotational degree of the rotor of the spindle's main drive is separated through a bearing from the axial drive.

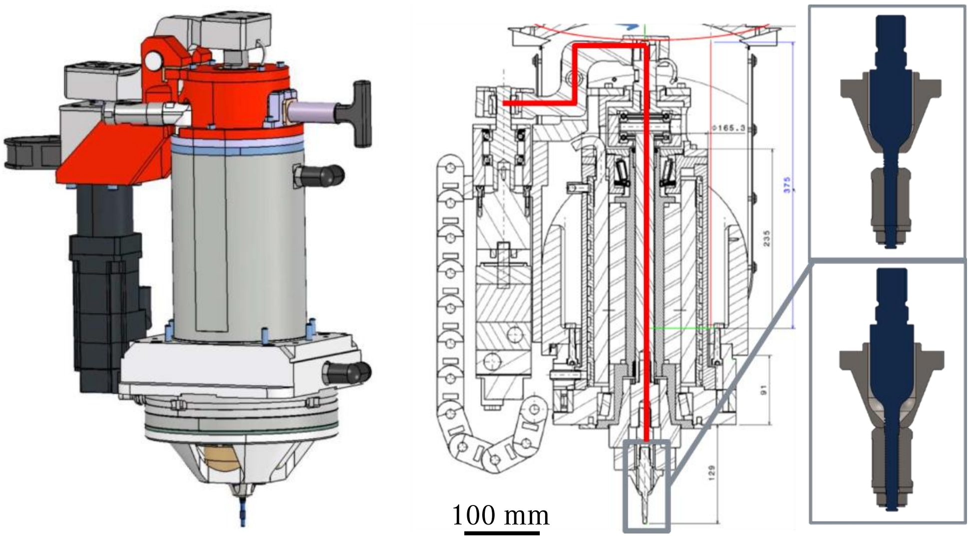

(a) (b)

Figure 13. Welding spindle configuration (a) in the stationary shoulder and (b) in conventional SRBT demonstrating the mechanism of controlling the gap.

4.2.2 Human Machine Interface (HMI) for the Welding Spindle

The objectives of the new system were to achieve great flexibility and improve handling, as well as implement an intuitive operation structure concerning the Human Machine Interface (HMI). Furthermore, the safety concern was an important issue.

The Program Logic Controller (PLC) controls all drives responsible for the welding operation. With the new system, the spindle is not integrated into the robotic system. It is stand-alone solution with the Computational Numeric Control (CNC) of the robot acting autarkic. For performance stability an industrial approved solution of the numeric control was equipped to the spindle. A challenge was to determine all needed functions of the HMI of the spindle to be prepared for any possible welding condition during the experiments. Thus, the welding conditions were divided into three research modes: fully manual, fixed-gap, and controlled gap. An example of the HMI for the lists of welding parameters of the conventional SRBT mode is given in Figure 14.

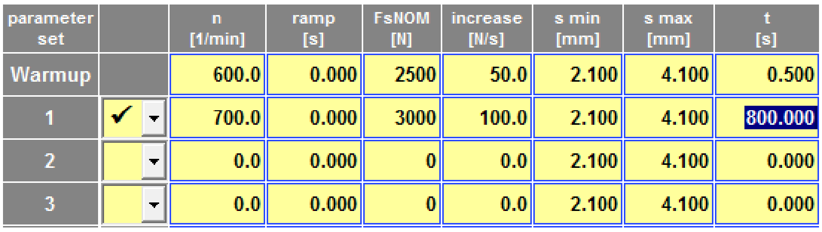

parameter set		n [1/min]	ramp [s]	FsNOM [N]	increase [N/s]	s min [mm]	s max [mm]	t [s]
Warmup		600.0	0.000	2500	50.0	2.100	4.100	0.500
1	✓ ▾	700.0	0.000	3000	100.0	2.100	4.100	800.000
2	▾	0.0	0.000	0	0.0	2.100	4.100	0.000
3	▾	0.0	0.000	0	0.0	2.100	4.100	0.000

Figure 14. List of parameters for the self-reacting gap.

It can be observed that the gap size is limited by the input $s_{i\,min}$ and $s_{i\,max}$. The rotational speed n_i with a time ramp, gap force $F_{s\,NOMi}$ with a ramp in N/s of de- or increase and the time of the parameter sets for an activity of time t_i are chosen by the user. Up to ten sets can be defined and the user can switch manually to each set of parameters during any time of the process. Also a manual alteration of the parameters is possible in the manual field on each welding HMI. To avoid tool destruction the operation is governed by safety force parameter $F_{s\,max}$.

The controller for the gap force in the FlexiStir machine is an incremental cycle of the multiphase motor for the gap control. For replication of this solution and also higher flexibility, the controller of the force gap was constituted to be fully parametric. In the new spindle two general options were implemented. According to the programming of the FlexiStir machine, a fully parametric incremental controller and, additionally, a proportional-integral-derivative (PID) controller were installed. However, for changing welding situations a different setup of the controller can be required. Thus, the incremental controller and the factors of the PID controller kp, ki, kd are fully parametric.

For higher flexibility, a possibility to alter HMI was implemented. The software for programming the PLC of the spindle was installed on a separate computer and can be accessed locally or via remote control.

4.2.3 Force Sensor Implementation

The bi-directional sensor for the gap force is applied in the line of the force transmission. However, the sensor for the reaction forces of the spindle in radial and axial direction gives forces in x, y and z direction. For the evaluation it is necessary to document the forces according to the welding direction. For example the force F_x in x-direction is defined as welding direction.

The movement of the robot is defined in addition to the three axial actuators of the T805 Tricept, by two radial degrees of freedom. The fourth axis rotates the fist of the robot around the centre axis of the three linear axes and the fifth axis adds another rotational degree within the fist of the robot. The rotational axis is perpendicular to the rotational axis of the fourth actuator, as indicated in Figure 16. The spindle is turned during the movement of the robot as demonstrated in Figure 15. Furthermore, welding direction can change within experiments or along the welding process, as also indicated in Figure 16.


(a) (b) (c)

Figure 15. Rotation of the force sensor plattform at a linear movement of the robot (a) starting, (b) approximately 50% done, while welding head rotated by approx. 45° and (c) completed while rotating angle changed to approx. 135°.

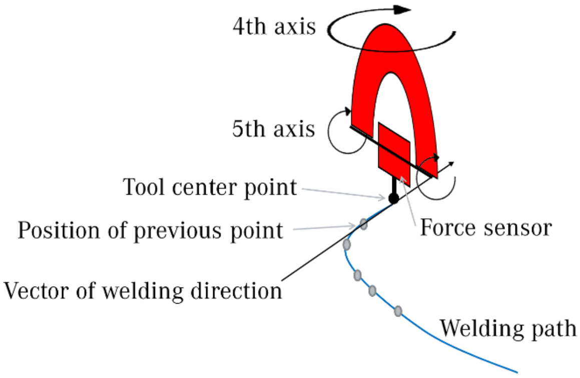

Figure 16. Changes on the direction of the welding forces and schematic parameters for force transformation.

The movements have to be tracked and documented in a log-file for evaluation to interpret the welding process in post-weld condition. For fast examination the transformed forces should be included. For the mathematical transformation, some important assumptions are made. In the mathematical equation, it has to be considered that the coordinate system is turning. The tilt angle of the bobbin tool is not feasible, as described in Section 3.1.3. This assumption leads to the conclusion that the x, y plane of the force sensor must be always a parallel plane of the welded zone on the work piece. To determine the welding direction a vector $\vec{u}$ is made by two points according to Figure 16, which are the tool centre point, indexed by the abbreviation tcp, and the last measured point before, as shown in Equation (2). This includes that the welding angle is referred to the robotic Cartesian coordinate system of the work piece coordinate system.

$$\vec{u} = \begin{pmatrix} x_{tcp} \\ y_{tcp} \end{pmatrix} - \begin{pmatrix} x_{tcp-1} \\ y_{tcp-1} \end{pmatrix} \tag{2}$$

If the work piece coordinate system is changed by the user – for example according to a rotational angle - the transformed forces are calculated to the new angle. In the software solution a build-in editable angle for this configuration was added. In summary three angles influence the transformation of the force direction according to the welding direction: $\varphi_{axis}, \varphi_{weld}\ and\ \varphi_{WCS}$. The sum of the angles $\varphi_{tot\,passiv}$ of the rotated coordinate system is given in Equation (3).

$$\varphi_{tot\,passiv} = \sum_{i=1}^{n} \varphi_i = \varphi_{axis} + \varphi_{WCS} + \varphi_{weld} \tag{3}$$

Herein φ_{axis} is the angle of the C-axis of the robotic system, φ_{WCS} the angle of the work piece coordinate system, and φ_{weld} the angle of the welding direction. The transformation of the rotation of a vector p of the coordinate system for an angle φ is done according to Equations (4) and (5):

$$p` = A^{-1}\,p \tag{4}$$

$$\begin{pmatrix} F_x{}' \\ F_y{}' \end{pmatrix} = \begin{pmatrix} cos\,\varphi & -sin\,\varphi \\ sin\,\varphi & cos\,\varphi \end{pmatrix}^{-1} \begin{pmatrix} F_x \\ F_y \end{pmatrix} \tag{5}$$

The inverse matrix A^{-1} can be expressed by the determinate $\det A$ and adjunct matrix A_{adj}:

$$A^{-1} = \frac{1}{\det A}\left(A_{adj}\right)T \tag{6}$$

Through inserting Equations (5) and (6) into the transformational Equation (4) with the rotational matrix, the Equation (7) for the transformed force vectors $\begin{pmatrix} F_x{}' \\ F_y{}' \end{pmatrix}$ can be obtained.

$$p` = \begin{pmatrix} F_x{}' \\ F_y{}' \end{pmatrix} = \begin{pmatrix} cos\,\varphi_{tot\,passiv} & sin\,\varphi_{tot\,passiv} \\ -sin\,\varphi_{tot\,passiv} & cos\,\varphi_{tot\,passiv} \end{pmatrix} \begin{pmatrix} F_x \\ F_y \end{pmatrix} \tag{7}$$

4.2.4 Communication Spindle ⇔ T805

As described previously, the spindle has a required portfolio of functions. A communication between the robot and the spindle had to be established for some of these functions. The communication was established in two categories: field bus communication and hardware wiring. The communication implicates mostly four basic tasks:

- Transmit the starting signal for the welding process;
- Provide the data for the recording;
- Provide the data for the transformation of vector forces of the force sensor;
- Establish emergency stop connection.

The starting signal for the welding process is necessary to assure a precise and timed warmup sequence. After the warmup, the robot is supposed to start the welding process by applying the welding speed. The starting variable is set by the PLC of the spindle and the robot continues with the program only after the welding process is started. If this would not be applied, the rotating shoulder(s) would dive into the material by closing the gap. A delayed starting process could lead to failure of the weld or failure of the tool. An advanced welding start would lead to a start with open shoulders, which could also result in tool failure.

For recording the data, an Ethernet connection was established in between a computer and the PLC. On the computer a programme was written in Visual Basic, which can record the data received from the connection. The task was to achieve equidistant timed recording of the parameters with a frequency of at least 200 Hz and for a sufficient amount of time. The solution for the T805 spindle is directly writing the data into a .csv file. The advantage of this process is that the amount of saved data is limited only by the capacity of the hard drive and the handling size of the .csv file. The protocol size of 100 Bit was chosen and the sequence of data is sent separately for each parameter time set. Since the communication involves a request and an answer, the minimum value of cycles is limited to the double of the PLC cycle. The cycle of the PLC of 1 ms results in 2 ms minimum time set. As an option a cache can be used and send sets of more than one dataset at a time. This way the data could be acquired at cycle time of the PLC which is 1 ms. This option has to be activated in the source code and can be beneficial for modal analysis.

The information about the welding parameters gap force, gap size, rotational speed, torque, reaction forces, and time are available in the PLC of the spindle. The missing information for the data recording is the welding speed and the information necessary for the transformation. For the force sensor transformation mentioned before in Section 4.2.3, the tool centre point (x, y, and z) and the rotational angles of the fourth axis and the work piece coordinate system of the robot are necessary. Since the robotic CNC and the spindle PLC operate in Profibus protocol, the communication could be easily established. Both systems operate in master mode, and a coupler for the two decentralized peripherals

(DP-DP coupler) was used for connection. The starting signal, velocity and position information of the tool centre point, as well as the angles for the force transformation were transferred.
The emergency stop connection was established by wire connection from the spindle to the hardware interface of the T805 and documented in the wiring diagram. Pushing the emergency button on the spindle HMI or on the robot HMI results in sudden stop of the complete system.

4.2.5 Programming T805

The programming of the new T805 robotic system was written completely new. The welding speed was divided in four welding situations: acceleration to warmup speed, travelling with warmup speed, acceleration to welding speed and travelling with welding speed. The speeds and distances were programmed to be parametric. This programing is a great advance in comparison to the manual ramp of the welding speed by increasing the potentiometer manually stepwise, as shown in Figure 17 in the manual acceleration example 1 + 2. With the parametric programming in the spindle described in Section 4.2.2, the welding speed can be ramped up along with the rotational speed and the gap force. These improvements in addition to the start variable, previously mentioned in Section 4.2.4, have positive influence on the repeatability of the conducted welding experiments. This is demonstrated by the automatic acceleration examples 1 and 2 in in Figure 17, which differ only in the starting speed.

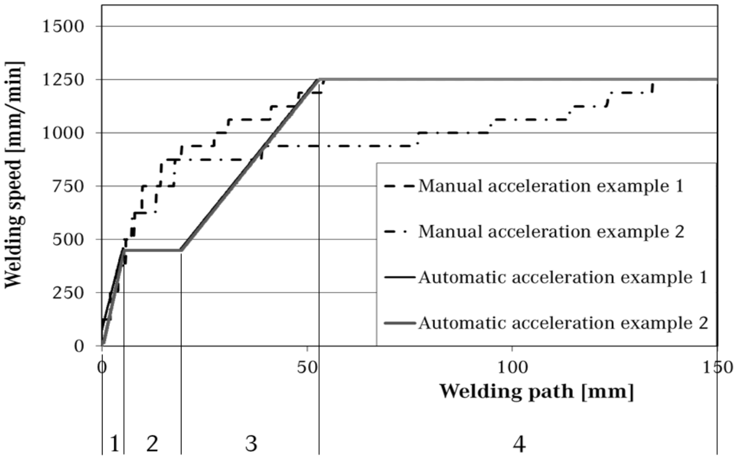

Figure 17. Comparison between manual and automatic acceleration. The welding phases indicated are: 1. acceleration from starting to warmup speed, 2. warmup speed, 3. acceleration to welding speed and 4. welding speed.

4.3 Tool Concept

The manufacture of a new spindle allowed the tool design to be revised. Before the experiments, different tool concepts and designs were evaluated and chosen. In this section, first, the observed challenges with the tool design from Hilgert are described. Afterwards, the new design used in the present study is introduced. An overview of all tool concepts and processes used in the current work is given in Section 4.4.

4.3.1 Previous Tool Design

The tool design developed by Hilgert [1] was a first prototype for the stationary shoulder approach which was limited to the geometry of the shafts of the FlexiStir machine. Three limitations of the tool were deducted from the experience with the tool design of the FlexiStir. First, the disassembly of the tool was challenging. Second, friction between the tool components during the welding led to failure of the tool. As a third difficulty, there was a tilt angle on the lower shoulder and extruded flash formation next to the stationary lower shoulder observed during the experiments, which resulted in cavity defects in the welds. Due to these drawbacks, a demand for the new tool design was derived.

As the first limitation the disassembly of the tool after the experiments was especially challenging because of uncontrolled shifting of components during the welding process that led to difficulties taking the blocked tool apart. For the conventional SRBT process this was described by Hilgert [1]. In the first generation SSBT, which was used firstly in the present study, the lower shoulder was fixed in rotational degree by force fit (Section 3.2.2). The fitting was established by two setscrews applying pressure against the flat contact surface of the probe. This surface is indicated in Figure 8 (a) and the position of the setscrews can be identified in Figure 8 (b). The setscrews of the support of the bearings could loosen during the process and/or turned into the threaded part of the probe. This resulted in the damage of the threads. With the deformed threads of the probe, the disassembly of the bearing support was not possible and all connected parts were likely to be destroyed. Another disadvantage was the pre-set pressure of the small dimensioned setscrews, which was limited. Thus, high torque loads on the screw heads led to failure during assembly and disassembly. Furthermore, in case of bearings failure during the process, it was difficult to line up the holes for inserting the Allen key into the setscrews with the axes of the screws. The lined up shoulder and threads can be seen in Figure 8 (c).

The high loads in axial direction to the probes axis are a major challenge of the stationary lower shoulder design. The distribution of the axial loads only on one of the bearings, as it is the case for the first generation of the SSBT, can result in disadvantages during the welding trials.

As the second limitation the frictional contact between the stationary and the rotating tool components led to failure during the first welding trials with the SSBT process variant. The new requirements for the stationary shoulder are, among others, a probe stiff enough to take the process loads and to not bend to a displacement that the rotating probe contacts the stationary shoulder. In Figure 8 (c) the critical contact area is marked red. In the first set of experiments carried out on the FlexiStir, the probe was destroyed due to friction between the tool steels.

As the last limitation to mention, flash was extruded next to the stationary shoulders to the sides of the weld seam during welds with the first generation of the SSBT.

4.3.2 New Tool Design

The previous design of Hilgert [1] showed good performance according to the conventional SRBT process variant. However, for the new tool requirements the probe and the shoulders were redesigned. Additionally, the SSBT process variant was especially challenging and some improvements were implemented.

4.3.2.1 Probe

The probe represents the most loaded part of the tool system. Concerning the demands of high temperature, high tensile stress and ductility, in the present study the material MP159 was chosen for the probe. It is a Cobalt based alloy, originally developed for the use in aircraft engine components. Good results were reported with this material for welding aluminium alloys [120-122]. Further information about MP159 alloy can be found in literature [123-125].

For cost reasons the setup of the tools was designed modular and several adjustments were introduced such as:

- Bending was minimized;
- A seal from the weld zone to the threads of the probe was implemented;
- Torque transmission was separated from the axial force transmission channels;
- Features were redesigned and tilted to reduce notch effects and induce local small scale vertical flow.

To minimize bending of the new tool generation, the process load was simulated in a mechanical FEM model with a stationary solver. In the model the original design was evaluated as a reference and, additionally, three new designs with different shape and diameter were included. In order to keep the gap between probe and shoulder as small as possible, the concept with the lowest displacement was chosen. The newly designed probe in the configuration of the SRBT can be seen in Figure 18 (a). The SRBT design is also a result of the requirements for the stationary shoulder processes. The dimensions of the rotating lower shoulder could be much reduced, if the probe was used solely for a rotating lower shoulder process. Since the conventional SRBT process was not the main focus of this work, modularity to the other process variants was chosen above the compact design of each tool set.

A limitation of the old design was that the material was pushed into the threads of the lower shoulder. With the new concept, a surface with the tolerance pair of g6-h7 was designed to keep the material away from the threads as showed previously in Figure 15 (a).

The torque transmission is now with a face-centred design at the lower end of the probe, as presented in Figure 18 (c). The torque transmitting ring connects to the lower end of the probe with the lower shoulder and limits the rotational degree of freedom. Residual stresses from thermal expansion during the process can be loosened with a slight turn of this part. The interlocking surfaces are very simple and increase with the applied loads. Furthermore, the contact channel is located in the centreline of the surfaces and not on the damageable edges. If roughened during the process the surfaces are smoothed by the reversed movement of loosening. The notches of features of the probe were smoothened and the features where tilted in the new design to further reduce the bending and reduce the local strain on the surface of the probe.

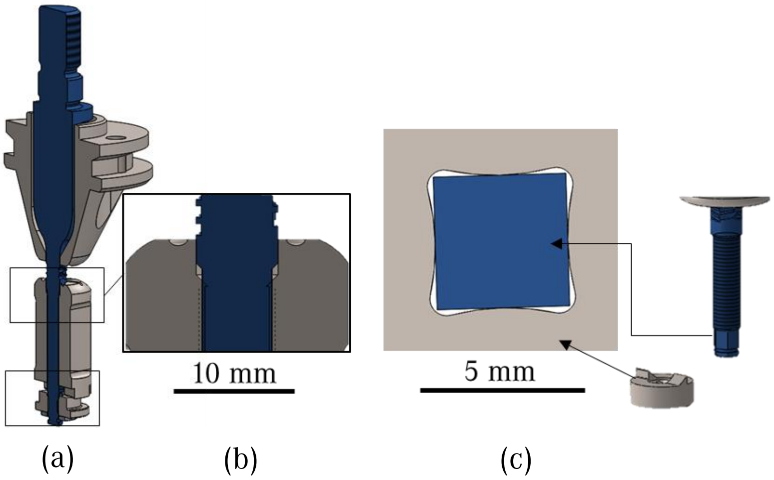

(a) (b) (c)

Figure 18. Conventional SRBT indicating (a) major design changes for better disassembly, (b) fitting of lower shoulder to prevent welded material to reach the threads and (c) probe with face-centred torque transmitting connection.

4.3.2.2 Shoulders

Wear resistance at high temperatures is a major issue for the shoulder surfaces and also for the torque transmitting part. These parts were manufactured from tool steels as Hotvar steel [126], 1.2343 (X38CrMoV5-1) or 1.2344 (X40CrMoV5-1), depending on the ordered workshop. The effects of tool shoulder material on the heat input has been studied by Midling et al. [127]. Effects of the different tool shoulder materials in combination with the welded material could not be observed in the present work.

For a floating upper shoulder, the design of the stationary upper shoulder was adapted as shown in Figure 19 (a). Module design is achieved with the lower part of the upper shoulder being interchangeable for different probe diameters.

The stationary lower shoulder was redesigned in the present work as presented in Figure 19 (b). The shoulder assembly consists of the shell of the lower shoulder, which houses two roller ball bearings on the bearing support. This configuration leads to the distribution of the axial loads on both bearings. The bearing support is kept in place by the torque transmitting ring which was introduced with the probe of the SRBT. A wider stationary shoulder was introduced in the new tool design to control the amount of flash on the RS and the tilt angle experienced with the first design.

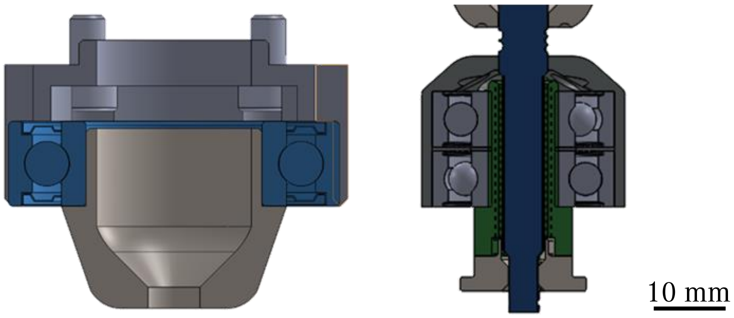

(a) (b)

Figure 19. Stationary shoulders with (a) assembly of the pivot mounted upper shoulder and (b) bearing supported lower shoulder.

The preliminary SSBT experiments showed that, for the experimental research state, conventional industrial roller ball bearings lasted sufficiently to conduct a weld. The combination of high temperature and high axial loads leads to excessive clearance of the bearings after several welding processes. However, a different bearing configuration and dimensioning would increase the service life of the tool system, but lifetime appropriate for industrial application was not a requirement during experimental research.

4.3.2.3 Process Relevant Improvements on the SSBT

Challenges of guiding the material flow in the SSBT process variant required improvements during the experiments. First, small fixed-gap shoulder parts were added to the probe as demonstrated in Figure 20 (a). This design is referred to as stepped probe design and has the purpose of increased contact channels for flow redirection through active guidance. The assembly of the tool with the stepped probe design for the SSBT process is shown in Figure 20 (b).

As a second step, a support for the lower stationary shoulder was designed as presented in Figure 20 (c). The support was used to stabilize the lower shoulder in horizontal level during the experiments. With this design, the shoulder should be kept on a parallel level to the surface of the welded sheets. The implementation of the improvements in the SSBT process development is shown in Section 4.4.2.

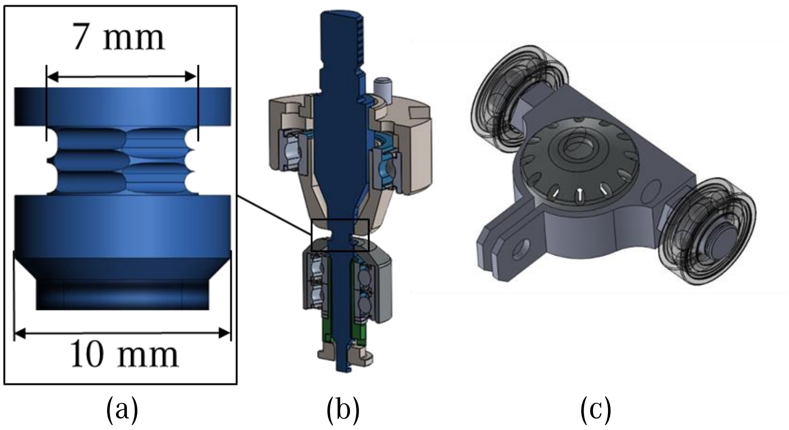

Figure 20. Adaptation for the stationary shoulder bobbin tool (SSBT) process variant: (a) additional rotating shoulder parts on probe with the stepped probe design, (b) assembly with stepped probe design and (c) add-on support for the stationary lower shoulder.

4.4 Process Development

An overview of the conducted process variants and tool concepts is given in Table 2. As baseline experiments, the conventional SRBT process for butt welds was conducted. The welds were done with probe diameters of 6 mm and 7 mm, and with welding speeds in between 120 and 300 mm/min.

To achieve knowledge about the behaviour of stationary shoulders in BT-FSW, first the semi-stationary shoulder bobbin tool (S^3BT) process variants were performed. Depending on the stationary side, the processes are distinguished as S^3BT-SLS for the S^3BT with a stationary lower shoulder and S^3BT-SUS with a stationary upper shoulder. Second, a SSBT tool with the stepped probe design including small additional rotating shoulder parts was introduced, as described in previous Section 4.3.2.3.

To examine the importance of the levelled surface of the stationary shoulder, a supporting sledge was installed which was trailing in two grooves. This add-on support “sledge” was exclusively introduced for the SSBT process, as described before in Section 4.3.2.3. The construction stabilized the lower shoulder by transforming the bending momentum into axial stress on the probe. With this setup it was possible to limit the tilt angle.

The described experiments were all conducted on sheets of 6082-T4 aluminium alloy with thicknesses of 3.0 and 3.6 mm, as presented in Table 2. The experiments for process development were proceeded in three steps. In the first experiments, a parametric research was necessary. As an approach for saving material, the first series were conducted with short bead-on-plate welds. Sheets with dimensions of 190 mm x 150 mm were chosen and three run-in notches were cut in each sheet with a distance of 25 mm from another. Three experiments on each work piece could be conducted in a fast manner, since clamping time was reduced. As a second step, with a suitable set of welding parameters, the experiments proceeded to equally short butt welds. And, as a last step, samples in greater dimensions were welded for the manufacture of tensile testing specimens. For this purpose, two work pieces with dimensions of 140 mm x 380 mm were butt welded.

Table 2. Overview of process variants and used tools, with values presented in mm. The fully rotating conventional self-reacting bobbin tool (Conv. SRBT), semi-stationary shoulder bobbin tool (S^3BT) in stationary lower shoulder (S^3BT-SLS) and stationary upper shoulder (S^3BT-SUS) configuration, and the stationary shoulder bobbin tool (SSBT) with the probe as the only rotating part in straight and stepped probe design configuration

<table>
<tr><th>Process variant</th><th colspan="2">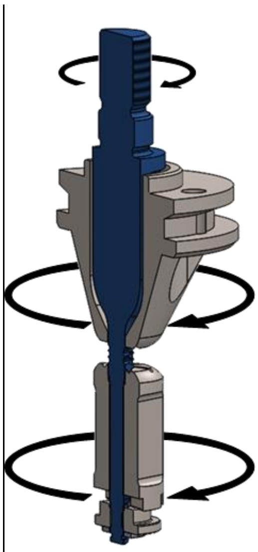
Conv. SRBT</th><th>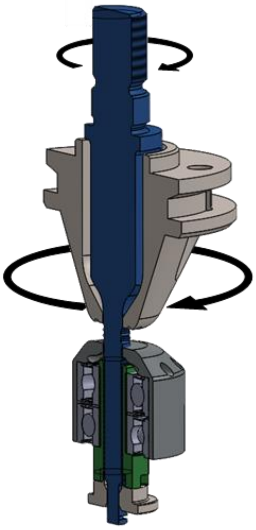
S^3BT-SLS</th><th>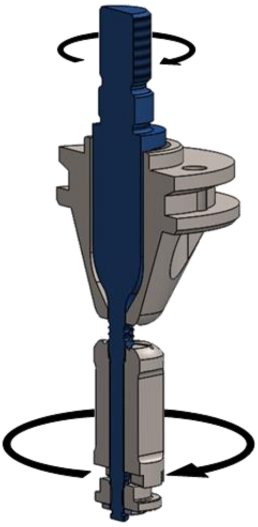
S^3BT-SUS</th><th colspan="2">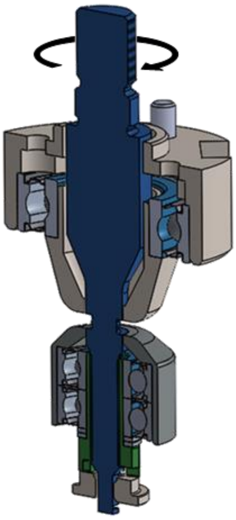
SSBT</th></tr>
<tr><td>Probe [mm]</td><td>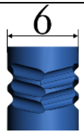 </td><td> </td><td> </td><td>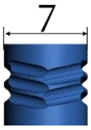 </td><td> </td><td>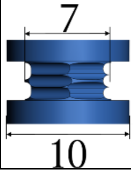 </td></tr>
<tr><td>Add-on</td><td>–</td><td>–</td><td>–</td><td>–</td><td colspan="2">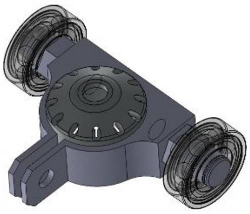</td></tr>
<tr><td>Sheet thickness [mm]</td><td>3.0</td><td>3.0
3.6</td><td>3.0</td><td>3.0</td><td colspan="2">3.6</td></tr>
</table>

A statistic study of parameters, such as Design of Experiments[2], covers wide ranges of parameter sets. It also covers combinations of parameters which can exceed the load capabilities of the tool. Failure of the welding tool can lead to damage of the welding apparatus, therefore a different experimental procedure was chosen for this study. The coordinate search algorithm, which is an iterative method, was used. Changing each parameter individually and in both directions was helpful

---

[2] DOE=Design of Experiments is a statistical plan of experiments with a range of parameters

to determine the influence on the process. After finding the optimum for a single parameter, the next parameter was altered to its optimum successively. The iterative steps for the new parameters were kept small, this way the transfer was kept also small. In total, a number of approximately 700 experiments of five different process variants were conducted: conventional SRBT, S^3BT, and the SSBT with straight and stepped probe design.

The welding parameters were not set constant throughout the welding process. According to the welding process variant, the preheat phase was added in the beginning of the three welding speeds of the phases with the two acceleration ramps mentioned before in Figure 17. These steps were individualized for each BT process variant.

4.4.1 S^3BT

The configuration of the S^3BT-SLS tool consists of the stationary lower shoulder of the SSBT process variant and the upper shoulder of the conventional SRBT process, as seen in Table 2. In the case of the S^3BT-SUS tool assembly, the configuration is the opposite.

For S^3BT-SLS, the lower shoulder of the tool went through an extended preheat phase on the longer sheet in the beginning of the welding path. Welding speeds of 1800 mm/min were reached. Experiments with welding speed below 1000 mm/min led to a dive-in of the rotating shoulder or the welds were not consolidated due to reduced gap force application.

The S^3BT-SUS process variant the experiments reached high welding speeds up to 3000 mm/min. The outcome of the welds show similarities to the inverse process variant of S^3BT-SLS. The main limitation for the S^3BT-SUS process variant in the present work was the maximum torque delivered by the spindle. At the welding speed of 3000 mm/min a reduced rotational speed, which differed from the set value of the controller could be observed. As a safety measure, the welding speed was reduced to 2950 mm/min. At this speed, the rotational speed correlated with the set values. All resulting welds are described in Section 5.1.

A comparison of the tool setup for the S^3BT-SLS process variant to the conventional FSW process can reveal some similarities. At closer observation the difference is the probe, which extends through the work piece, and the lower stationary shoulder, which works comparably to a sliding anvil.

4.4.2 SSBT

The first design of the stationary shoulder BT was created during the work of Hilgert [1]. This design was applied for the first time in the present study, but all experiments with this design resulted in non-consolidated welds. The experimental procedure continued with the new designed tools on the T805 robot. For the SSBT process variant, all welds have been conducted as bead-on-plate welds. The experiments were divided into the SSBT process variant with straight probe design and the stepped probe design, as presented in Table 2.

The tools used on the first set of experiments were with the SSBT with the straight probe design. The focus of the experimental work at that time was to achieve a consolidated weld. As one indication, the gap size was observed during the experiments. The gap size should be slightly lower or at least the same as the thickness of the original work pieces. The experiments were conducted on 3.0 and 3.6 mm sheets and the work pieces have been cut by the probe instead of welded. Probe failure occurred with comparably low gap forces (approximately 60% of S^3BT-SLS) at welding speeds between 40 and 150 mm/min. Approaches with higher welding speeds also turned out without good results. The experiments were extended to use the additional support for the stationary lower shoulder, as seen in Figure 21, and the tilt angle of the stationary lower shoulder was reduced significantly.

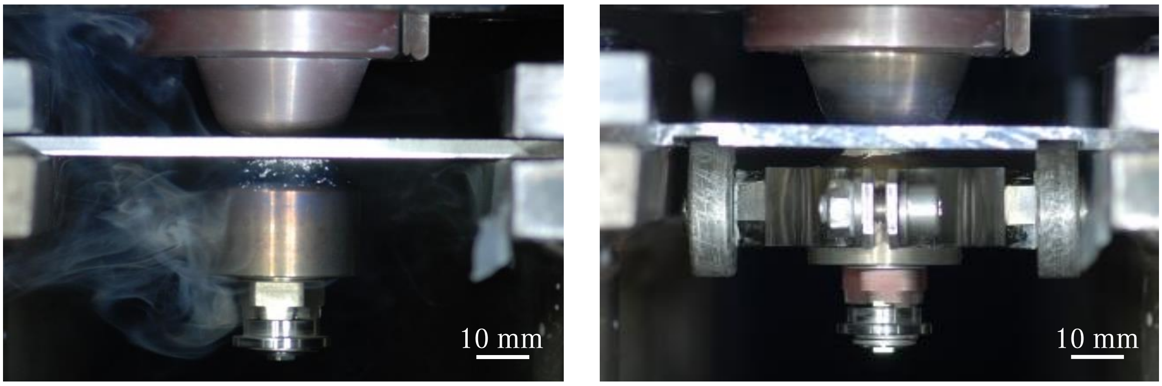

(a) (b)

Figure 21. SSBT process variant with (a) stepped probe design (not visible) and a slightly tilted lower shoulder and (b) a stationary lower shoulder supported through sledge.

The previous welds on 3.6 mm sheets were repeated with the SSBT including the stepped probe design and resulted in a partially consolidated weld. The gap size increased after two-thirds of the welding path to a level above the thickness of the work pieces. The experiments were repeated with the support and also with increased gap force and both trials resulted in consolidated welds. For comparison of all the tool solutions, welds starting with the same parameters were conducted with the different tool approaches. The results of this set of experiments are discussed in Section 5.6.4.

With the stepped design, the alignment of the stepped shoulder parts and the stationary shoulder parts was difficult and could not be proceeded under process loads conditions. Due to this, repeatability of the process with this design was limited.

4.5 Further Experimental Procedures

For the experiments which resulted in good quality welds, further investigation was sought for. The S^3BT process variants were chosen to conduct experiments for flow evaluation. First, the stop action technique was applied on S^3BT-SLS experiments, and second, S^3BT-SUS experiments with marker material were conducted and evaluated by X-ray analysis for Welds 3 and 4 from Table 3. And third, experiments were recorded with an infra-red camera to analyse the temperature field during the process on all welds of Table 3.

Table 3. List of processes evaluated in the thermo camera experiments

№	Process variant	Welding Speed [mm/min]	Rotating shoulder diameter [mm]	Probe diameter [mm]
1	Conv. SRBT	300	10-12	6
2	S^3BT-SLS	1800	14	7
3	S^3BT-SUS	2000	14	7
4	S^3BT-SUS	3000	14	7

4.5.1 Stop Action Technique

In literature, stop action techniques were described frequently [66, 67, 71]. One challenge of the technique is to stop the rotating components, such as the spindle rotor and tool, as fast as possible and remove the tool afterwards without damaging or influencing the microstructure in the weld zone. Commonly the machine is stopped in the middle of the weld. Depending on the author, either the probe is removed or kept in the sample for preparation. One major drawback of this technique is that the machine has a moving momentum which should come to a sudden stop. Even with mechanical breaks on the spindle rotor and with high torque loads on the shoulder and the probe, it cannot be guaranteed that the stop is freezing the image of the material flow in the process. Most stop action reported were done with this technique. A different approach with a broken tool was used in other studies [64, 76], but the welds presented in these cases suffered from insufficient flow around the probe. Yet, this procedure allows to evaluate the frozen microstructure with little disruptive influences.

During the present experimental study, an advance of this technique could be made. Especially in the S^3BT-SLS process variant, failure of the probes was achieved easily at stable process conditions. Since the inertia of the probe is very little and the bearing supported lower shoulder is not participating in the momentum, the probe stopped very sudden. In the experiments, several mechanical limits were evaluated. As an example, the region of the maximum gap force in the welding process was tested by reaching the mechanical strength of the probe. The same procedure was applied for the maximum welding speed, if not limited by the handling system. During the search of these limits for the parameter ranges, breakage occurred as a natural boundary in experimental research. Raising the speed in combination with the axial forces to the limit of the probe, it was possible to achieve failure during a welding process with sufficient flow conditions for parameters similar to weld 2 in Table 3. Yet, the disadvantage of this technique is the destruction of an expensive welding tool.

4.5.2 Marker Material Experiments

In the current development of the process variants with a stationary shoulder, the most difficult step was to achieve the flow from RS to AS on the trailing side of the probe. To research the influence of the rotating shoulder on the material flow, marker material was embedded into the sheets before welding. Furthermore, the occurrence of vertical flow in the BT-FSW with a stationary shoulder was evaluated. The arrangement of the marker material is shown in Figure 22 and was conducted similar to Reynolds [128]. As marker material titanium powder with particle size of 20-63 µm was used according to Zettler et al. [70]. The Ti-powder was embedded through drilled 0.6 mm holes on the faying surface of the work pieces. The holes were approximately 6 mm deep and were drilled in three thickness levels on the top, middle and bottom of the work pieces. A distance of 0.3 mm was kept to the top and bottom surfaces. The application of marker material on RS and AS was shifted to separate the observed transportation on both sides.

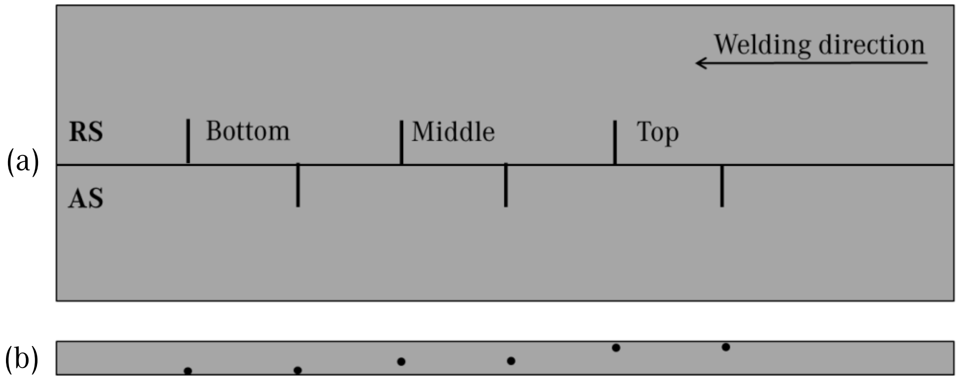

Figure 22. Sketch of the arrangement of marker material on (a) top view and (b) side view.

The marker material experiments were conducted with the S^3BT-SUS process variant with welding speeds of 2000 and 3000 mm/min. The choice of the process variant was made according to experimental stability in the results and to the mandatory butt weld configuration necessary for the arrangement of the marker material.

4.5.3 Temperature Measurements

For the temperature measurements, an infra-red camera type InfraTec ImageIR 8300 was used. The temperatures were controlled with k-type thermocouples at forehand. The temperatures during the experiments were recorded to evaluate the temperature fields during the welds, since there is a direct influence on the degradation of the material in the surrounding. For this purpose, dull black temperature resistant paint was applied on the surface of the tools and of the work pieces. An area of the weld seam dimension was left unpainted. All welds for temperature measurements were conducted with a room temperature handling system and using work pieces with identical dimensions and a length of 380 mm. The welding processes which were monitored by thermo camera are listed in Table 3. The nominal shoulder diameter of the conventional SRBT is 10 mm. Yet, the construction of the tool has convex shoulders exceeding the nominal diameter. During the process, approximately 12 mm of the shoulder were active. In comparison to the shoulder diameter of processes conducted with the 7 mm probe, the shoulder diameter is reduced by 2 mm. Post-weld examination of the diameter of the welds does not to reflect the shoulder diameter due to an oscillating deviation of the handling system perpendicular to the welding direction.

4.5.4 Characterization

The data acquisition for the experiments is described in Section 4.2.4. Metallographic examination was carried out after the experiments. The welds were evaluated through macrographs of the cross sections. For this purpose, the samples were cut by diamond abrasive wheels and embedded in a cold mounting resin (Demotec 30). After embedding, the samples were prepared with a standard procedure. Etching was done with Barker or a modified Keller etchant according to the needs of evaluation. The used optical microscope is a Leica Microsystems DM IRM type.

The procedures and the results for mechanical testing are described in the Appendix B.

5. Results and Discussion

As a consecutive work of Hilgert [1], one of the main objectives is to understand the phenomena taking place in the SSBT process variant. After the evaluation of these baseline experiments with the conventional SRBT, strategies for the stationary shoulder BT experiments were developed. The design with the full stationary shoulder BT turned out to be the most challenging in experimental feasibility. As a strategy, the stationary shoulder was introduced stepwise with different tool designs (Section 4.4). Five different BT-FSW process variants have been conducted with different methods during the experimental phase of the work. Each process included a unique set of challenges and advantages. Section 5.1 gives an overview of the resulting welds from the new process variants. Even though the process variants differ in tool concept and welding parameters, the observations are similar or comparable within some variants. A description of the phenomena observed is given in Section 5.2. Correlation between the observed phenomena and gathered data resulting from the experiments could only be established by numerical simulation, which is described in Section 5.3. The evaluation and interpretation of the results are conducted in Sections 5.4 to 5.6 and the mechanical properties achieved in the different welds are presented in Appendix B.

5.1 Experimental Results of Process Development

In the present study, welds were performed with five different process variants, as previously mentioned. During the experiments for development of the process variants, the main challenge was to reach stable welding conditions. In order to achieve these conditions, welding parameters were altered, such as welding and rotational speed, material thickness and probe design for the different process variants. A visual inspection of the surface appearance of the welds was carried out to understand the influence of these parameters on the stability of the welding conditions. An overview of the surfaces of the welds produced with the different process variants and parameters is presented in Table 4.

Table 4. Overview of surfaces of the welds produced with different BT-FSW variants. The fully rotating conventional self-reacting bobbin tool (SRBT), the semi-stationary shoulder bobbin tool (S^{3}BT) in stationary lower shoulder (S^{3}BT-SLS) and stationary upper shoulder (S^{3}BT-SUS) configuration, and the stationary shoulder bobbin tool (SSBT) with the probe as the only rotating part in stepped and straight probe design configuration

Weld №	Process variant	Material Thickness [mm]	Welding Speed [mm/min]	Probe Design [mm]	Top Surface	Bottom Surface
					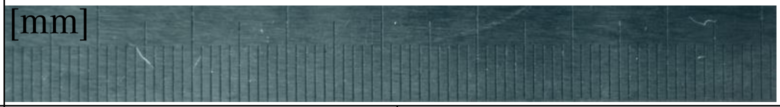	
1	Conventional SRBT	3	120	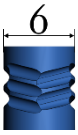		
2		3	300	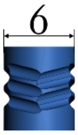		
3		3	300			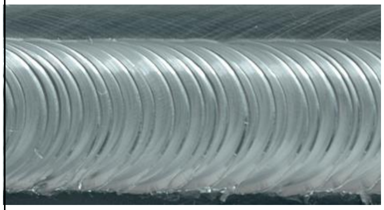
4		3.6	300	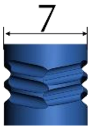	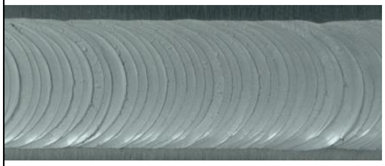	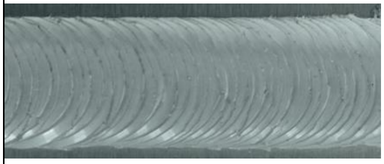
5	S^{3}BT-SLS	3	1800	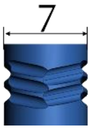	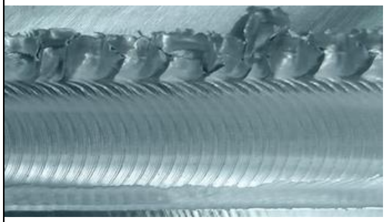	
6	S^{3}BT-SUS	3	1850		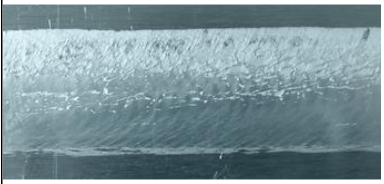	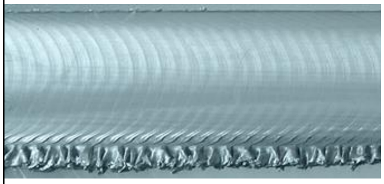
7		3	2000	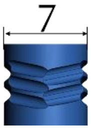	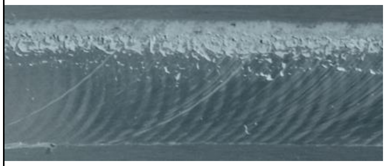	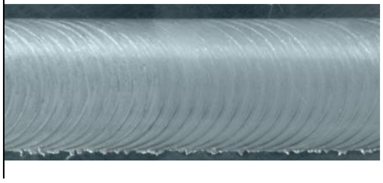

Weld №	**Process variant**	**Material Thickness [mm]**	**Welding Speed [mm/min]**	**Probe Design [mm]**	**Top Surface**	**Bottom Surface**
					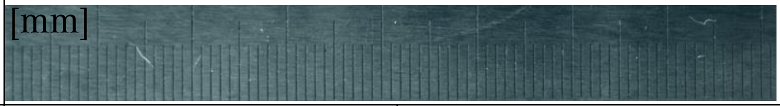	
8	S^{3}BT-SUS	3	2500			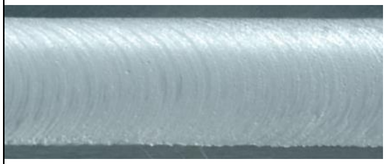
9		3	2950		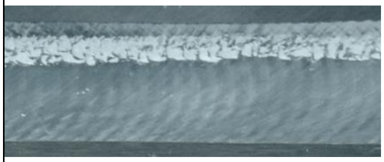	
10	SSBT-stepped	3.6	100	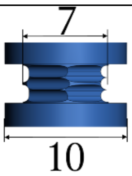		
11	SSBT-straight	3.6	100	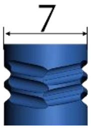	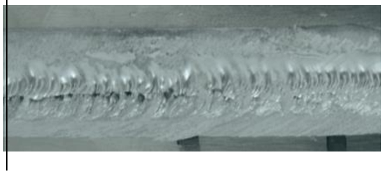	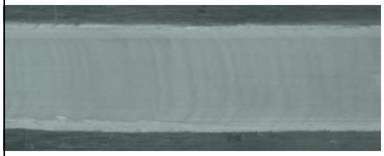

The results obtained for the conventional SRBT process variant are shown in the first four welds of Table 4. This process variant, used as the baseline, present a typical FSW pattern on the top and bottom surface and the surface appearance correlates with an observed oscillating deviation of the spindle from the welding path. The roughness on the surface increased with the increase of the oscillating deviation. The most stable welding conditions for this process were achieved for the weld 1, with a probe diameter of 6.0 mm, a sheet thickness of 3.0 mm, and a welding speed of 120 mm/min, which is comparable to the highest welding speed achieved by Hilgert [1]. In the welds 1 and 2, the increase of roughness on the surface appearance can be observed with the increase of the welding speed from 120 mm/min to 300 mm/min. Further increased welding speeds resulted in unstable behaviour with an oscillating deviation of the handling system perpendicular to the welding direction.

Comparing the welds 2 and 3 in Table 4, the increase of probe diameter from 6.0 mm to 7.0 mm was accompanied with an increased surface roughness. Especially for the weld 3, the oscillating deviation of the handling system was elevated, and excessive flash was produced. The change of thickness from 3.0 to 3.6 mm in the welds 3 and 4 showed a positive effect on the surface quality. Even though these welds were produced with the same tool, the oscillating deviation of the tool perpendicular to the welding direction in the weld 3 resulted in an increased width of 16.8 mm, while the weld 4 presented a width of 13.9 mm.

The weld 5 obtained with the S^{3}BT-SLS process variant showed smooth surface on the stationary side and the typical FSW pattern on the upper side of the weld. The smooth surface appearance is described in the literature as “hot ironing” effect of the stationary shoulder [20, 21, 27, 28]. A good example of a surface with this effect is presented in Figure 23, which was produced in the current work.

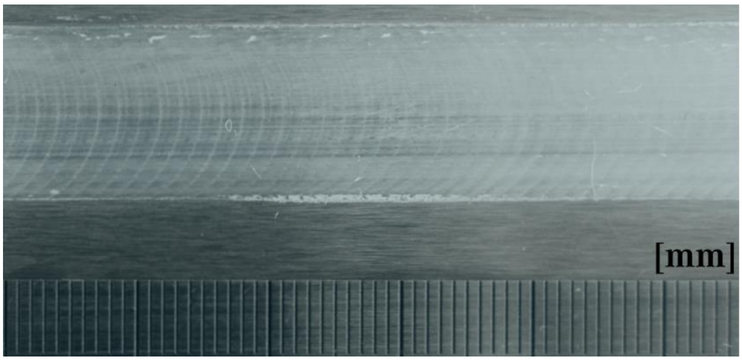

Figure 23. Hot ironing effect on the stationary shoulder side of a weld produced with the S^{3}BT-SUS process variant.

In all the welds performed with S^{3}BT-SLS, the formation of toe flash has been observed on the rotating shoulder side, as seen on the top surface of weld 5 in Table 4. As expected, the characteristics of the weld 6, which was produced with the S^{3}BT-SUS process variant, are comparable to weld 5. This comparison can be done because of the similar tool concept of both processes, as previously shown in Table 2. One difference that can be noticed between welds 5 and 6 in Table 4 is the width of the stationary shoulder side. In the S^{3}BT-SLS the diameter of the stationary shoulder is increased. The reasons for the increase are discussed in Section 5.2.1.

Welds 6 to 9 in Table 4 were performed with the S^{3}BT-SUS process variant. On the rotating shoulder side, the amount of toe flash is smaller than in the S^{3}BT-SLS process variant. Especially when the welding speed increases, as observed in welds 6 to 8 from 1850 mm/min to 2950 mm/min, the toe flash formation is reduced.

For the weld 10, conducted with the SSBT process variant with the stepped probe design, the surface appears matte on both sides of the weld. On the top surface, the typical FSW pattern was replaced by a longitudinal pattern. At the bottom surface it shows increased roughness. For the weld 11 performed with the SSBT process variant with the straight probe design and the support for the lower shoulder, the upper surface shows a cavity, while the lower surface appears smooth.

A comparison between the respective macrographs was done to understand the influence of each process variant on the macrostructure and to control the consolidation of the welds. Table 5 shows the macrographs of the cross section of the welds introduced in Table 4.

Table 5. Overview of the process variants, probe design and macrographs of the conducted welds, The fully rotating conventional self-reacting bobbin tool (SRBT), the semi-stationary shoulder bobbin tool (S^{3}BT) in stationary lower shoulder (S^{3}BT-SLS) and stationary upper shoulder (S^{3}BT-SUS) configuration, and the stationary shoulder bobbin tool (SSBT) with the probe as the only rotating part in stepped and straight probe design configuration

Weld №	Process variant	Material Thickness [mm]	Welding Speed [mm/min]	Probe Design [mm]	Line-energy [kJ/m]	Macrograph AS RS
1	**Conventional SRBT**	3	120	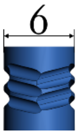	730	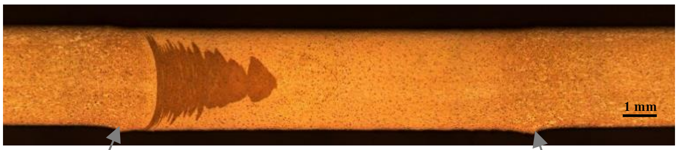
2		3	300	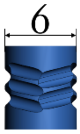	424	
3		3	300		470	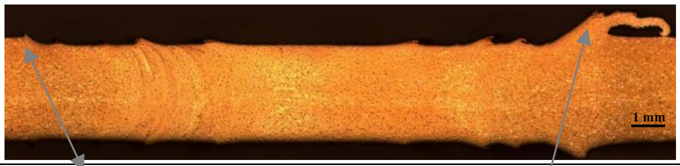
4		3.6	300		460	
5	**S^{3}BT-SLS**	3	1800		164	
6	**S^{3}BT-SUS**	3	1850		134	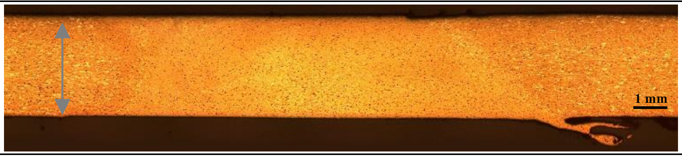
7		3	2000		130	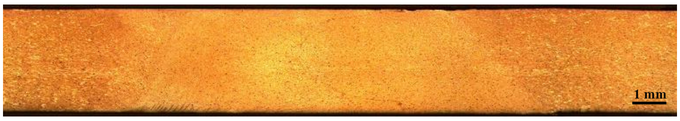
8		3	2500		115	
9		3	2950		104	

Weld Nº	Process variant	Material Thickness [mm]	Welding Speed [mm/min]	Probe Design [mm]	Line-energy [kJ/m]	Macrograph AS RS
10	**SSBT-stepped**	3.6	100	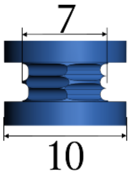	930	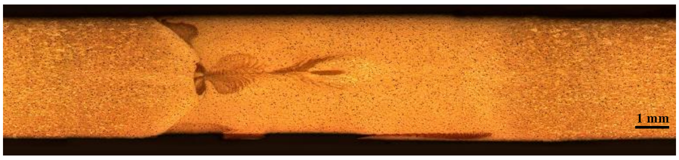
11	**SSBT-straight**	3.6	100		950	 AS RS

As indicated in Table 5, an unusual increase of the area of the SZ with the increase of the welding speed was observed for the welds 1 and 2 produced with the conventional SRBT process variant. This behaviour can be a result of the oscillating deviation of the welding spindle perpendicular to the welding direction, as described earlier for weld 2 in Table 4. Since the same tool was used to produce these welds, the indicated change in the imprint of the shoulder supports this assumption. From weld 3 to 4, conducted with an increased probe diameter, there was a reduction of the imprint of the shoulder, as pointed in Table 5. This also supports the visual observation of the reduced oscillating deviation of the welding spindle during the experiments. The symmetrical convex shape of the SZ in weld 4 is typical for a conventional SRBT joint and was also observed by Hilgert [1].

The notable difference of the S^{3}BT-SLS process variant when compared to the conventional SRBT is the strong asymmetry of the SZ, according to weld 5 in Table 5. There is a horizontal asymmetry since the area of the SZ on the RS is wider than the area on the AS. Moreover, there is a vertical asymmetry due to the influence of the rotating upper and stationary lower shoulder. The upper shoulder was tilted to the lower shoulder and also to the surface of the work pieces during the welding process. The penetration of the upper shoulder indicated in the macrograph resulted in a reduced thickness of the weld on the RS. The reasons for the tilt angle are discussed in Section 5.2.1.

The macrograph of weld 6 conducted with the S^{3}BT-SUS process variant has a mirrored appearance to weld 5. The same was observed in the surface appearance of these welds in Table 4. The stationary and rotating shoulder surfaces are parallel, since a tilt angle was not applied. As shown in the macrographs of the welds 6 to 9 obtained with the S^{3}BT-SUS process variant, the SZ area is reduced with increasing welding speed between 1850 and 2950 mm/min. A comparable relation between welding speed and SZ has been observed in literature [44]. Commonly, in conventional FSW there is a reduction in thickness of the weld zone due to the penetration of the tool, and this is also observed for BT-FSW. In the case of SSFSW, this penetration could be reduced, but was still observed and reported in literature [20, 21]. The penetration of the stationary and rotating shoulder was minimized in the present work with the S^3BT-SUS process variant, especially in the welds 8 and 9. In comparison to the other BT-FSW variants, the line-energy is reduced for all welded specimens with the S^3BT variants as seen in Table 5.

The macrographs of welds 10 and 11 of the SSBT process variant are also shown in Table 5. Weld 10 was performed with the SSBT process variant in the stepped probe configuration and the additional support for the stationary lower shoulder, while for weld 11 the SSBT process variant with the straight probe design and the support was used. The influence of the shape of the probe design can be seen on the AS, where the transition between the SZ and the TMAZ is abrupt. In direct contrast, the transition on the RS is comparable to the conventional SRBT welds. In the macrograph of weld 11, additionally to the presence of cavities, a harsh and straight transition on the AS can be observed. Furthermore, the thickness of this weld increased on the RS and on the AS, as indicated in the macrograph. This can also be observed through the gap size values recorded during the experiments, as described in Section 5.6.4. The reason for this increased thickness due to accumulation of material is discussed in Section 5.5.3. A comparison of the macrostructure of the welds and the velocity fields from the CFD model is established in Section 5.3.3

5.2 Observed Phenomena

There is a strong dependency between insufficient flow in BT-FSW and material loss from the SZ. This dependency can be explained with the volume consistency during the welding process. Leaving thermal expansion aside, if the volume of material in the SZ remains constant, no cavity defect could occur. Furthermore, the consequences and the possibilities to suppress the phenomena concerning material loss from the SZ are listed in the flow chart of Figure 24. In the present section, the factors affecting material flow in BT-FSW are described. The sections are divided according to the main phenomena related to material loss from the SZ. According to the flow chart of Figure 24, these are accumulation of the material on RS, entrapment in tool, and toe flash formation.

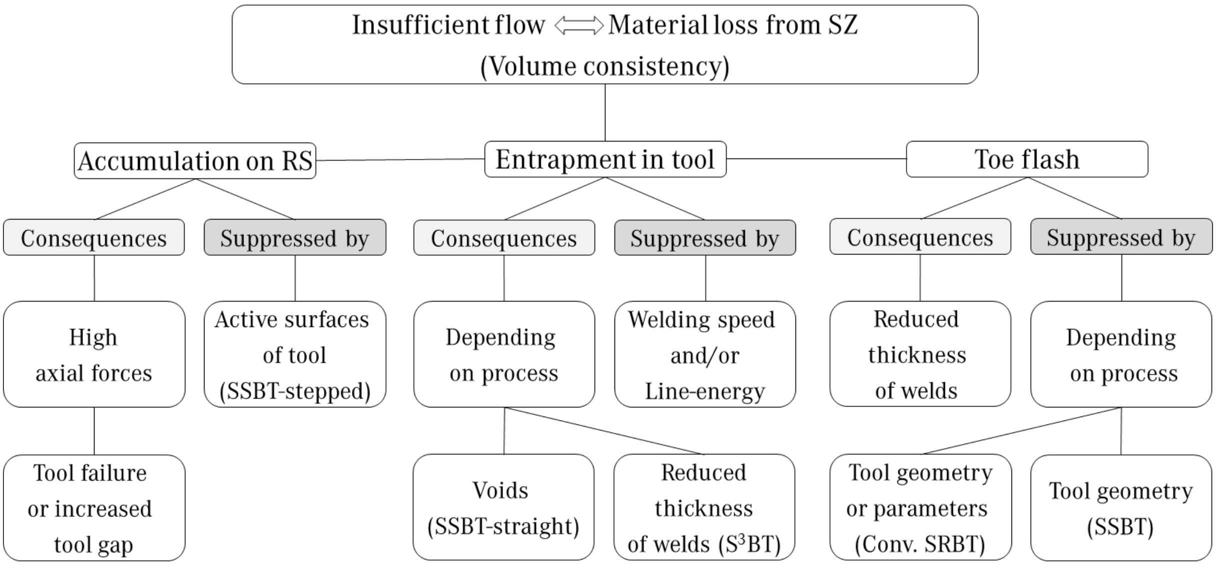

Figure 24. Flow chart of the main phenomena related to material loss from the SZ.

5.2.1 Material Loss due to Accumulation on the RS

The accumulation of material on the RS can be caused by a tilt of one of the shoulders of the tool. A tilt of the lower shoulder was observed during the experiments with the S^{3}BT-SLS and the SSBT process variants. Okamoto et al. [40] also observed an accumulation of material on RS in the macrographs for the fixed-gap BT process variant.

Results of a bead-on-plate weld conducted with the SSBT process variant with the straight probe indicated that this accumulated material can be the cause of the cavity defects observed in the macrograph of Figure 25. A thickness variation can be observed, reaching a maximum at the RS. Moreover, the surfaces of the weld are not parallel to each other. In the experiments, a tilt of the lower shoulder was observed in relation to the upper shoulder, as demonstrated in the scheme shown in Figure 26 (a). This way, the material was accumulated on the RS and left cavities in the centre of the weld. With the accumulation of material on the RS, the gap size of the tool started to increase. The application of higher gap force did not result in an improvement of the material flow. In several cases, the gap force was adjusted until the point of probe failure. Welding process stability could not be achieved in any welding trial with the SSBT including the straight probe.

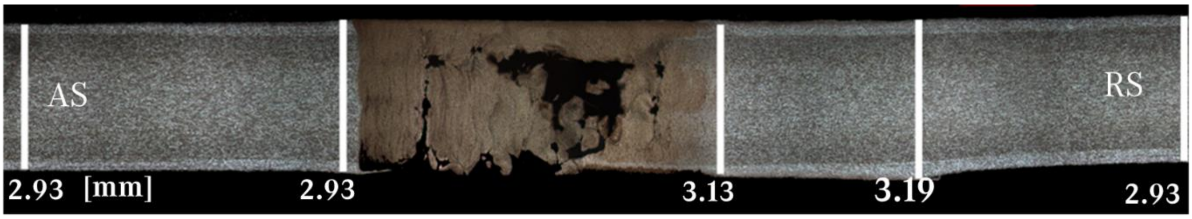

Figure 25. Macrograph of the cross section of a weld produced with the SSBT process variant in straight probe configuration with a tilted stationary lower shoulder.

In the conventional SRBT and S^{3}BT process variants, however, there were strategies for achieving and also recovering process stability after insufficient flow conditions occurred.

As shown by Okamoto et al. [40] with fixed-gap BT-FSW process variant and also seen in the weld 5 produced with the S^{3}BT-SLS process variant (Table 4 and Table 5), the accumulation of material on the RS still allowed the consolidation of the welds. This was only possible because of two new strategies introduced in the welding procedures to reduce the material loss due to accumulation on the RS.

The first attempt was a correction of the angle of the lower shoulder, carried out through the use of a wider shoulder. As indicated in Figure 26 (b), a wider lower shoulder leads to a reduction of its tilt angle, and results in a pressure on the RS. This pressure is produced through the applied lever from the supporting rigid material on the AS transported to the RS. This procedure reduced the formation of cavities, but did not lead to the consolidation of a defect free weld. As a second attempt, a tilt angle was applied on the upper shoulder according to Figure 26 (c). Through the bending of the probe, an additional pressure was applied on the RS on the bottom surface of the material by the stationary lower shoulder. Through this configuration, the rotating upper shoulder could penetrate the material on the AS, reducing the thickness on the AS and producing an elevated amount of flash on the RS at the top surface of weld 5. The stationary lower shoulder is not able to penetrate the material and is parallel to the bottom surface.

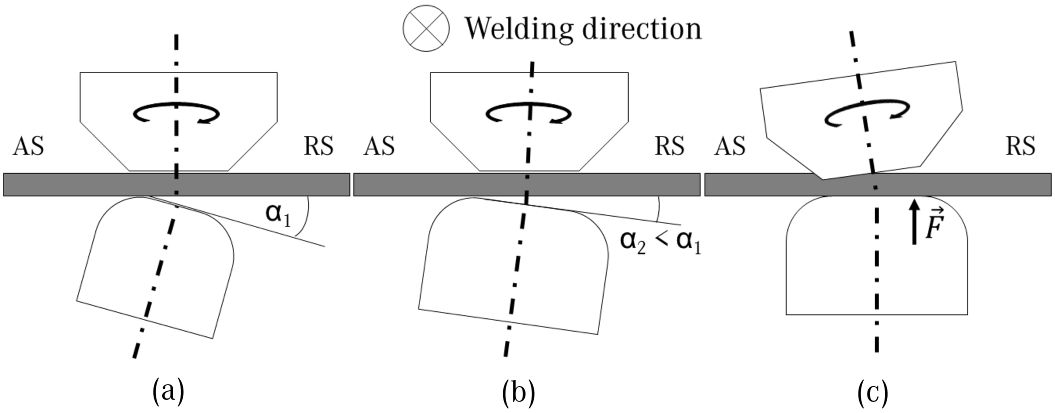

Figure 26. Schematic drawing of the S^{3}BT-SLS experiments with (a) a tilted lower shoulder, (b) reduced tilt angle through wider lower shoulder and (c) tilted upper shoulder to increase pressure on RS.

For the SSBT process variant, the tilted lower shoulder was reduced with wider shoulders in the stationary side and a support of the stationary lower shoulder, as previously introduced in Section 4.3.2.2. As a result, the material accumulation was balanced between the AS and RS, but not avoided. The resulting welds still presented cavity defects, as it can be seen for weld 11 (Table 4 and Table 5).

Studies in literature are not as focused on the accumulation of material on the RS as the present study. This might be a result of the influence of the pressure distribution which is more severe in BT-FSW than in conventional FSW. The offset of the pressure to the tool axis is not as problematic as in conventional FSW, because it can be compensated in the experimental procedure by an adjustment of the tilt angle of the tool. It can be assumed that the accumulation of material on the RS could also occur, but it was never such a challenge to correct the resulting tilt angle of the tool. Explanations for the elevated forces and the accumulation of material on the RS are discussed in Section 5.5.3.

5.2.2 Material Loss due to Entrapment in the Tool

Hilgert [1] reported material loss due to entrapment between the shoulders and the probe. In the present work, the material loss could be compensated in the conventional SRBT and S^{3}BT process variants by adjusting the self-reacting tool gap. For the SSBT process, this compensation is not feasible and any material loss results in cavity defects in the welds. Since the shoulders are not rotating, they cannot penetrate the work pieces. Consequently, there is no compensation of the material loss through reduction of the weld thickness by reduction of the gap size. Especially with wide stationary shoulders, the radii of the shoulders are bigger than the softened material around the SZ and the solid material does not allow any penetration of the shoulders. Additionally, the area of the shoulders is bigger and a higher gap force must be applied to achieve the same amount of pressure. This demands forces beyond the mechanical limitations of the probe.

In the SSBT process, the movement of the probe needs to be separated from the stationary shoulders. This separation is done by two gaps for clearance around the probe, which make the material loss from the SZ inevitable. Through these clearances, which are geometrically direct in the vicinity of the SZ, material can be transported and entrapped inside the tool in this region, as shown in Figure 27.

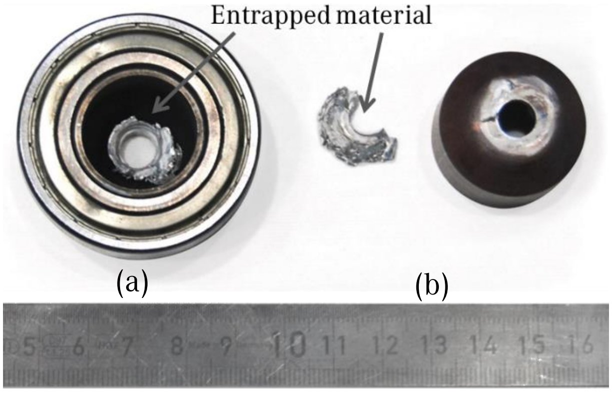

Figure 27. Entrapped material in the SSBT porcess variant with the straight probe (a) in the upper shoulder and (b) removed from inside of the lower shoulder.

The amount of entrapped material in the shoulders was increasingly observed with the straight probe. The magnitude of entrapped material for the S^{3}BT variants was decreased, even though the exact same design[3] of the tool components was used during the welds. Also the amount of entrapped material for the SSBT process variant with the stepped probe design was not as high as with the straight probe design. This matter is further discussed in Section 5.5.3.

5.2.3 Material Loss due to Toe Flash

The material loss is commonly reported in literature as toe flash [129]. For the present study, toe flash was observed in some welds on the side of the rotating shoulder. In the conventional SRBT welds, the toe flash can result from inadequate parameter sets. Also, it can be a consequence of an unsuitable tool geometry for the base material in question. An example for the latter is displayed in weld 3 (Table 4 and Table 5). Another example of toe flash can be found on the upper surface of weld 5 produced with the S^{3}BT-SLS variant (Table 4). For this process variant, all welds performed in the current work included toe flash. The cause can be the material transport from the penetrated AS to the open angle on the RS due to tilt angle of the upper rotating shoulder, as shown in Figure 26 (c).

5.3 CFD Modelling

In the present work, computational fluid dynamics (CFD) modelling was used for process understanding and interpretation of the experimental results. The comprehension of the flow during the FSW process can be the key aspect to a successful weld with a new process variant. The challenges of generating a physical environment in the weld zone, which leads to a consolidated weld, could be observed in the first experiments with the SSBT process variant. With the new SSBT with the stepped probe design including more active surfaces in the weld zone, there were indications how the process can successfully produce a continuous weld, as described in Section 5.2. However, the information gained by the observation methods during experiments is limited. The scope of observations included the measured temperatures and forces during the welds, the mechanical behaviour of the tool, and the post-weld condition of the material. Simulation can be a powerful tool to make an extrapolation from known processes to unknown process variants of an ongoing research. The scope of the simulation is focused on the difference of the obtained shear layers in the weld zones for the different

---

[3] The same probe and shoulders were used for the S^{3}BT and SSBT process variants

tool configurations. The aim of the modelling in the present work was to find evidence which can explain the phenomena observed in the experiments.

The behaviour of the studied conventional SRBT process was used as the initial reference. Through a comparison of the CFD model of the conventional SRBT variant generated during the present work to the conventional SRBT experiments, a good baseline could be set for the new process variants. The simulation results of the different processes were compared to each other and also validated against the experimental results reported in Section 5.3.3.

5.3.1 Governing Equations

As a common approach for CFD simulations, COMSOL Multiphysics uses the Navier-Stokes equation [130, 131] to solve the state of a fluid at each node. In the Nabla operator notation, the Navier-Stokes equation for incompressible fluids is given in Equation (8). The equation basically consists of a balance of forces. On the left side, there are the forces of inertia. On the right side, there are the forces applied on or within the fluid: pressure forces, forces through the viscosity and other body forces. The equation implements momentum, mass and energy conservation.

$$\rho \frac{\partial \vec{u}}{\partial t^*} + \rho(\vec{u}\vec{\nabla})\vec{u} = \vec{\nabla}\left[-p\mathrm{I} + \eta\left(\vec{\nabla}\vec{u} + (\vec{\nabla}\vec{u})^T\right)\right] + \mathrm{F} \tag{8}$$

In the equation, the variables are the frozen time t^*, the density ρ, the velocity vector $\vec{u}$, the pressure p, the viscosity η, and the volume force vector F. The term "$\rho(\vec{u}\vec{\nabla})\vec{u}$" is called the Stokes term for inertia. The inertia of the circular flowing material resolves in pressure on the outer material. The simulation in this study was conducted with and without the Stokes term. The differences were not significant and the simulation was continued with the Stokes term set to zero.

5.3.1.1 Effective Viscosity

The effective viscosity has a governing influence on the output of the CFD simulation for FSW. The viscosity model should replicate the behaviour of the material under specific physical conditions. Hence, the effective viscosity models depend on variables and material parameters. The variables strain rate and temperature have main influence on the viscosity. The relation for a non-Newtonian fluid in between the effective viscosity η_{eff}, the flow stress $\bar{\sigma}$ and the effective strain rate $\dot{\bar{\varepsilon}}$ is given in Equation (9) [92, 132].

$$\eta_{eff} = \frac{\bar{\sigma}}{3\dot{\bar{\varepsilon}}} \tag{9}$$

The most common approach for $\bar{\sigma}$ is given in the constitutive Equation (10), described by Sheppard [103-105].

$$\bar{\sigma} = \frac{1}{\alpha}\, ln \left\{ \left(\frac{Z}{A}\right)^{\frac{1}{n}} + \left[1 + \left(\frac{Z}{A}\right)^{\frac{2}{n}}\right]^{\frac{1}{2}} \right\} \tag{10}$$

It is based on the material parameters n, A, and the Zener-Hollomon parameter Z, which is defined in Equation (11).

$$Z\,(T, \dot{\varepsilon}) = \bar{\dot{\varepsilon}}\; exp\left(\frac{Q_a}{RT}\right) \tag{11}$$

Z is depending on the shear rate $\dot{\gamma}$, the material parameter Q_a, the gas constant R, and also on the temperature T. The relation between $\bar{\dot{\varepsilon}}$ and $\dot{\gamma}$ in Equation (12) was derived by Schmidt [133].

$$\bar{\dot{\varepsilon}} = \frac{\dot{\gamma}}{\sqrt{3}} \tag{12}$$

Inserting the Equations (10), (11), and (12) in Equation (9) results into the shear rate $\dot{\gamma}$ and temperature T dependent effective viscosity η_{eff} of Equation (13).

$$\eta_{eff} = \frac{1}{\sqrt{3}\dot{\gamma}\alpha}\, ln \left\{ \left(\frac{\dot{\gamma}\; exp\left(\frac{Q_a}{RT}\right)}{\sqrt{3}A}\right)^{\frac{1}{n}} + \left[1 + \left(\frac{\dot{\gamma}\; exp\left(\frac{Q_a}{RT}\right)}{\sqrt{3}A}\right)^{\frac{2}{n}}\right]^{\frac{1}{2}} \right\} \tag{13}$$

It was shown in literature, for example by Colegrove et al. [97], that it is possible to find a good agreement between the CFD simulation with this effective viscosity model and the experiments. Thus, it is used in many CFD studies [72, 86-88, 90-92, 98-101, 106]. This effective viscosity can be reformulated according to the relation of the inverse hyperbolic sin law ($sinh^{-1}$) in Equation (14).

$$sinh^{-1}(x) = \; ln\left\{x + [1 + x^2]^{\frac{1}{2}}\right\} \tag{14}$$

The mathematical identity between the effective viscosity based on the natural logarithm (ln) in Equation (13) and the effective viscosity based on $sinh^{-1}$ in Equation (15) is also mentioned by Colegrove et al. [93]. The description of the latter was also used in literature [1, 50, 107, 108]. In the present study, both equations were implemented. The plots of the effective viscosity models based on ln and $sinh^{-1}$ are shown in logarithmic proportions in Figure 28 (a) and (b) respectively. The plots were produced in the ranges for the temperature from 300 K to 900 K and for the shear rate from 0 s^{-1} to 10^3 s^{-1}.

$$\eta_{eff} = \frac{\sinh^{-1}\left(\frac{\dot{\gamma}\, exp\left(\frac{Q_a}{RT}\right)}{\sqrt{3}A}\right)^{\frac{1}{n}}}{\sqrt{3}\dot{\gamma}\alpha} \tag{15}$$

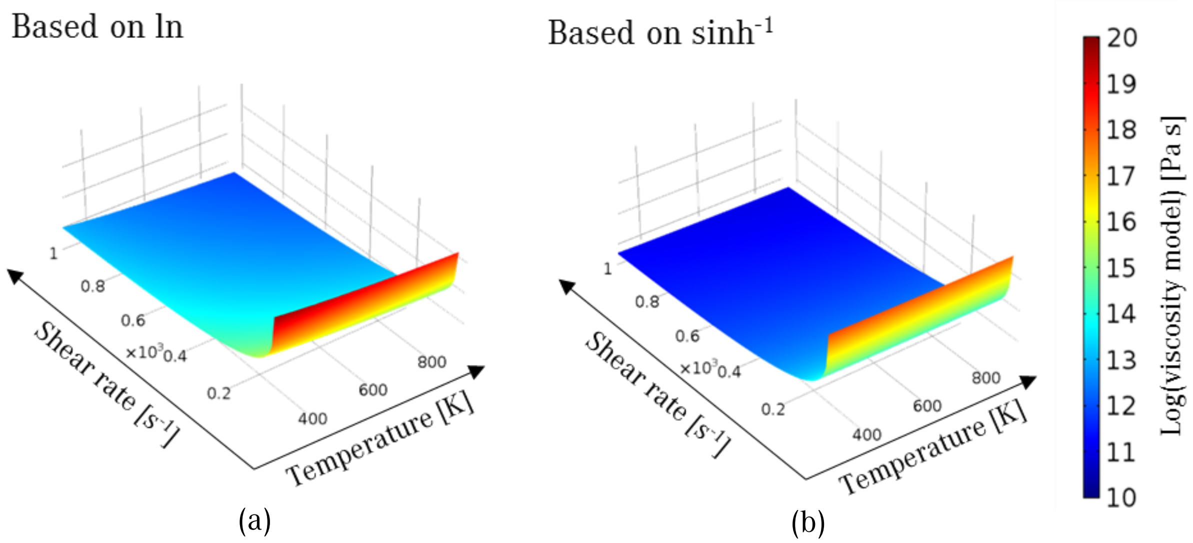

Figure 28. Plots of the effective viscosity models calculated with (a) natural logarithm ln and (b) inverse hyperbolic sin law $sinh^{-1}$.

Both effective viscosity models depend on variables and material parameters. The variables can be evaluated during the calculation of the simulation. Yet, the material parameters, which mostly depend on variables of the physical conditions in the weld zone, need to be received from other sources. Zhang et al. [114] showed that the material parameters n, A, and Q_a are highly dependent on the strain rate and temperature. In FSW, the material suffers elevated strain and strain rates. Zhang et al. suggested adapting the material constants according to the strain for the AA6082 in T4 temper condition, the same as used in the present study. For this material, parameters acquired experimentally are available covering the strain rates from 0.1 to 0.7 s^{-1} presented by Zhang et al. [114]. The values of strain given on experimental basis do not cover the strain rates which are active during the welding process. Strain rates in FSW around 200 s^{-1} were reported in literature [134-136]. Other authors predicted lower strain rates of 9 s^{-1}, 16 s^{-1} and 80-90 s^{-1} [84, 137, 138]. Furthermore, there are studies with parameters implemented that are depending on variables, such as temperature and strain rate [108, 114, 139]. For the present model, the approach of McNelley et al. with a comparison of different parameter sets was used on the available sources [134]. The best agreement of the received velocity field to the macrostructure of the experiments was achieved with the parameter set of the highest strain rate from Zhang et al. [114]. The results are presented in Section 5.3.3.

The simulation was conducted expecting laminar flow conditions. Schmidt introduced a way to calculate the Reynolds number (Re) for FSW application [133]. Since the lower limit of the effective viscosity in the current work was chosen comparably small ($minimum\ of\ 10^2\ [Pa\ s]$) and in addition the rotational speed during the experiments was uncommonly high, the Re was re-evaluated for the present conditions and calculated according to Equation (16).

$$\mathrm{Re} = \frac{\rho\, \vec{U}\, \mathrm{L}}{\eta} \tag{16}$$

Herein ρ is the density, U denotes a velocity scale, and L denotes a representative length. According to Schmidt the velocity for the FSW process can be evaluated with the angular velocity ω assuming stick conditions (contact state variable $\delta = 1$) on the probe's surface and the radius of the probe R_{probe} representing the length, what leads to Equation (17).

$$\mathrm{Re} = \frac{\rho\, \mathrm{R}_{probe}\, \omega\, \delta\, \mathrm{R}_{probe}}{\eta} = \frac{\rho\, {\mathrm{R}_{probe}}^{2}\, \omega\, \delta}{\eta} \tag{17}$$

Using the minimum probe[4] for the fluid domain, the minimum of the effective viscosity reached (≈ 5 $[kPa\ s]$) is evaluated from the modelled weld with the highest speed gradients. The applicability of the laminar flow condition was individually reinsured in post simulated conditions: with the rotational speed and the radius of the used probe during the experiments, the Re reaches a value of approximately $1.1\ 10^{-3}$. Since the returned value is below the critical value expected for turbulent flow, a laminar model can give sufficient resolution of the flow conditions simulated. The laminar flow condition is supported by results of the marker material experiments presented in Section 5.6.1.

5.3.1.2 Temperature Fields

Zettler [8] made the following statement about the importance of the temperature field during FSW: "The reader will very quickly discover that, through the following discussion of heat and material flow, that joint formation is subject to a specific thermal environment, …". In the present study, the temperature field was separately solved with COMSOL Multiphysics software in a "heat transfer in solids" physics environment. The temperature of the SZ was calculated through the heat transfer according to Equation (18).

$$\rho C_p\, \vec{u}\ \vec{\nabla}\mathrm{T} = \vec{\nabla}\ \left(\mathrm{k}\vec{\nabla}\,\mathrm{T}\right) + \mathrm{Q} \tag{18}$$

In the equation, the variables are the specific heat capacity C_p, the thermal conductivity k, the temperature T, and the heat Q. In FSW, the generated heat during the process is a function of temperature. The heat generation reduces drastically close to the melting temperature of the plasticized material. An elaborate way to generate the heat source in friction stir welding is through the dissipation energy of the plasticized material as proceeded by the thermal-pseudo-mechanical heat source of Schmidt et al. [95, 133, 140-142] which is derived in Equations (19) to (28). For this, the contact state in the FSW process is categorized in two ways: one is pure sliding condition in

---

[4] Refers to a probe for physical parameter evaluation implemented in the boundaries or domains of the model and not the component of the tool "probe"

between tool and material matrix and the heat is generated only by friction. In the second state, sticking condition, the material is transported along with the probe and the dissipation of the material produces heat in correlation to the yield stress. Assuming that the welding speed is neglectable in comparison to the rotational speed of the tool ($v_{weld} \ll v_{tool}$) and, therefore, has little influence on the velocity of the material matrix, a contact state variable δ was introduced by Schmidt et al. [140, 141] as presented in Equation (19).

$$\delta = \frac{v_{matrix}}{v_{tool}} = \frac{\omega_{matrix}}{\omega_{tool}} \tag{19}$$

The slip rate $\dot{\varsigma}$ between the surface of the probe and the material matrix includes the same velocities as the contact state variable δ:

$$\dot{\varsigma} = v_{tool} - v_{matrix} \tag{20}$$

$$v = \omega r \tag{21}$$

Inserting Equation (20) into Equation (21) and resolving results in Equation (22).

$$\dot{\varsigma} = (1\text{-}\ \delta)\ \omega_{tool}\, r_{tool} \tag{22}$$

Shear stress induced by friction $\tau_{friction}$ is defined by Equation (23).

$$\tau_{friction} = \mu p \tag{23}$$

The heat induced by friction $q_{friction}$ is defined through Equation (24).

$$q_{friction} = \tau_{friction}\ \omega\ r \tag{24}$$

The total heat input due to the rotation of the tool q_{rot} consists out of the heat input due to frictional heat and the heat input due to dissipation of the material. Heat input can be expressed by velocity multiplied by the shear stress τ_{yield} as in Equation (25).

$$q_{rot} = \dot{\varsigma}\tau_{friction} + (\omega r - \dot{\varsigma})\tau_{yield} \tag{25}$$

Using equations (21), (23) in (25) results in equation (26).

$$q_{rot} = \omega r\ ((1-\delta)\mu\, p + \ \delta\tau_{yield}) \tag{26}$$

With material transport involved ($\delta \neq 0$) the shear stress at the interface $\tau_{interface}$ is in equilibrium with τ_{yield} and $\tau_{friction}$.

$$\tau_{interface} = \tau_{yield} = \tau_{friction} \tag{27}$$

Inserting Equations (27) and (23) into (26), the total generated heat on the rotating boundaries becomes independent from the Columb friction coefficient μ in Equation (28) as introduced by Schmidt et al. [95, 140, 141].

$$q_{rot} = \omega_{tool}\ r\ \tau_{yield} \tag{28}$$

For the higher welding speeds, the heat source was extended on the stationary shoulder for the heat input of the friction induced by the sliding q_{slide} as seen in Equation (29).

$$q_{slide} = \vec{u}_{weld}\ \tau_{yield} \tag{29}$$

A convective heat transfer due to the moving material was implemented with an analytical shear layer model (ASLM) originally introduced also by Schmidt et al. [142]. The ASLM simulates the convection of the heat transfer due to the material flow around the probe. To avoid numerical costly calculation, the velocity is defined in a two dimensional pattern, which is rotated around the probe. For the conventional SRBT process variant, the equations from Hilgert et al. [29, 34] were applied.

For the S^{3}BT process variants, as well as for the SSBT, the equations were adapted to fit the observed macrostructure of each process variant. The tangential velocity v_{tan} of the shear layer around the probe was described in the area in between the shoulders indicated with the black rectangle and darkened area in Figure 29 (a).

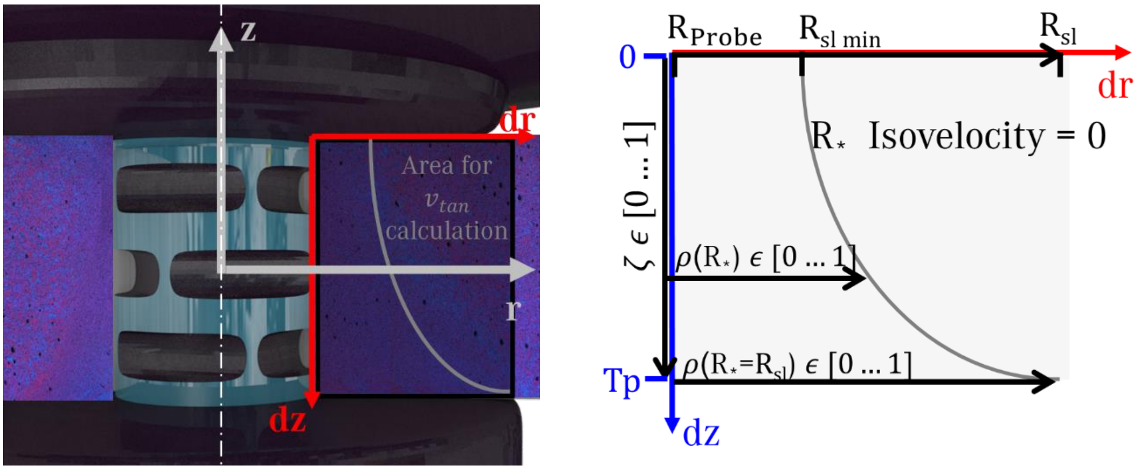

(a) (b)

Figure 29. Development of S³BT-SUS analytic shear layer model (a) coordinate systems and (b) restricted subset area for definitions of shear layer velocities.

An introduction of new coordinates dr and dz and their normalized coordinates ρ and ζ allow the definition of the v_{tan} in the subset area shown in Figure 29 (b). These coordinates are defined for the S^{3}BT-SUS process variant by Equations (30) to (33).

$$dr\ = r\ -\ R_{Probe} \tag{30}$$

$$dz\ = \frac{T_P}{2} +\ z \tag{31}$$

The normalized coordinates of ρ and ζ introduce restricted ranges of values between 0 and 1 in which T_P is the thickness of the work pieces.

$$\rho = \frac{dr}{R_* - R_{Probe}} \tag{32}$$

$$\zeta = \frac{dz}{T_P} \tag{33}$$

The line which is defined by the function R_* defines the outer boundary of the stirred zone and describes the shape of the shear layers in Equation (34). R_* depends on the height ζ and defines the point where no material is transported anymore ($v_{tan} = 0$) on the ρ-axis. The exponent m_{shape} controls the shape of the boundary of the shear layers.

$$R_*(\zeta) = (1 - \zeta^{m_{shape}})\ R_{sl} + (\zeta^{m_{shape}})\, R_{sl\,min} \tag{34}$$

With $R_{sl\,min}$ the shear layer is limited in the minimum radius on the stationary shoulder side and with R_{sl} is the maximum radius of the shear layer at the rotating shoulder side. The v_{tan} is defined in Equation (35) as an interpolation between the maximum tangential velocity of the probe and zero.

$$v_{tan} = r\omega\,(1 - \zeta^{m_z}\,\rho^{m_r}) \tag{35}$$

The exponents m_z and m_r were added to control the transfer of the gradient of v_{tan} vertically and horizontally. The tangential velocity is limited for $(1 - \zeta^{m_z}\,\rho^{m_r}) \geq 0$ and $r \leq R_{sl}, \zeta \leq 1$.

Since the asymmetric macrostructure of the S^{3}BT process variants did not fit to the analytical velocity field of the existing ASLM, the implementation of an asymmetric analytic shear layer model (A^{2}SLM) became necessary. A simple approach is to influence the maximum radius R_{sl} of the shear layer on the rotating shoulder side. Thus, the angle β of the rotation of the z-axis is used as shown in Figure 30 and in Equation (36).

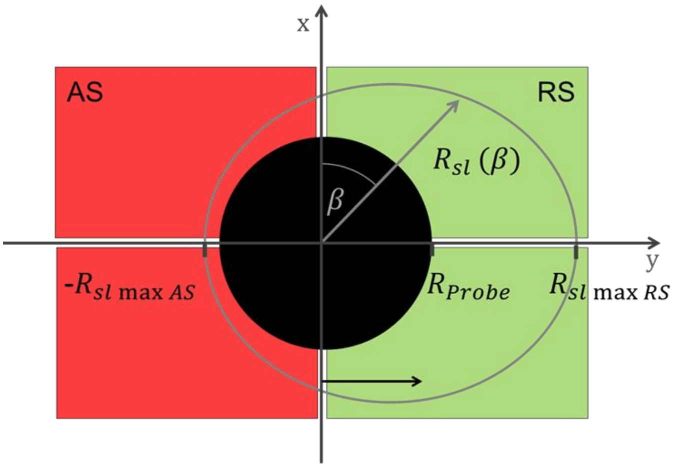

Figure 30. Definition of the radius of the asymmetric shear layer model.

$$\beta = \sin^{-1}\frac{y}{\sqrt{x^2+y^2}}\,, \qquad \beta \in \left\{-\frac{\pi}{2}, \frac{\pi}{2}\right\} \tag{36}$$

The results of the function are a mirrored angle on the y-axis. The angle β is negative in the red fields and positive in the green area of Figure 30. The variable maximum shear layer radius $R_{sl}(\beta)$ is defined by Equation (37).

$$R_{sl}(\beta) = R_{sl\,\max AS} + (R_{sl\,\max RS} - R_{sl\,\max AS})\left(\frac{\frac{\pi}{2}+\beta}{\pi}\right)^{m_{asym}} \tag{37}$$

To adapt the new shear layer shape, the variables $R_{sl\,max\,AS}$ and $R_{sl\,max\,RS}$ define the boundary on the AS and RS. The exponent m_{asym} defines the shape of the shear layer. An example for an A^{2}SLM is shown in Figure 31 (a) with a view in welding direction and in Figure 31 (b) as 3D view. As a result, Figure 32 shows an overlay of a fitted analytical shear layer model to the macrostructure of a weld. The function $R_{sl}(\beta)$ was implemented to the ASLM of the different process variants, but mostly used for the S^{3}BT process variants. The A^{2}SLM definition includes an inconsistency in the transported material volume in the shear layer region is indicated in Figure 31 (c). This behaviour reflects the flow during the consolidation of the welding process as explained in Section 5.5.5.

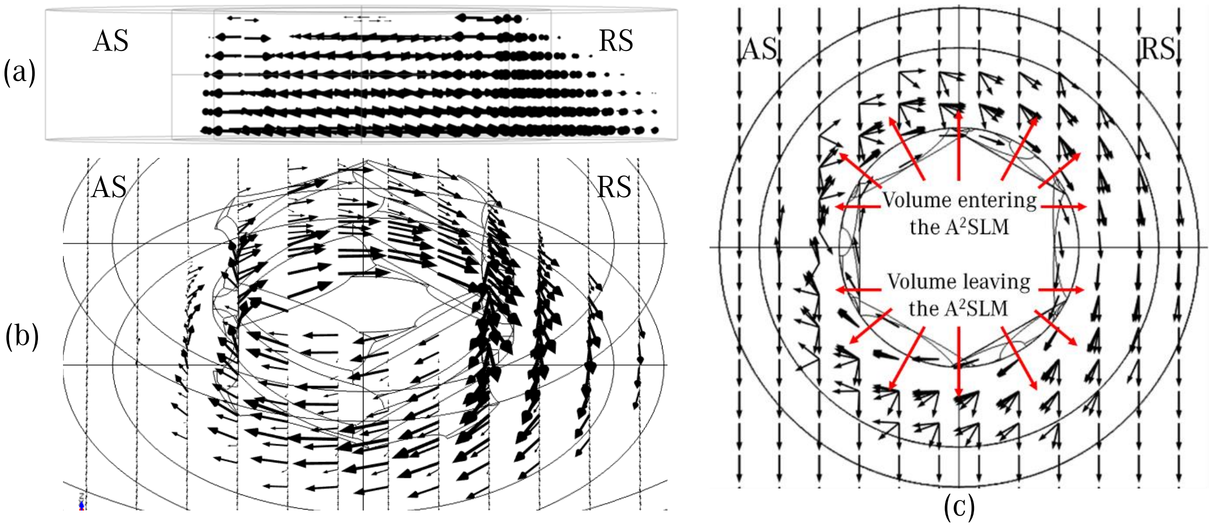

Figure 31. Examples of the asymmetric analytical shear layer model for the S^{3}BT-SUS process variant: (a) view in welding direction, (b) 3D view and (c) top view with the volume inconsistency between AS and RS pass.

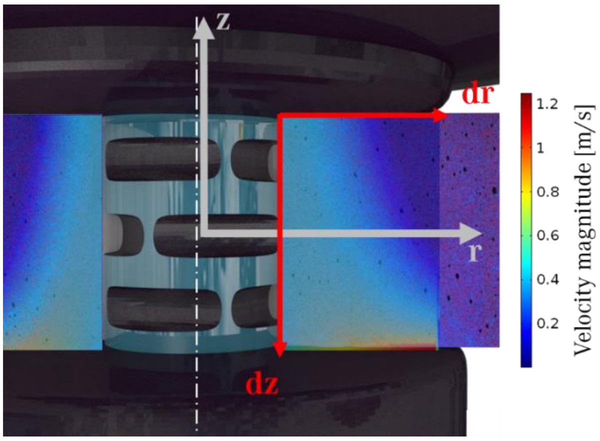

Figure 32. Analytical shear layer velocity overlayed with the macrostructure.

For the SSBT process variant including the straight probe design, the curves for the velocity are described analogue to the S^{3}BT process variants. Since the presumed velocity field is symmetric, dz origins in the horizontal middle line as an absolute value and the curves are mirrored vertically. The resulting velocity field is shown in Figure 33 (a) and the subset area for the mathematic description for the A^{2}SLM of the SSBT process variant in the straight probe configuration in Figure 33 (b) and in Equations (38) to (43).

$$dr = r - R_{Probe} \tag{38}$$

$$dz = |z| \tag{39}$$

$$\rho = \frac{dr}{R_* - R_{Probe}} \tag{40}$$

$$\zeta = \frac{2dz}{T_P} \tag{41}$$

$$R_*(\zeta) = (\zeta^{m_{shape}})\, R_{sl\,min} + (1 - \zeta^{m_{shape}})\, R_{sl\,asym} \tag{42}$$

$$v_{tan} = R_{sl}\,(1 - \rho^{m_r}) \tag{43}$$

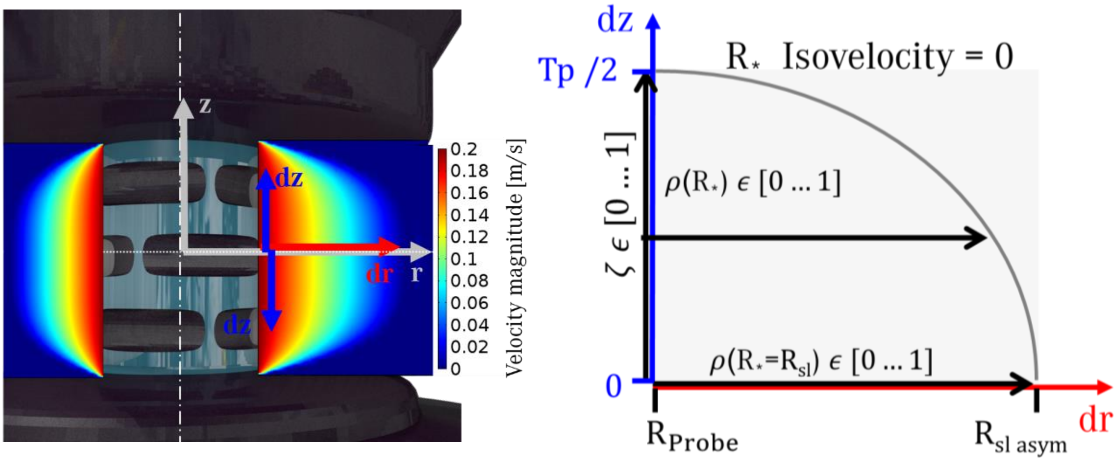

(a) (b)

Figure 33. A²SLM of SSBT process variant, shown as (a) an example of velocity field and coordinate systems, and (b) the restricted subset area for definitons of shear layer velocities.

The tangential velocity is here also limited for $(1 - \rho^{m_r}) \geq 0$ and for $r \leq R_{sl}(\beta), \zeta \leq 1$. The velocity fields of the A²SLM are applied during the thermal simulation. An example of resulting temperature field is given for weld 11 of Table 4 and Table 5 with the SSBT process variant including the straight probe in Figure 34. For the velocity fields of the CFD simulation these temperature fields are used as an input.

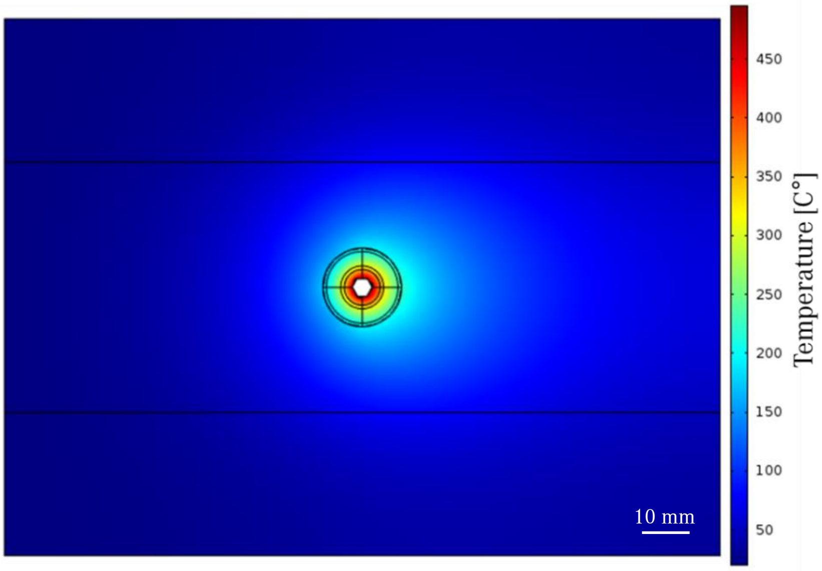

Figure 34. Temperature field for CFD simulation from SSBT with the straight probe design.

5.3.2 Boundary Conditions

The achieved welding and rotational speeds for BT-FSW in the present work are much higher than the ones described by Hilgert [1] or other references in the literature mentioned in Section 3. Several aspects contribute to a higher gradient of shear rate in the SZ. A higher welding speed leads to a reduction in width of the SZ and a faster rate of incoming material. A higher rotational speed leads to an increase in the maximum velocity in which material is transported around the probe. The combination of these conditions results in an increase of the maximum values of velocities in a decreased area of interest. The shear rate is the difference in between the velocities. The implemented viscosity models are depending on the shear rate and temperature. Besides that, they are strongly nonlinear, what can lead to difficulties in convergence during the calculation of the velocity field with the corresponding material viscosity in the SZ. Being aware of these factors, a CFD model was designed for the evaluation of the different process variants.

Considering the fine resolution in mesh demanded by the high gradients of the material viscosity, the number of elements per volume had to be increased. The time dependent model described by Hilgert [1] uses a rotating domain in connection with a domain representing the rest of the welded material. A high number of elements was used to create identity pairs in between the rotating domain and the fixed domain of the work piece. The pairs were necessary to implement the continuity conditions in the geometry. After Hilgert's model [1], a new "rotating machinery" interface was introduced by COMSOL Multiphysics. The model was based on the stationary "frozen rotor" study implemented in the COMSOL Multiphysics software interface of rotating machinery. Within this study, an Eulerian formulation is fully coupled, solved through an iterative solver approach. With this stationary solver, the results were improved and comparable to the time dependent solution according to the velocity field in the SZ.

Through these considerations, the CFD model applied in the present study consists solely of a rotating domain as presented in meshed conditions in Figure 35 (a). To define the applied boundary conditions, the geometry was chosen slightly bigger than the weld zone in between the tool's shoulders. The domain was divided in specific sections of outer boundaries. With this procedure, all inner boundaries were obsolete, except the ones necessary for evaluation of probes[5]. Virtual operations were applied where possible, in order to save calculation time and reduce the number of elements in non-valuable regions. With the small rotational domain, the mesh could be chosen with a high resolution in the areas of interest. Also the implemented limits of viscosity for the model could be defined wider, with a minimum of 10^2 $[Pa\ s]$ and a maximum of 10^{12} $[Pa\ s]$. The first boundary

---

[5] Referes to probes for physical parameter evaluation implemented in the boundaries or domains of the model –not the component of the tool "probe"

is comparable to olive oil and the second to asphalt. In comparison to the velocity profile in the macro sections presented by Hilgert [1], the results have a higher resolution.

The dominating boundary conditions were implemented on the modelled geometry as shown in the example for the S^3BT-SUS process variant: in Figure 35 (a). The domain was meshed with a total amount of approximately $5\ 10^5$ tetrahedral elements. The mesh was optimized according to the expected gradients of velocity profile. One of the highest gradients expected takes place between the highest orbital speed of the rotating shoulder and the surface of the material. This occurs at the outer radius of the rotating shoulder, which is in contact with the material located next to the unaffected material's surface. Consequently, the mesh is more refined at the surface around the line in between the rotating boundary of the upper shoulder of Figure 35 (b) and the slip condition of Figure 35 (c). In Figure 35 (d) and (e), the in- and outlets are defined. The inlet is defined according to the experimental welding speed. The boundary condition outlet is free of pressure. In Figure 35 (f), the stationary upper shoulder is represented by boundary condition with welding speed.

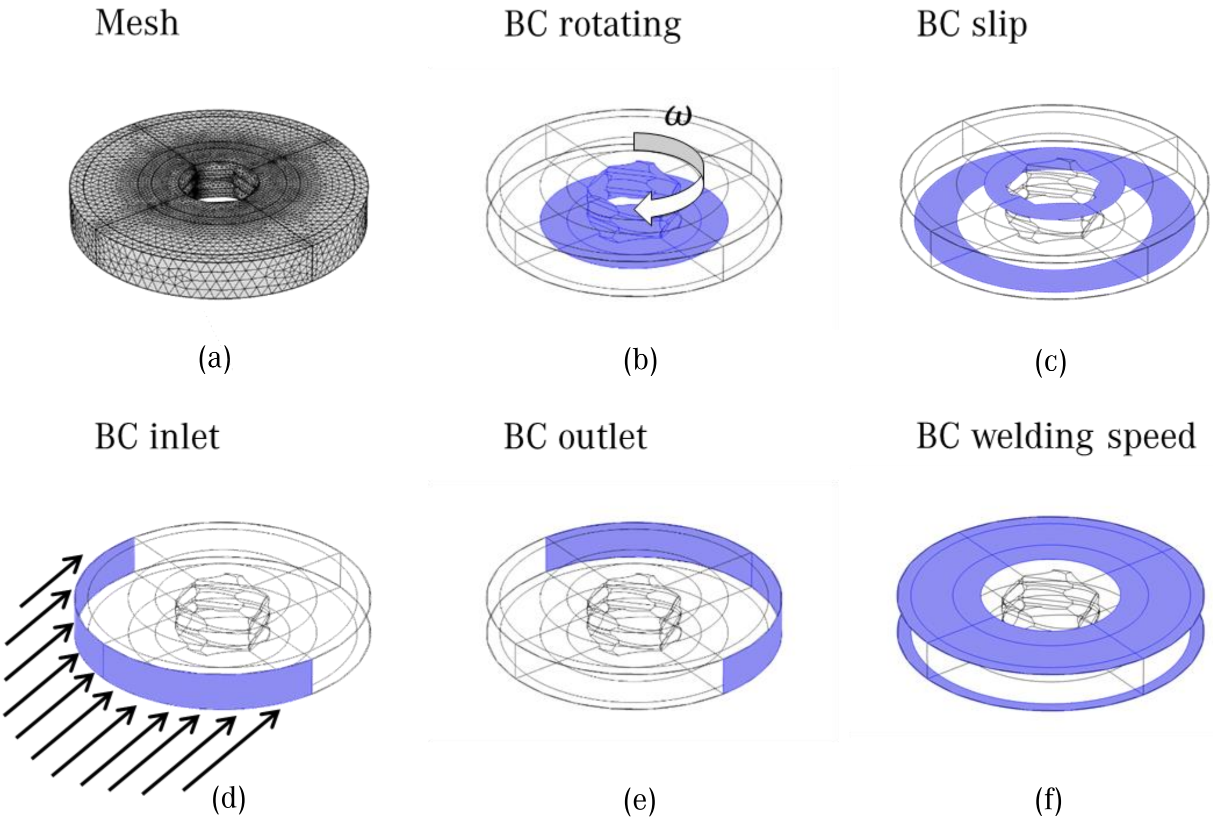

(a) (b) (c) (d) (e) (f)

Figure 35. Model for S^3BT-SUS and boundary conditions (BC).

For the temperature simulation, BCs for the A^2SLM were applied on the original CFD domain in Figure 35 (a) and the BCs for the thermal-pseudo-mechanical heat source were applied on the boundaries of the rotating tool parts as in Figure 35 (b). Also the thermal-pseudo-mechanical heat source for the sliding was applied on the boundaries of the stationary shoulder. For the convective heat transfer to the lower shoulder and to the spindle, boundaries conditions were applied on the fluid domain. While the fluid mechanisms are only active in a limited region of the weld zone, the heat transfer affects a wider volume of the welding configuration.

In order to satisfy this requirement, the domain for CFD was extended for the thermal simulation to the dimensions of 150 mm x 200 mm as seen in Figure 36 (a). The convective heat transfer to air and to the clamping system is shown in Figure 36 (b) and (c), respectively. Analog to the CFD domain boundaries, the inlet and outlet were defined in Figure 36 (d) and (e). Identity pairs were implemented to couple the domains as presented in Figure 36 (f). The resulting temperature fields were mapped onto the smaller fluid domain and used during the CFD simulation as an input for the effective viscosity.

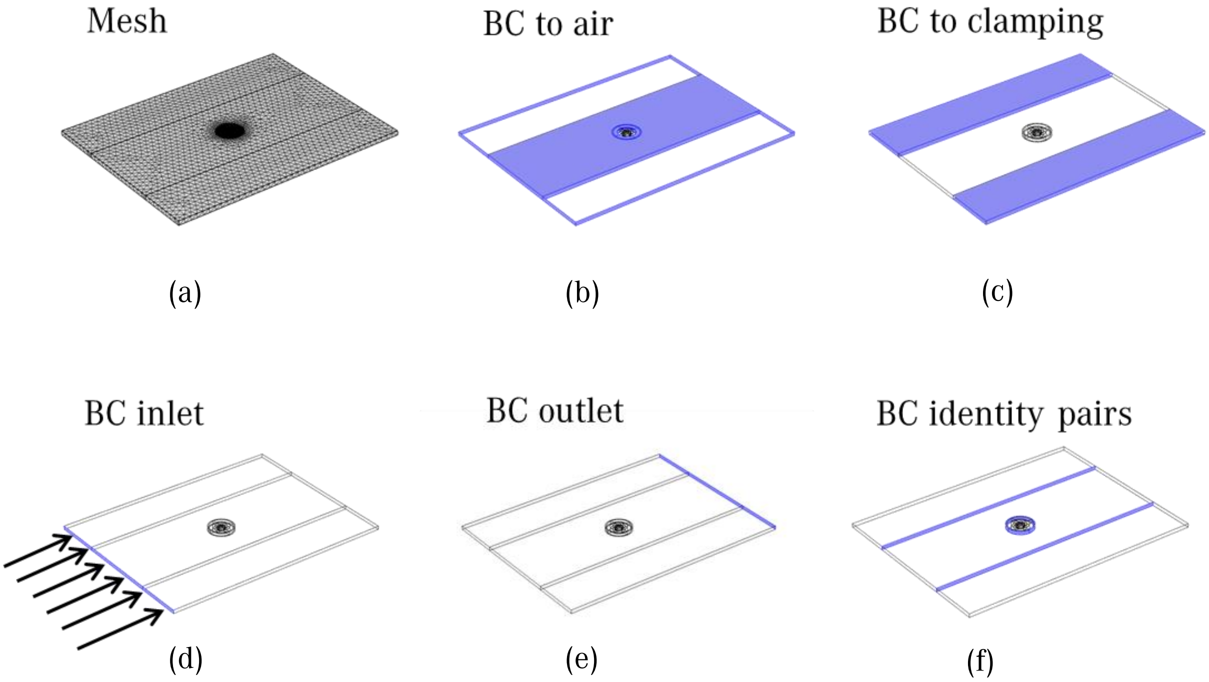

Figure 36. Boundary conditions for the conventional SRBT CFD model.

5.3.3 Predictions and Validation of CFD

The simulation model was fed with the parameters of the welding experiments (Table 5). As a first step, the temperature fields were calculated. Second, the fields were mapped onto the CFD domain and the CFD simulation was conducted.

5.3.3.1 Temperature Fields

To validate the implemented temperature fields and also validate the reduction of the thermal cycle during the welding process in the S^{3}BT process variants, temperature measurements with an infrared camera have been conducted. Observed were the welding processes of conventional SRBT (120 mm/min and 300 mm/min), S^{3}BT-SLS (1800 mm/min) and S^{3}BT-SUS (2000 mm/min and 3000 mm/min). These are the welds 1, 2, 5, 7, and 9 of Table 5. The images of the temperature fields are shown in Figure 37 (a) to (e). The images were taken at the end of the welding process, shortly before the tool exits the work pieces. Especially in Figure 37 (b), (d) and (e) the reflection of the unpainted surface of the work pieces in front of the tool can be observed. The influence of the process and the welding speed can be seen through the comparison of the size of the conventional SRBT process variant with 120 mm/min and 300 mm/min in Figure 37 (a) and (b), respectively. With the S^{3}BT process variants the temperature field is reduced when compared to the conventional SRBT process variant.

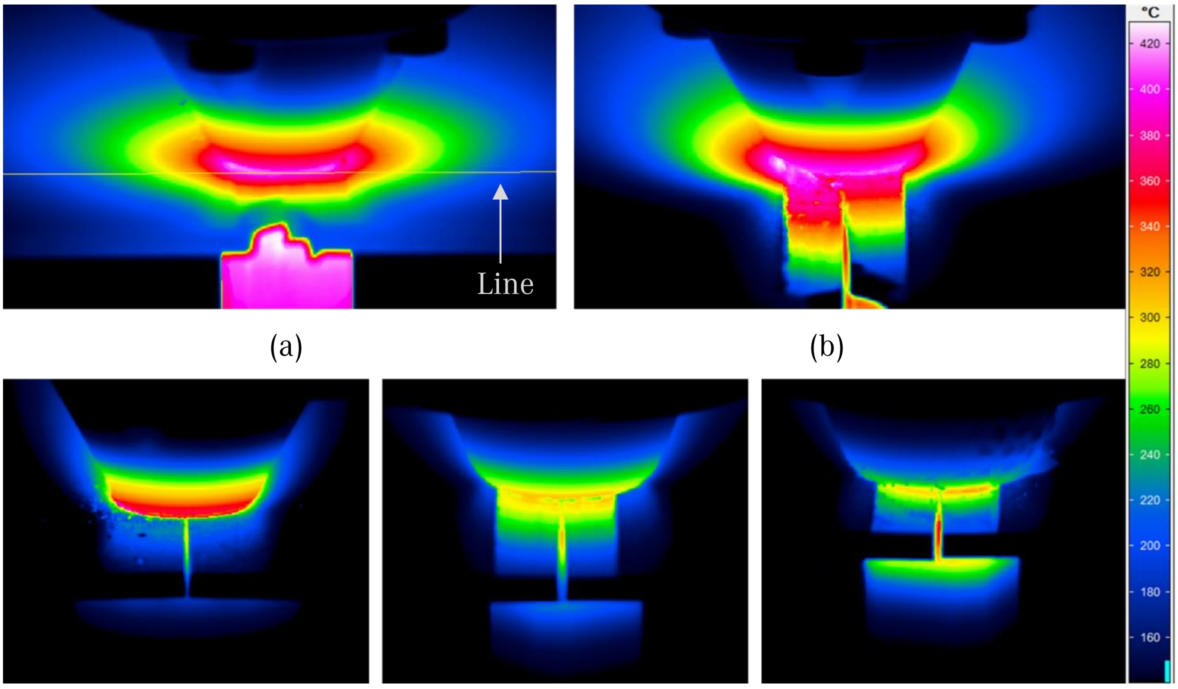

(a) (b)

(c) (d) (e)

Figure 37. Thermographic images of different processes with different welding speeds in [mm/min]: (a) conventional SRBT 120, (b) conventional SRBT 300, (c) S^{3}BT-SLS 1800, (d) S^{3}BT-SUS 2000 and (e) S^{3}BT-SUS 3000.

Regarding the temperature of the upper shoulder the temperature reduces from the rotating shoulder in the S^{3}BT-SLS process variant (Figure 37 (c)) to the stationary shoulder of the S^{3}BT-SUS process variant (Figure 37 (d)). In between the S^{3}BT-SUS process variants with different welding speeds, the gradient of the temperature changes when Figure 37 (d) and (e) are compared.

To compare the width of the temperature fields, the temperature was evaluated along a line as indicated in Figure 37 (a). The results of the evaluation for the lines of Figure 37 (a) to (e) are presented in the graph of Figure 38 (a). The resulting peak temperatures and the width show a correlation with the welding speed. There is a strong correlation between the line-energy and the welding speed as seen in the function of line-energy calculation in Equation (1). The higher the welding speed, the narrower the temperature field and the smaller the measured peak temperature. The validity of the comparison between the S^{3}BT-SLS and S^{3}BT-SUS is limited because of the perspective on the upper side of the work pieces of the camera. The stationary upper shoulder is not as active in the heat generation as a rotating shoulder. Nevertheless, the graph correlates with the evaluation of the line-energy for the different process variants in Table 5. In Figure 38 (b) the graphs of the temperature field of the simulations are presented.

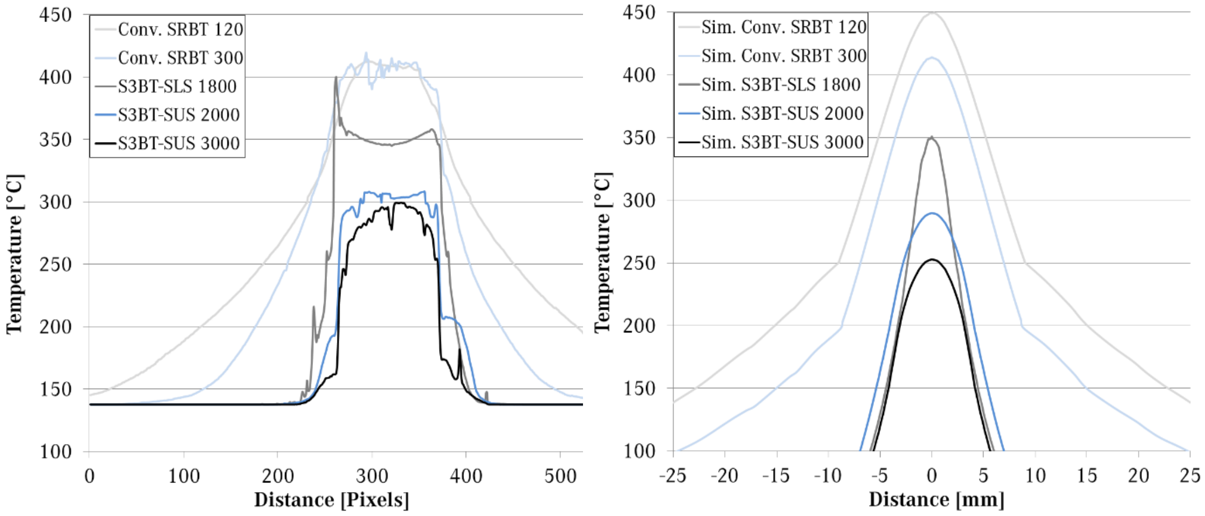

Figure 38. Resulting graphs from (a) temperature measurements and (b) simulations.

In general there is a good agreement between the recorded and the calculated fields. The peaks of temperature are narrower in the simulation than in the infra-red camera measurements. This can be explained by the perspective of the infra-red camera. The temperatures are evaluated from the data saved for each pixel of the image. With this method the evaluation is influenced by the angle of the camera. The calculated values in the simulation can be compared with an angle of zero degree of top view. The line of evaluation, in this case, is tangential to the shoulder radius. As a consequence the temperature curves have a pronounced sharp maximum in the simulation. The peak values of the simulation show that for two active shoulder surfaces the predicted temperatures are appearing too high. With only one rotating upper shoulder the prediction of the peak temperature is very close to the measured temperature field, leaving the peak of the plasticized toe flash on the left side of the image aside. Shifting the main heat source to the lower shoulder and using only the frictional heat generated by sliding on the upper shoulder the predicted peak temperatures are lower than the ones measured during the welding processes.

The reduced heat input of the new process variants shows as well in the experiments as in the simulation, which was one of the objectives of the present study. The measured values of the line-energy presented numbers in Table 5 also correlate with the measured and simulated temperature fields and the hardness measurement in Appendix B.

5.3.3.2 Velocity Fields

All CFD simulations were conducted with both viscosity models. For the evaluation, a surface which is crossed by all flows in perpendicular direction was chosen. In Figure 39, this plane is represented by the vertical line through the velocity field and the material transport can also be seen. It can be observed that the material incoming on the AS is transported to the RS and propelled behind the probe. Also, there is a flow against the welding direction on the AS.

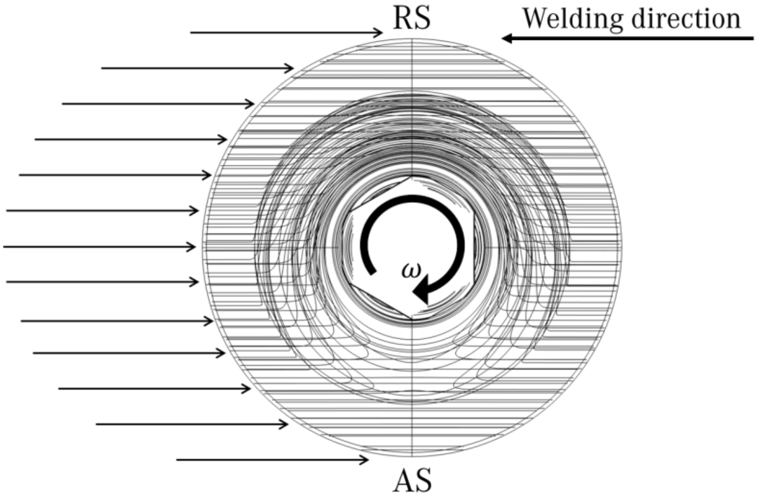

Figure 39. CFD flow pattern for the S^3BT process variant in the weld zone as top view.

The velocity field predictions are in good agreement with the weld zone macrograph, as shown in Figure 40. The area of high velocity directly underneath the rotating lower shoulder on the RS shows a comparable TMAZ and SZ. On the AS, the model predicts an increased area of the velocity field in comparison to the macrograph. In the experiments, the influence of the rotating shoulder on the AS

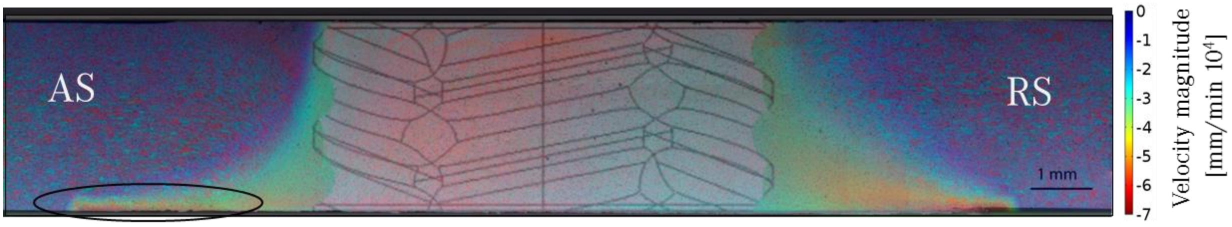

Figure 40. CFD simulated velocity field superimposed on a macrograph of a S^3BT-SUS weld with marked area of increased velocity profile on the AS.

for all S^{3}BT welds was small, when compared to conventional SRBT in Table 5. This phenomenon is further discussed in Section 5.5.4.

The boundary conditions of the S^{3}BT-SUS and -SLS process variants in CFD simulation are identical. Since all achieved welds with the S^{3}BT-SLS variant included material loss through flash and a tilt of the upper shoulder, the CFD description fitted better the volume of the S^{3}BT-SUS process variant. In Figure 41, the magnitude of the velocity field around the probe for the S^{3}BT-SUS process with a welding speed of 2950 mm/min is displayed. At a closer look in Figure 41 (a), the viscosity calculated with ln displays greater gradients in the vicinity of the moving parts of the tool. These gradients fit the observed macrostructure of the SZ better, as compared in Figure 40. For the remaining part of this work, only the viscosity based on the calculation with ln is considered.

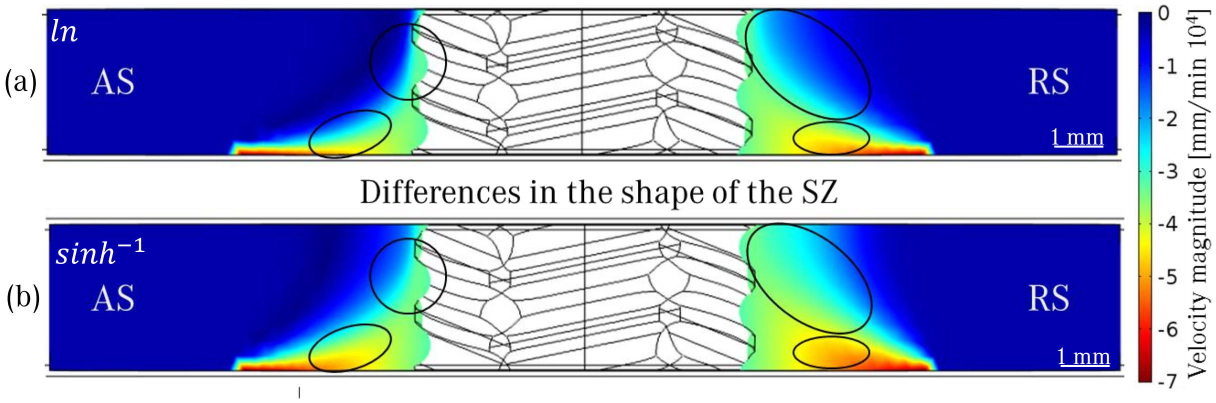

Figure 41. Comparison between the effective viscosity models for S^{3}BT simulation with a welding speed of 2950 mm/min based on (a) the natural logarithm (ln) and (b) the inverse hyperbolic sin law ($sinh^{-1}$). Circled areas indicate the highest differences.

An overview of the conducted CFD simulations is presented in Table 6. The displayed “u” component of the velocity is in the welding direction and opposite to the incoming material flow, as indicated previously in Figure 39. The simulation shows that the material on the AS is transported around the probe in the welding direction. Therefore, the “u” component velocity is positive on the AS (blue velocity field). The observed predictions of the opposing flow on the AS were described in the literature in CFD computation [50, 85, 92, 93, 95, 100], as well as in marker material and stop action technique experiments [68-72, 74]. On the RS, the transported material around the probe is in the same direction as the incoming material, resulting in a negative “u” component.

Table 6. Overview of the velocity field from the conducted CFD simulations

Simulation Nº	**Process**	**Material thickness [mm]**	**Welding Speed [mm/min]**	**Probe Design [mm]**	**Macrograph**	**Scale**
					AS RS	
1	**Conventional SRBT**	3	120	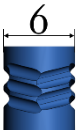	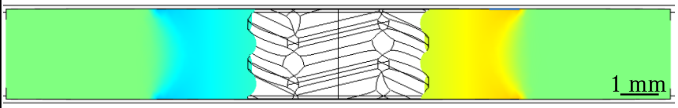	
2		3	300	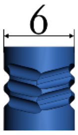	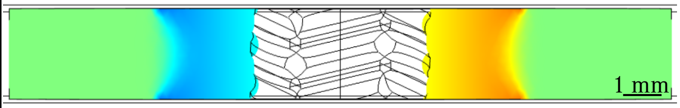	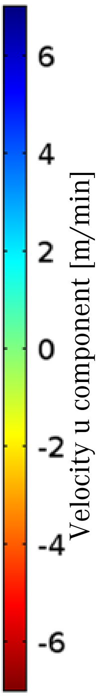
3		3	300	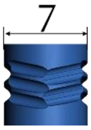	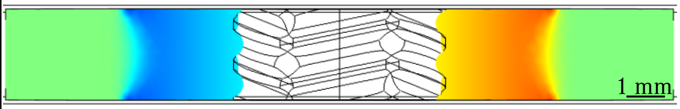	
6	**S³BT-SUS**	3	1850		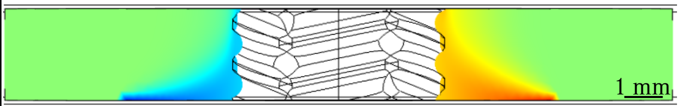	
7		3	2000	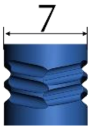	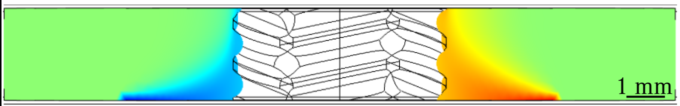	
8		3	2500	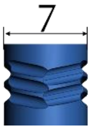	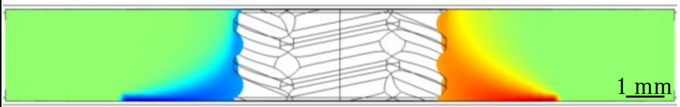	
9		3	2950		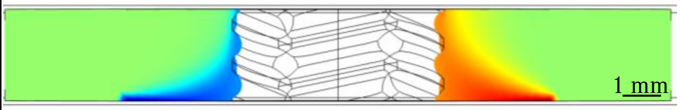	
10	**SSBT-stepped**	3.6	100	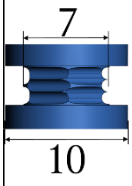	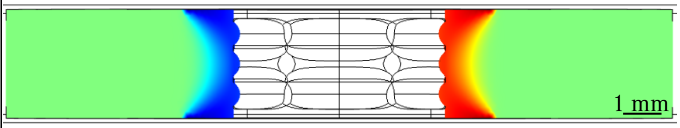	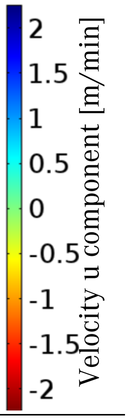
11	**SSBT-straight**	3.6	100	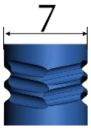	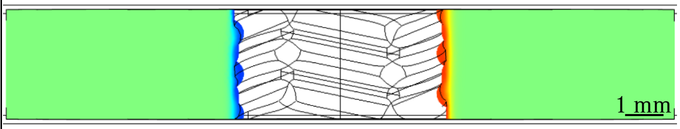	
					AS RS	

The comparison between the simulations of Table 6 and the macrographs of Table 5 indicates that the CFD model described well the material flow. The velocity fields of the conventional SRBT process variant with probe diameter of 6 and 7 mm can be compared in the simulations 2 and 3 of Table 6. A visible difference in the expansion of the velocity fields in these two welds was calculated by the simulation. Especially the increase of the velocity field with the 7 mm probe diameter appears to be remarkable. The scaling of the tool components was done with an increase of the profile of the probe by 17%. With this the area of the velocity field was calculated to be increased by 18%, which shows that the increase of the area is not uncommonly high.

The most evident differences between the conventional SRBT and the S^3BT process variants are the shape and the area of the SZ. The comparison of the velocity fields of the S^3BT-SUS process variant for the simulations 3 to 6 presented in Table 6 shows that the welding speed had an influence on these results. Mainly the velocity gradient and the maximum achieved velocity changed. However, the geometrical outline of the velocity fields appears constant for different welding speeds. This can be seen comparing the yellow region in the positive velocity field on the RS and the light blue region in the negative velocity field on the AS.

The simulations 7 and 8 of Table 6 present the results for SSBT process variant with the stepped and straight probe design, respectively. The simulation can be compared to the supported stationary lower shoulder since a since a displacement of the boundaries was not possible. The shear layer of material for the straight probe with no shoulder rotation is narrower, when compared to all other simulations. The area of the SZ has a diameter very close to the probe diameter. Within the simulated weld zone, the material was accelerated to the rotational speed of the probe and transported around it, without greater influence of the material in greater vicinity of the probe. With this phenomenon, the maximum shear rate close to the probe was calculated to be more than 400 times higher than in the configuration with the stepped probe design. In the experiments the material transport at very high shear rates due to friction ceases and sliding dominates the interaction between the contact channels. Thus, the simulated shear rate gradients lead to sliding conditions in the experiments.

The calculation based on the $sinh^{-1}$ for the viscosity model found convergence in a comparable amount of the iterations in comparison to the viscosity equation based on the ln. As an important influence of the convergence behaviour the limits of the viscosity were identified. At a maximum viscosity of 10^{12} $[Pa\ s]$ more than twice of the calculation time was necessary in comparison of the maximum of 10^{9} $[Pa\ s]$. Convergence above a maximum of 10^{12} $[Pa\ s]$ could not reached for some process variants.

In general, the CFD model showed good agreement with the results of the experiments. For more precise results, material parameters such as $UTS(T)$, n, A, and Q_a for higher strain rates have to be experimentally acquired and implemented as strain rate dependent variables into the model. For the present study, the material parameters of AA6082 aluminium alloy were available with defined strain rates. In case of n, A, and Q_a the parameters were available for different temper condition and different strain rates in the work of Zhang et al. [114]. In comparison to the observed literature, this volume of available data represents a great advantage.

In the CFD simulation, any welding process variant is stable and running – regardless of reaction forces or elevated temperatures above melting point. Therefore, a challenge in the present work was to find interpretable results from modelling which indicate whether the process is feasible in experiments. In order to find an explanation for the tilted shoulder observed previously in the experiments (Section 5.2.1), the pressure on the surfaces of the shoulders was evaluated for the S^3BT and SSBT process variants. In the model, no exceptional elevated pressure on the RS could be found, as shown in Figure 42. In consequence, this phenomenon is further investigated as presented in Section 5.5.

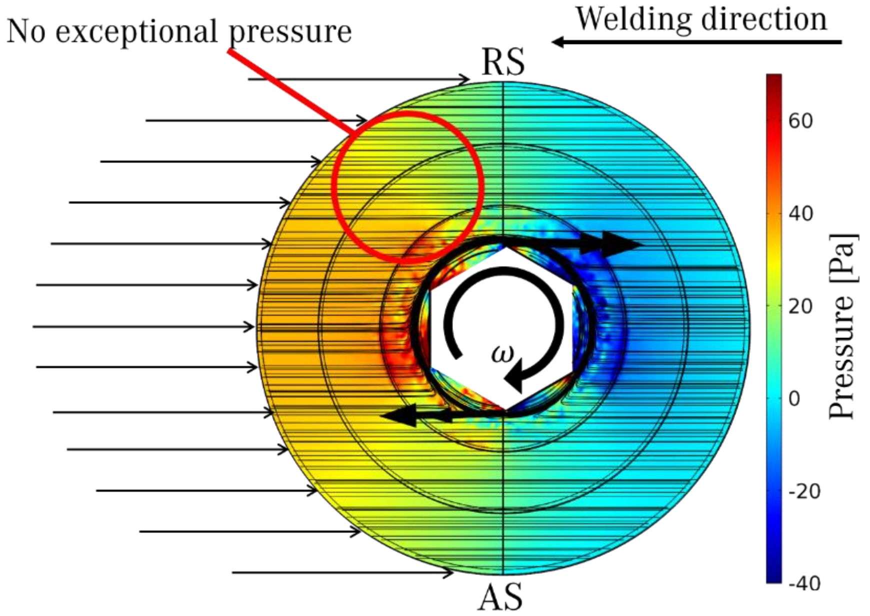

Figure 42. Pressure field from CFD simulation of SSBT process variant with the straight probe design.

The material underneath the rotating shoulder on the AS is not affected by heat as much as the simulation suggests. The material transport on the AS is dominated by a process comparable to milling as suggested in Section 5.4. Since sliding condition of the rotating shoulder is not implemented in the viscosity model, the material is “sticking” to the boundary of the rotating shoulder and causing material transport in the simulation.

5.4 Influence of Rotating Shoulder

In Table 5, the macrographs of the different process variants are displayed. It can be observed in the macrostructures that the rotating shoulder of S^3BT process variants had little influence on the material at the AS in the vicinity of the shoulder, and this observation is new to the FSW processes. Even with the rotating shoulder used in the present study, the appearance of the AS is similar to the stationary shoulder welds of the single-sided FSW process variant [21, 23, 25, 28].

In Figure 43 the areas close to the rotating shoulder in the AS and the RS are closer observed. A macrograph of weld 5 obtained with the S^3BT-SLS process variant, as earlier presented in Table 5, is shown in Figure 43 (a). The shape of the SZ is indicated with red lines. On the upper surface of the RS, the material seems to be milled away with little effect on the material underneath the removed volume. As seen, the imprint of the upper shoulder on the AS in Figure 43 (b) is approximately 2 mm away to the left from the SZ. In Figure 43 (c), the influence of the rotating shoulder on the material in the RS ends at the outer radius of the shoulder.

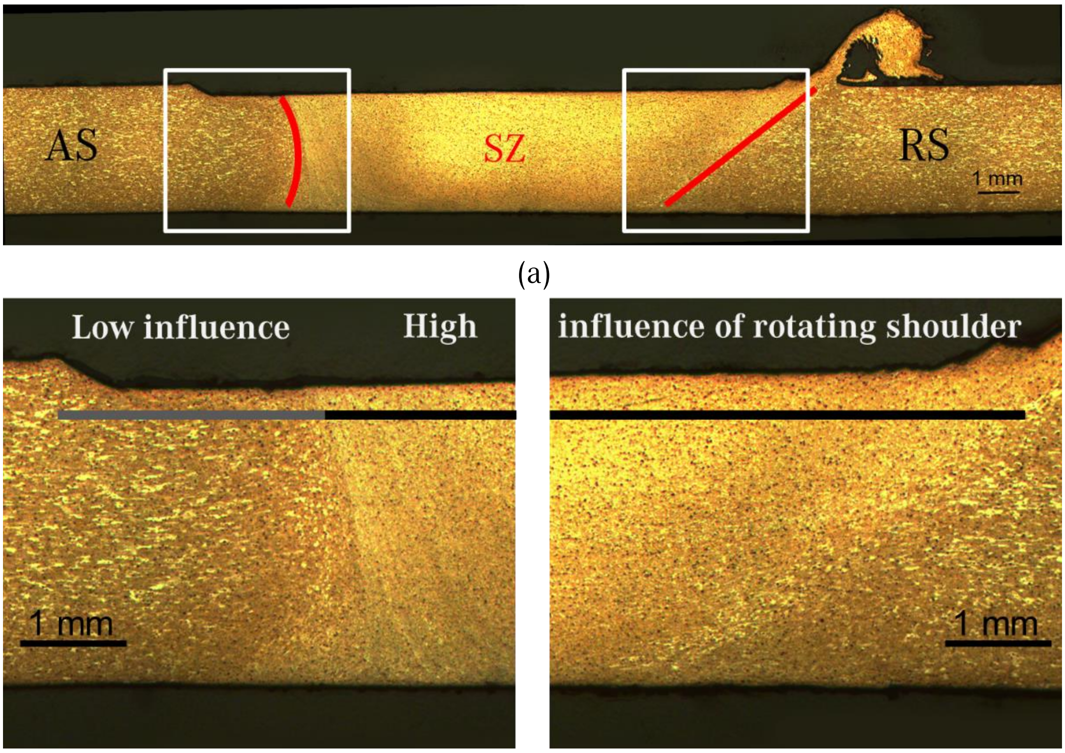

(a)

(b) (c)

Figure 43. Influence of the rotating shoulder of S^3BT-SLS process variant on the material: macrograph of the cross section of the weld in (a) complete view, (b) detailed AS, and (c) detailed RS.

A similar behaviour regarding the rotating shoulder has been observed for the S^3BT-SUS process variant displayed for welds 6 to 9 in Table 5. The macrograph in Figure 44 (a) was obtained through etching with Barker´s reagent of the weld 9, performed with a welding speed of 2950 mm/min. In the Figure 44 (b), the microstructure is detailed on the AS at the contact region of the rotating lower shoulder. The influence of this rotating shoulder ends in less than a 1/10 of a millimetre away from the surface on the outer radius of the shoulder contact.

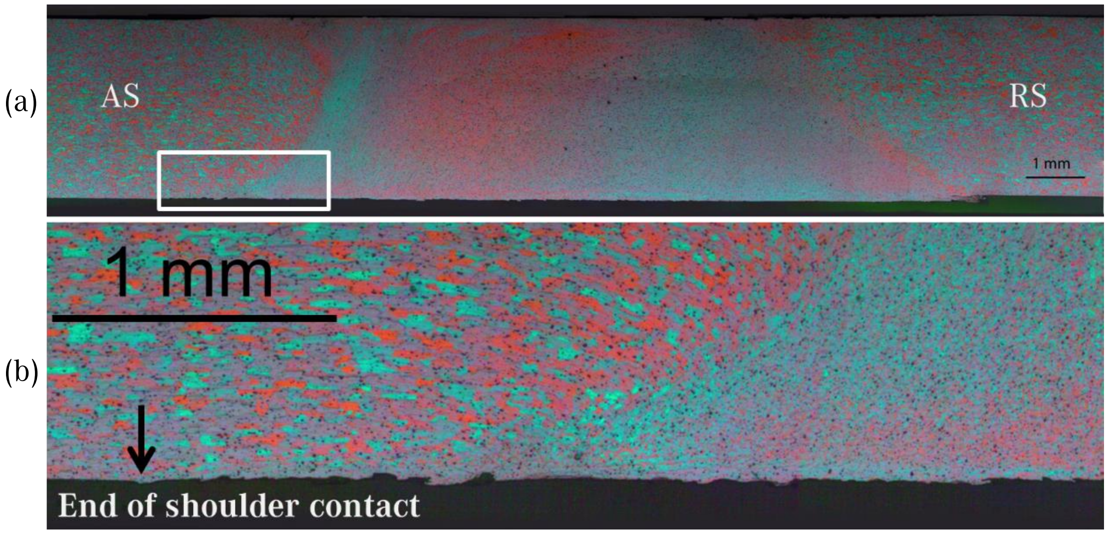

Figure 44. Macrograph of the weld 9 conducted with S^{3}BT-SUS process variant: (a) overview and (b) detailed contact region of rotating shoulder.

The stop action technique is a common practice in literature to have a better understanding of the material flow around the probe. In the present study, the advantages of the stop action technique, described in Section 4.5.1, were successfully applied. In Figure 45, the macrostructure in the vicinity of the rotating shoulder is presented. The rotating shoulder had a different influence on the material of the RS and of the AS, as described previously in this section. When it is compared to the indicated black circle in Figure 45, the radius of transported material is smaller on the AS and becomes as big as the shoulder radius on the RS.

The material flow at mid-thickness of the weld is presented in Figure 46. The influence of the rotating shoulder was reduced to the material flow around the probe. The material flow radius on the RS and on the AS were reduced as well.

The diameter 1 indicated in Figure 46 correlates to the radius received from the cross sections of the simulations in Table 6. The diameter 2 correlates to the cross sections presented in the macrographs of Table 5. The cross section of the SZ through the trailing side of the probe (diameter 2) is increased in comparison to the cross section of the SZ directly in the vicinity of the probe (diameter 1) by around 10%. It shows that the formation of the weld zone seen in the macrographs takes place on the trailing side of the probe. This formation was also observed but not discussed by Zettler [69, 70]. The active mechanisms on the trailing side of the probe are further discussed in Section 5.5.5.

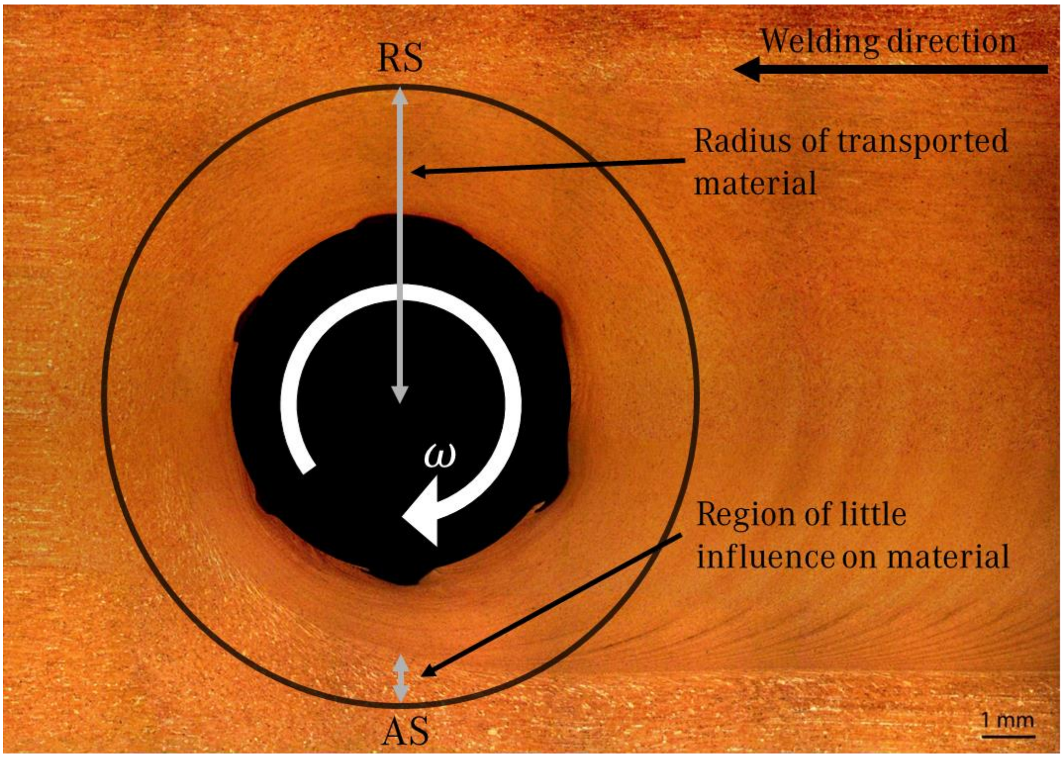

Figure 45. Macrograph of the weld zone directly underneath the rotating shoulder through stop action technique and the influence of the shoulder on the material.

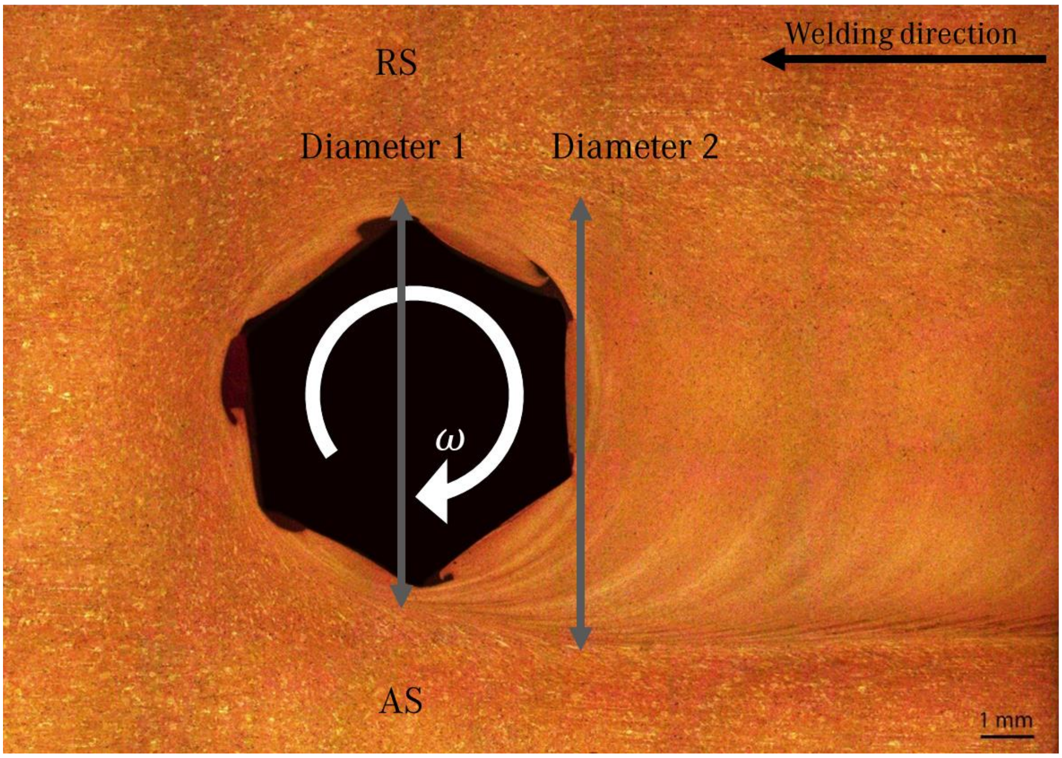

Figure 46. Macrograph of the flow through stop action technique in the mid-thickness of the weld and the diameters in the SZ.

5.5 Analytical Model for Weld Zone Conditions: Explanation of Observed Phenomena

The results from experiments and the simulation show no evident reason for the observed phenomena, especially in the case of material loss due to accumulation on the RS (Section 5.2.1). The experiments resulted in difficulties in feasibility of the SSBT process variant, such as:

- tilted shoulder which is apparently caused by high pressure on the RS;
- initiation of flow around the probe, which can result in accumulation of material on the RS.

In the observation of the experiments, there was a tilt angle of the stationary lower shoulder in SSBT and S^3BT-SLS process variants. The accumulated material on the RS and the tilt angle were shown, respectively, in Figure 25 and in Figure 26 (a) (Section 5.2.1). These phenomena could be an indication of increased pressure on the RS. However, the pressure plot of the simulation in Figure 42 (Section 5.3.3) illustrates that no exceptional pressure has been found on the RS. Also it was shown in the CFD simulation that most of the material passes only through the RS. This is in agreement with the literature, as exposed earlier (Section 5.3.3). In the macrograph of the stop action technique in Figure 45 (Section 5.5.4), an asymmetry of the SZ can be observed. The SZ is shown with different radii of influenced material on RS and AS. In the macrograph of Figure 42 and analogue in the simulation in Figure 39 a constantly rotating backflow in the region of the AS is observed. This was also described in several studies [50, 68-72, 74, 85, 92, 93, 95, 100]. The analytical model presented in this section was built to explain these phenomena.

5.5.1 Discretized Mass Flows: Top View

In order to understand these phenomena, the flow in the SZ has been divided into discrete parts. In Figure 47, the different mass flows can be observed separately in a top view macrograph. The mass flow $\dot{m}_1$ represents the mass of incoming material (inlet). The mass flow $\dot{m}_2$ represents the material on the AS which is entering the foreside of the probe after being transported all the way around the probe. Along the rotation, the $\dot{m}_1$ and $\dot{m}_2$ mass flows are combined in front of the probe to the mass flow $\dot{m}_3$ passing through RS, assuming incompressibility and mass continuity. The mass flow $\dot{m}_4$ represents the material passing through the AS as a rigid solid[6] state material. It is suggested that the interaction between this mass flow $\dot{m}_4$ and the pressure condition behind the probe are

---

[6] Since it is a solid state joining process, the definition “solid” is found to be insufficient for the solid state of the material which is not part of the SZ

responsible for the reduction of $\dot{m}_3$ to $\dot{m}_2$ on the trailing side of the probe, as described in Section 5.5.5.

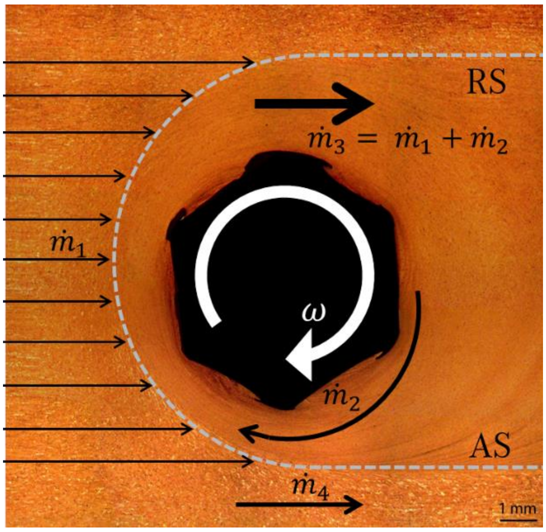

Figure 47. Scheme of the material flow in the SZ divided into discretized flows.

5.5.2 Mass Flow $\dot{m}_2$

In FSW processes, the existence of the mass flow $\dot{m}_2$ was observed in stable welding conditions in the present study and in the literature. To demonstrate the importance of the mass flow $\dot{m}_2$ for stable welding conditions, a case of ceased mass flow is evaluated. This case describes insufficient material transport around the probe ($\dot{m}_2 = 0$) and results in high pressure in the SZ. The area A_{II} of the channel on the RS is comparably small to the area A_I of the incoming mass flow $\dot{m}_1$, as it can be observed from the diameters indicated with grey lines in Figure 48 (a). Assuming volume consistency, the flow velocity must be higher in the area A_{II}. The observed pressure conditions might remind of the application of the Bernoulli equation. A schematic display comparing two conditions consistent with the Bernoulli equation is given in Figure 48 (b). Considering the mentioned velocity condition $u_I < u_{II}$, the Bernoulli equation states that the pressure p_I in condition I must be high and therefore the pressure reduces in a transition zone to a smaller value p_{II} in the condition II.

The Bernoulli equation establishes a comparison between the conditions. The transition zone between conditions I and II during the welding process and especially any changes of energy are not implied. The transition zone is difficult to capture due to its complexity. In the present modelling, with the generally applied fluid domain, the flow of the material is initiated on the inlet boundary of the CFD model, as earlier described (Section 5.3.2). In the experiments, the plasticized material is entering “through” the boundary of the rigid solid material marked by dotted grey line in Figure 48 (a).

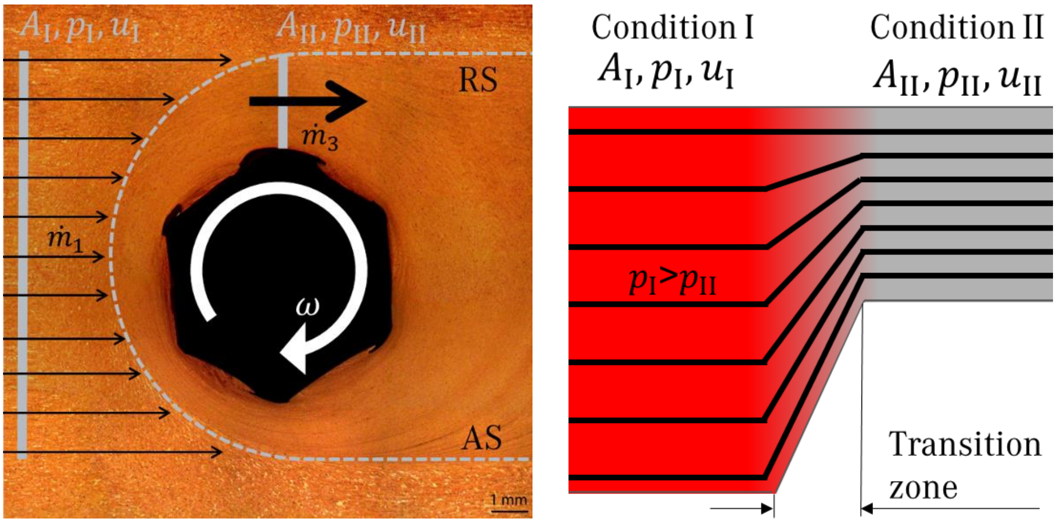

(a) (b)

Figure 48. Similarity between the (a) discretized material flows in the weld zone and (b) Bernoulli principle.

Moreover, the energy is changing in the transition zone, for example, by the plastification of the aluminium or the thermal input through viscous heating. One way to evaluate the energy input into the weld zone is the resulting mechanical energy input of the rotation of the tool components. Even though the Bernoulli equation does not reflect these changes of energy in the system, it can help to achieve an understanding of the interactions in the transition zone and the influence of the discretized mass flows. The derivation of the Bernoulli equation from the Euler equation, as done by Malcheret [143], can capture the applicability of the equation and help to comprehend the differences of the conditions in the FSW processes. In the Euler equation, the viscosity and the viscous heating are neglected. The balance of all involved impulses is given in the Euler equation (44).

$$\frac{\partial \vec{u}}{\partial t} + (\vec{u}\vec{\nabla})\vec{u} = -\frac{1}{\rho}\vec{\nabla}p - \vec{g} \tag{44}$$

Herein the terms are the time t, the density ρ, the velocity vector u, pressure p, and the gravity g. With a Weber transformation, the second term on the left side can be formulated as in Equation (45):

$$(\vec{u}\vec{\nabla})\vec{u} = \frac{1}{2} grad\, \vec{u}^2 - \vec{u} \times rot\, \vec{u} \tag{45}$$

Assuming that the velocity fields are not time dependent, and that there is no rotating velocity field ($rot\, \vec{u} = 0$), the Equation (45) can be applied to (44), resulting in Equation (46).

$$\frac{1}{2} grad\, \vec{u}^2 = -\frac{1}{\rho} grad\, p - \vec{g} \tag{46}$$

The gravitational vector can be expressed as a gradient in vertical direction z, according to Equation (47).

$$\vec{g} = grad(gz) = \begin{pmatrix} 0 \\ 0 \\ g \end{pmatrix} \tag{47}$$

Inserting Equation (47) into Equation (46), the gradient can be extracted as demonstrated in Equation (48), since all terms are expressed as gradients.

$$grad\left(\frac{\vec{u}^2}{2}+\frac{p}{\rho}+gz\right)=0 \tag{48}$$

If the gradient of the added terms is zero, the sum of the terms must be constant. This results into the Bernoulli equation (49).

$$\frac{\vec{u}^2}{2}+\frac{p}{\rho}+gz=\text{const} \tag{49}$$

During the derivation from the Euler equation to reach the Bernoulli equation, it must be assumed that rotational velocity fields do not exist. Since the rotational field is represented in FSW by the rotational field of the backflow of the mass flow $\dot{m}_2$, it results in the demand that the mass flow $\dot{m}_2$ around the probe must be considered zero. However, to demonstrate the influence of the mass flow $\dot{m}_2$, this term was crossed out only from the final equation. For a balance of energy, the mass flows $\dot{m}_1$ and $\dot{m}_2$ add up to mass flow $\dot{m}_3$. Through the application of the Bernoulli equation with the constant mass flows $\dot{m}_1$, $\dot{m}_2$, and $\dot{m}_3$, and considering no gravitational influence and constant energy, the Equations (50) and (51) are obtained. The influence of the individual values on the modified Bernoulli equation is evaluated. The welding speed in relation to the orbital velocity of the rotational speed is low. Therefore the velocity u_1 is defined by the welding speed, while the velocity u_3 is majorly influenced by the rotational speed. As a result, it is assumed that $u_1 \ll u_3$. According to the equation, if $\dot{m}_2$, equals 0, the pressure p_1 must be much higher than p_3 ($p_1 \gg p_3$).

$$E_1+E_2=\ E_3 \tag{50}$$

$$\underset{\ll u_3}{\cancel{\frac{m_1\vec{u}_1^{\ 2}}{2}}}+\frac{m_1p_1}{\rho}+\underset{=0}{\cancel{\frac{m_2\vec{u}_2^{\ 2}}{2}}}+\underset{=0}{\cancel{\frac{m_2p_2}{\rho}}}=\frac{m_3\vec{u}_3^{\ 2}}{2}+\frac{m_3p_3}{\rho} \tag{51}$$

The elevated pressure p_1 in front of the probe is not described in literature. As an indication of the existence of this phenomenon, some papers described the sudden stop action technique, which means that the weld was stopped by the failure of the probe. In these studies there was no visible material flow on the AS [64, 76]. As an example, the welding condition with a broken probe is presented in Figure 11 (Section 3.3). The missing mass flow $\dot{m}_2$ leads, according to Equation (51), to elevated pressure p_1 in front of the probe and this could be the reason for the failure.

It follows the hypothesis that the missing $\dot{m}_2$ flow supports the observed increase of pressure in the experiments when the welding conditions become suddenly unstable. This can be the reason for the failure of probes in the SSBT experiments.

5.5.3 Initiation of Material Flow through Mass Flow $\dot{m}_2$

The Bernoulli equation gives a comprehension of the importance of the mass flow $\dot{m}_2$ on the active pressure in the SZ. However, it only shows this influence by the consideration that a rotational flow field does not exist. In FSW the mass flow $\dot{m}_2$ does exist for stable welding conditions as presented in this study and in the literature. To describe the influence of the mass flow $\dot{m}_2$, the boundaries of the welding process model were adapted according to Figure 49. Considering a plane normal to the welding direction at the centre of the probe, as in Figure 49, the flow is governed by the flow in welding direction or opposite to it. The total flow around the probe can be described with this cutting plane at the right side boundary of the considered system. By reducing the observed system in this way, the energy transported through the boundaries by the mass flows $\dot{m}_1$, $\dot{m}_2$, and $\dot{m}_3$ can be evaluated separately.

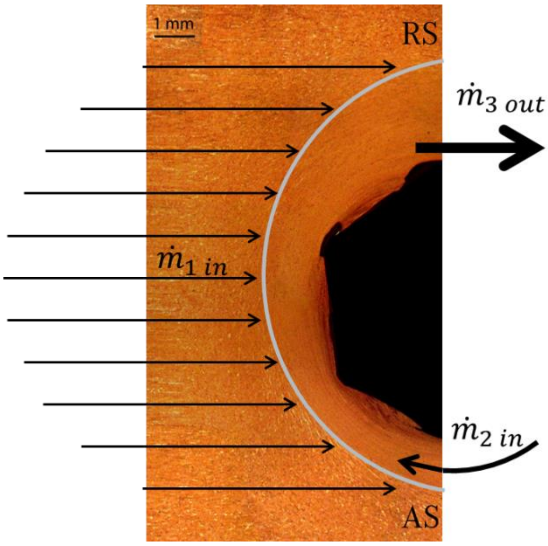

Figure 49. Redesigned system boundaries for thermodynamical model.

An analytical model of the energy fluxes through the model boundaries is described for the complex welding situation in Figure 50. The energies transported by the mass flows $\dot{m}_1$, $\dot{m}_2$, and $\dot{m}_3$ are described in horizontal direction. The energy input and output of the system are indicated in vertical direction. For the change of enthalpy in the mass flows $\dot{m}_1$, as example the phase changing entropy and the Gibbs energy, the term $\Delta\dot{H}_{\dot{V}_1}$ was added.

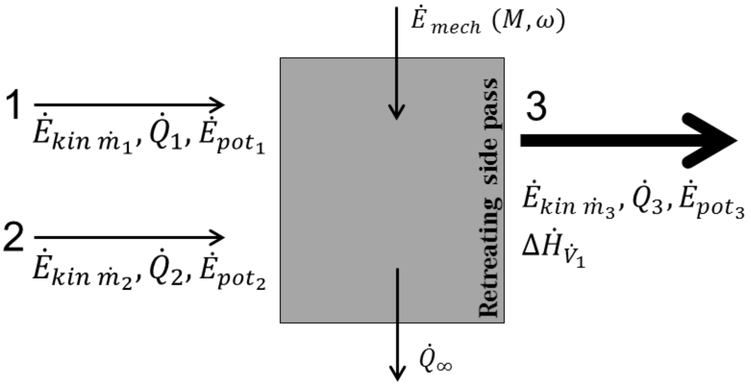

Figure 50. Scheme of the thermodynamical model for the balance of the energy fluxes of the weld zone.

As indicated before in Figure 49, the mass flow $\dot{m}_2$ has an impulse in the counter direction of the mass flow $\dot{m}_1$. This opposite movement induces a faster redirection and transportation of $\dot{m}_1$, than only induced by the moving components of the tool. Concerning heat transfer; it can be assumed that the mass flow $\dot{m}_2$ contributes also in heating the incoming material $\dot{m}_1$ at the AS. Thus, the magnitude of the mass flow $\dot{m}_2$, assuming similar temperatures in the SZ, has a direct influence on the transported heat.

The right side boundary of the Figure 49 is comparable to the plane of the CFD model described in Section 5.3. In the simulation, numerical evaluations were proceeded in the plane of the CFD model on the AS for the mass flow $\dot{m}_2$ and on the RS for the mass flow $\dot{m}_3$. The equations evaluated the volume for the mass flows $\dot{m}_2$ and $\dot{m}_3$, the kinetic energy of these flows, and the area crossed by them. The same operations were conducted for the mass flow $\dot{m}_1$ on the inlet boundary. Assuming incompressibility, the mass flow can be derived from the transported volume $\dot{V}$ according to Equation (52).

$$\dot{m} = \dot{V}\rho \tag{52}$$

The volume results from the plane with the integrational boundaries for the u component of the velocity $u \leq 0$ on the AS, and $u \geq welding\ speed$ on the RS, as shown in Equation (53).

$$\dot{V} = \int \vec{u}\, dA \tag{53}$$

The same integrational boundaries can be used for the kinetic energy of the mass flows passing through the plane, as given in Equation (54).

$$\dot{E}_{kin} = \frac{1}{2}\rho \int \vec{u}^3\, dA \tag{54}$$

The kinetic energy of a mass flow is a mechanical power and the incoming mass flow $\dot{m}_2$ is suggested to have significant influence on the flow initiation and as a result in experimental feasibility. Therefore two parameters were introduced from the simulation. First, a relation between the incoming ($\dot{E}_{kin2}$) of the mass flow $\dot{m}_2$ and the outgoing ($\dot{E}_{kin3}$) kinetic energy of the mass flow $\dot{m}_3$ was defined as the **r**elative **rot**ating **k**inetic **e**nergy ($\mathrm{R_{Rot}KE}$) in Equation (55).

$$R_{Rot}KE = \frac{\dot{E}_{kin2}}{\dot{E}_{kin3}} \tag{55}$$

And second, a relation between the incoming kinetic energy of $\dot{m}_2$ for each process variant ($\dot{E}_{kin2}$) and the incoming kinetic energy of $\dot{m}_2$ for the conventional SRBT process variant at a welding speed of 300 mm/min with the 6mm probe diameter ($\dot{E}_{kin2_{ref}}$) was established. The studied and feasible conventional SRBT process variant is taken as a reference process variant for the **r**elative to **ref**erence **k**inetic **e**nergy ($\mathrm{R_{Ref}KE}$) in Equation (56).

$$R_{Ref}KE = \frac{\dot{E}_{kin2}}{\dot{E}_{kin2Ref}} \tag{56}$$

The combination of these two parameters can give an indication of the experimental feasibility of the process variants.

In general, high $R_{Rot}KE$ means that the kinetic energy of the mass flow $\dot{m}_2$ is similar to the mass flow $\dot{m}_3$. This condition seems to establish a continuous flow around the probe even at low welding speeds (low mass flow $\dot{m}_1$). In addition, the related $R_{Ref}KE$ should show a value which indicates that the energy of the mass flow $\dot{m}_2$ is capable to initiate material flow at the AS. For example, a welding process variant with low $R_{Ref}KE$ implicates a slow or small mass flow $\dot{m}_2$ resulting in a limited feasibility of the process variant. This is shown in Section 5.5.2 for a mass flow $\dot{m}_2$ equal to zero. Welds with elevated $R_{Ref}KE$ are expected to result in unstable behaviour at lower speeds. The elevated kinetic energy of the rotating mass flow colliding with the incoming rigid material on the AS could be the reason for this unstable behaviour. This matter is discussed further in Section 5.5.5. Yet, high values of $R_{Ref}KE$ seem to be necessary for elevated welding speeds, since the fast incoming material on the AS of mass flow $\dot{m}_1$ needs to be initiated by heat and impulse transfer. A low mass flow $\dot{m}_2$ would result not only in low $R_{Ref}KE$, but also could result in low $R_{Rot}KE$. In all evaluated welds, there was no case of outstanding low $R_{Rot}KE$, which means that in the simulation there is always a high influence of the kinetic energy of the mass flow $\dot{m}_2$.

Table 7 displays the results calculated from the CFD simulations with effective viscosity model based on ln. The values were obtained from the simulations previously presented in Table 6. It can be referred to Table 4 and Table 5 for the comparison of the effects of the simulated values on the surfaces and macrographs of the welds. The description of the process variants was focused on the describtion of the viscosity based on ln, but the viscosity based on $sinh^{-1}$ can be evaluated in equally manner. These results can be found in the Appendix C. The indices in the Table 7 were used in agreement with Figure 49 and Figure 50. Since the integration for the evaluation of the mass flows is based on an area, the areas are also compared. The simulation were conducted with a symmetric and with an asymmetric probe shape. The latter is the CAD geometry on which the probes for the experimental procedure were manufactured. The volume consistency can be evaluated adding the $\frac{\dot{V}_1}{\dot{V}_3}$ and $\frac{\dot{V}_2}{\dot{V}_3}$ terms. Based on the consistency, the sum must result in 100%. For the symmetric probe geometry this was the case within a tolerance of 0.01%. However, for the slightly asymmetric geometry; the area of AS and RS slightly differ which results into an inconsistency of volume flows. This becomes especially present at high welding speeds and small areas of the SZ.

Table 7. Results from the simulations with viscosity model based on ln. The conventional self-reacting bobbin tool (SRBT) equipped with probe diameter of 6 mm and 7 mm, the semi-stationary shoulder bobbin tool (S^3BT) in stationary lower shoulder (S^3BT-SLS) and stationary upper shoulder (S^3BT-SUS) configuration, and the stationary shoulder bobbin tool (SSBT) with the probe as the only rotating tool part in stepped and straight probe design configuration

Simulation № and Process Variant		Welding speed [mm/min]	$\frac{\dot{V}_1}{\dot{V}_3}$	$\frac{\dot{V}_2}{\dot{V}_3}$	$\frac{\dot{E}_{kin2}}{\dot{E}_{kin3}}$ $\mathrm{R_{Rot}KE}$	$\frac{\dot{E}_{kin2}}{\dot{E}_{kin2Ref}}$ $\mathrm{R_{Ref}KE}$
1	SRBT-6 mm	120	3%	97%	94%	33%
2	SRBT-6 mm	300	5%	95%	91%	100%
3	SRBT-7 mm	300	4%	96%	93%	210%
6	S^3BT-SUS	1850	42%	58%	58%	72%
7	S^3BT-SUS	2000	42%	58%	58%	88%
8	S^3BT-SUS	2500	43%	57%	57%	165%
9	S^3BT-SUS	2950	47%	53%	53%	190%
10	SSBT-stepped	100	6%	94%	92%	9%
11	SSBT-straight	100	19%	82%	82%	1%

As seen in Table 7, the three conventional SRBT variants present an important base for comparison. All conventional SRBT welds were conducted with high kinetic energy of the mass flow $\dot{m}_2$ entering on the AS ($\mathrm{R_{Rot}KE}$ = 93 to 97%). Even though the difference in the $\mathrm{R_{Rot}KE}$ is small, the $\mathrm{R_{Ref}KE}$ increases in magnitude by almost seven times. While the SRBT process variant equipped with a probe of 6 mm diameter and with a welding speed of 120 mm/min in weld 1 was conducted with a smooth finish and with no difficulties of oscillation at a $\mathrm{R_{Ref}KE}$ of 33%, the weld 2 with 300 mm/min welding speed with a $\mathrm{R_{Ref}KE}$ of 100% showed good quality welding results at the limit of the capability of the handling system. In comparison, the SRBT process variant at the same welding speed of 300 mm/min but equipped with a 7 mm probe weld 3 was calculated with a $\mathrm{R_{Ref}KE}$ of 210% and resulted in unstable behaviour of the handling system during the welding process. This becomes evident in weld 3 with a rough surface appearance and an increased area of the SZ. The instability was observed at higher welding speeds during the experiments. The elevated $\mathrm{R_{Rot}KE}$ and $\mathrm{R_{Ref}KE}$ of conventional SRBT process variant, which represents a high transported volume in a continuous counter flow on the AS around the probe, could explain the higher reaction or process forces and the limitations of welding speed. This indication is seen in the maximum welding speed of 300 mm/min achieved for the conventional SRBT process variant.

In direct contrast to the SRBT process variant equipped with a 7 mm probe, the SSBT with the straight probe in weld 11 was not feasible in the experimental work with only 1% of $\mathrm{R_{Ref}KE}$. Furthermore, the small amount of transported material volume is reduced because of the reported material loss due to entrapment in the tool in the straight probe configuration (Figure 27). The SSBT including the stepped probe design in weld 10 was evaluated to have a $\mathrm{R_{Ref}KE}$ of 9% and showed experimental feasibility. For the SSBT process variants the influence of the reduced welding speed to 5/6 of the conventional

SRBT weld 1 must be pointed out. As seen in the SRBT process of weld 1 and weld 2 the $R_{Ref}KE$ increases from 33% to 100% (factor 3) by increasing the welding speed by factor 2.5.

The studied variants with mid-range $R_{Rot}KE$ worked very stable at high welding speeds and seem to depend on the $R_{Ref}KE$ values, which rise with the increasing welding speed. As an example, the S^3BT-SUS variant with mid-range $R_{Rot}KE$ (around 55%) reaches higher welding speeds with comparable values of $R_{Ref}KE$ (88% at welding speed 2000 mm/min) comparable to the referenced process of the SRBT process variant with the 6 mm probe diameter (by definition a 100% at welding speed 300 mm/min). The welds 6 to 9 of this process variant resulted in the most stable behaviour observed during the experiments. The incoming kinetic energy of the mass flow $\dot{m}_2$ seems to be enough to initiate the flow, but not to result in the oscillating deviation of the machine components that guided the process. For the S^3BT-SUS the $R_{Rot}KE$ stays within the range of 53% to 58% for the welding speeds conducted in the experiments. It can be observed that the $R_{Rot}KE$ decreases in non-linear behaviour with increasing welding speed, while the $R_{Ref}KE$ is increasing.

In summary, it can be proposed that the collision on the AS between the $\dot{m}_1$ and the $\dot{m}_2$ must occur to initiate the material transport around the probe. Yet, the reaction forces from the momentum exchange should be adjusted to a minimum necessary for the process. This can be done by two approaches, each involving a different process variant. For low welding speeds, the conventional SRBT with a high $R_{Rot}KE$ results in a stable flow around the probe and initiates the slowly fed material of the mass flow $\dot{m}_1$. For high welding speeds, the S^3BT process variant initiates the fast incoming mass flow $\dot{m}_1$ with mid-range $R_{Rot}KE$. Furthermore, it is observed that process variants with either very high or very low $R_{Ref}KE$ lead to challenges in the feasibility of the experiments if the welding speed used is comparable to the referenced SRBT process variant with the 6 mm probe diameter and the welding speed of 300 mm/min. The upper limit of the $R_{Ref}KE$ at a certain welding speed is suggested to be specific for each handling system. This limit is suggested to be a border for the reaction forces from the momentum exchange on the AS handled by the equipment before unstable welding conditions occur.

The values for the mass flow $\dot{m}_2$ on the AS during the experiments can be anticipated to be lower than the values received from the simulation. In the simulation the cross section of material flow of the S^3BT process variants on the AS is comparably high to the evaluation of the experiments as seen in the overlay of the simulation in Figure 40. The simulated velocity field is a simulated cross section of diameter 1 in Figure 45, but it is validated as an overlay with the diameter 2 in Figure 46 of the cross section of the macrographs. Since an in-situ evaluation of the macrostructure is a challenge, the procedure of evaluating the macrostructure behind the process zone is commonly done in literature as, for example, by Hilgert [1].

5.5.4 Discretized Mass Flows: Side View

In fluid mechanics, a flow can be driven by the shear and pressure [143]. In FSW, both are active. The pressure is induced by the forward movement of the welding tool and is proportional to the force applied in the welding direction.

The shear stress in FSW is applied by the rotating components of the tool. The moving shoulder has a high influence on the flow of the material in its vicinity [68, 71]. In the conventional SRBT process variant, the gap force induces friction between the shoulder and the material. The material is plasticized and a flow is induced in circumferential direction around the probe. Also, the surfaces of the probe induces or supports the flow through shear stress on the material. In Figure 51 (a) and (b), the flow is discretized for conventional SRBT and S^{3}BT-SLS process variants, respectively. Considering the conventional SRBT variant, it can be proposed that the incoming material flow is moved first by the upper rotating shoulder at the very outside radius. This flow establishes and the discretized horizontal flow layers are influenced by the flow one-by-one until reaching the middle region between the rotating shoulders. The same mechanism can be proposed for the S^{3}BT-SLS process variant, starting at the rotating shoulder and proceeding in narrower shear layers approaching the stationary shoulder.

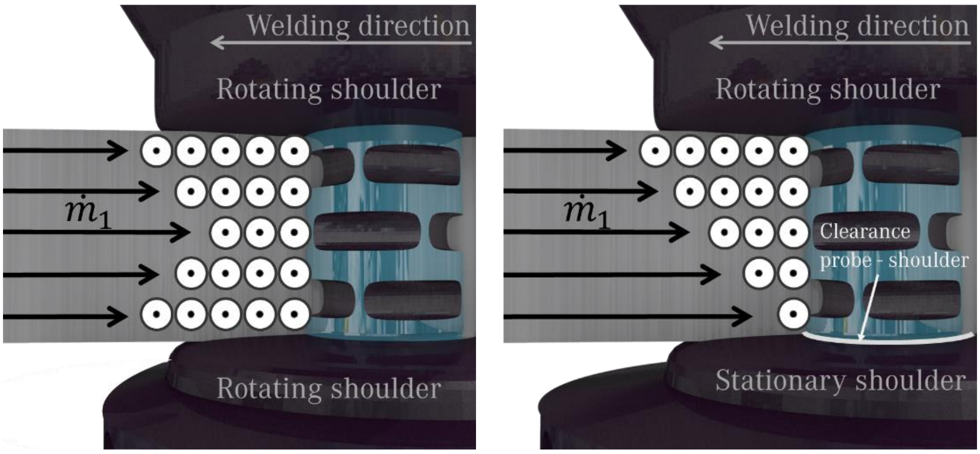

(a) (b)

Figure 51. Material transport caused by moving shoulders and influence of discretized vertical flow vectors on initiation of adjacent flow in between the discretized vertical flow layers for (a) the conventional SRBT and (b) S^{3}BT process variants, demonstrated as an example for S^{3}BT-SLS.

5.5.5 Stirred Zone Formation

The interaction between the rotating material and the incoming cold material was described previously regarding the energy of the mass flows (Section 5.5.3). For the S^{3}BT-SLS process variant, a widening of the SZ on the trailing side of the probe was observed in the mid-thickness top view macrograph of Figure 45. The same behaviour can be seen in Figure 46 in vicinity of the rotating shoulder. The diameter of the SZ on the AS is increased at the trailing side of the probe compared to the centreline.

In the introduced discretization of the flows of Figure 51 (b), the mass flow $\dot{m}_2$ is depending on the distance to the rotating shoulder. As suggested in Figure 52, the mass flow $\dot{m}_3$ is divided on the trailing side of the probe into the deposited material and the mass flow $\dot{m}_2$ that continues rotating to the front of the probe. The collision behind the probe between the welded material ($\dot{m}_{3\,deposit} = \dot{m}_3$- $\dot{m}_2$) and the rigid mass flow $\dot{m}_4$ can explain the formation of the widened SZ. The amount of $\dot{m}_{3\,deposit}$ which stays on the trailing side of the probe has an influence on the size and the shape of the SZ. It is also suggested that the collision between the deposited mass flow $\dot{m}_{3\,deposit}$ and the rigid solid material on the AS contributes to the side forces measured during the welding process. The interaction of the mass flows seems also to contribute on the formation of the onion ring pattern on the advancing trailing side of the probe and supports the description of Kumar [144].

The location of interaction between $\dot{m}_1$ and $\dot{m}_2$ depends on the vertical distance to the rotating shoulder and changes along the thickness of the welded work piece. The shear layers driven majorly by the rotating shoulder cause the formation of the SZ on the AS closer to the centreline of the tool, as it can be seen in Figure 46. The shear driven flow depending on the probe leads to a formation of the SZ on the AS shifted to the trailing side of the probe. Approaching the stationary shoulder side,

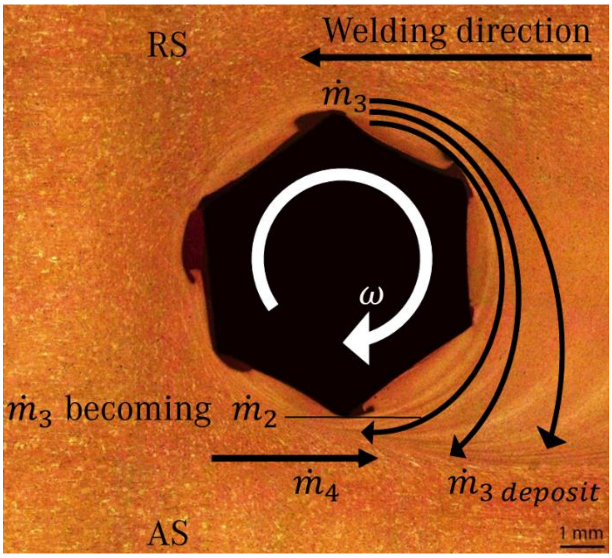

Figure 52. Collision between $\dot{m}_4$ and $\dot{m}_3$ mass flows on the trailing side of the probe.

there is a gradual reduction of the mass flow $\dot{m}_2$ due to the lack of transportation by the shear stress. The shear stress is lower in the region closer to the stationary shoulder because the material flow layers above are reduced in size and the orbital velocity of the probe's surface is reduced. The reduction in the horizontal shear layers is indicated schematically in the Figure 51 (b).

The existence of a critical spot for the consolidation of the weld is suggested and the radial location around the probe is indicated in Figure 53 (a). This is the region of the highest shear between the incoming material and the rotating material is in the weld zone. For the S^3BT-SLS process variant, the flow decreases from the rotating to the stationary shoulder in the vertical direction, indicated in Figure 54 (a). This decrease results in a critical spot for insufficient flow close to the stationary shoulder as demonstrated in Figure 53 (b), which could be observed during the experimental procedures. In general, each discretized layer influences the layers in vicinity. The probe supports the initiated material transport of the shear layers. Therefore, the critical point of transport is on the AS, in the furthest region from the first initiated shear layer. This region of the SZ is not solely depending on the distance to the rotating tool components.

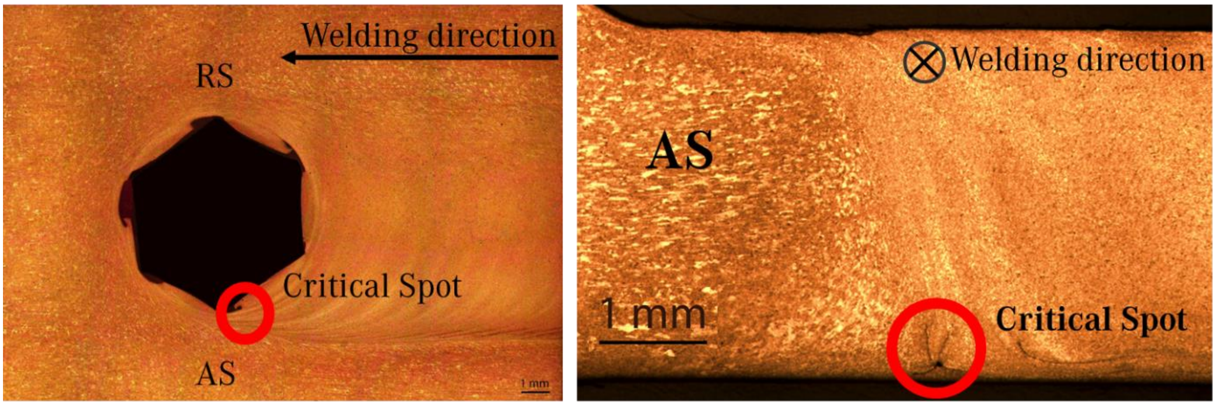

(a) (b)

Figure 53. Critical spot in macrographs of a weld obtained with S^3BT-SLS process variant in (a) top view and (b) cross section on the AS.

In Figure 54 (a) to (c), the critical spots are given, respectively, for the process variants of the S^3BT-SLS, conventional SRBT, and SSBT in stepped probe configuration. For the conventional SRBT process

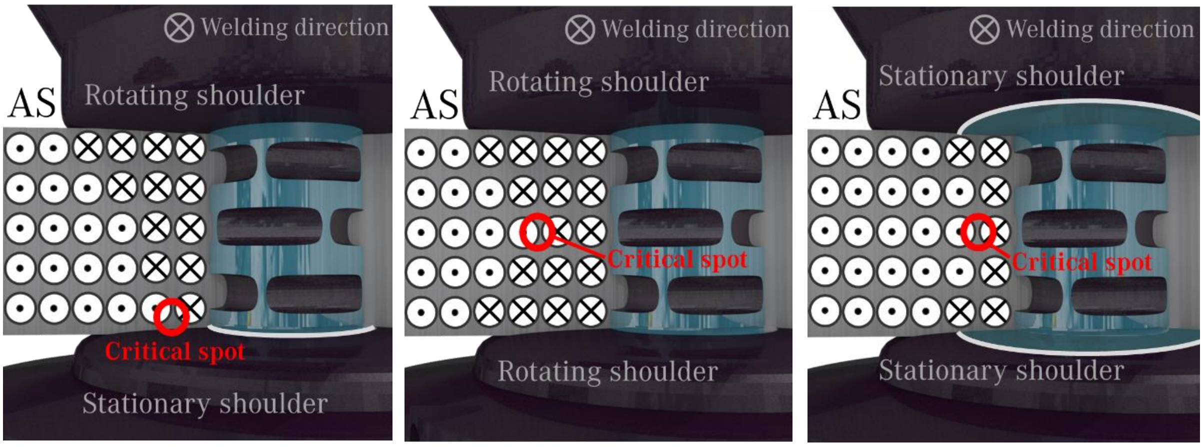

(a) (b) (c)

Figure 54. Models for the critical spot on the AS in (a) S^3BT-SLS, (b) conventional SRBT and (c) SSBT-stepped process variants.

variant, the critical spot was observed in the experimental studies and in the work of Hilgert [1], but not described, and during the present study. For the SSBT process variant including the stepped probe, an indication of the critical spot is found in the macrograph of weld 10 (Table 5). The S^{3}BT-SUS variant has the vertically mirrored behaviour of the presented S^{3}BT-SLS variant. Similar critical spots were also found in conventional FSW in a study by Lorrain et al. Difficulties of initializing material flow are reported with unthreaded tools, which naturally initiate less material volume than threaded tools and results in less transmitted shear stress in between the shear layers [79].

The stable and continuous horizontal flow in the S^{3}BT variants demonstrated in Figure 51 (b) can be the reason for the smaller material loss to the shoulders due to entrapment during the welding process. With the same probe-shoulder components used in the SSBT process variant with the straight probe from the S^{3}BT process variants, a high volume of material entrapped in the tool has been observed as indicated in Figure 55 (a) as described in Section 5.2.2.

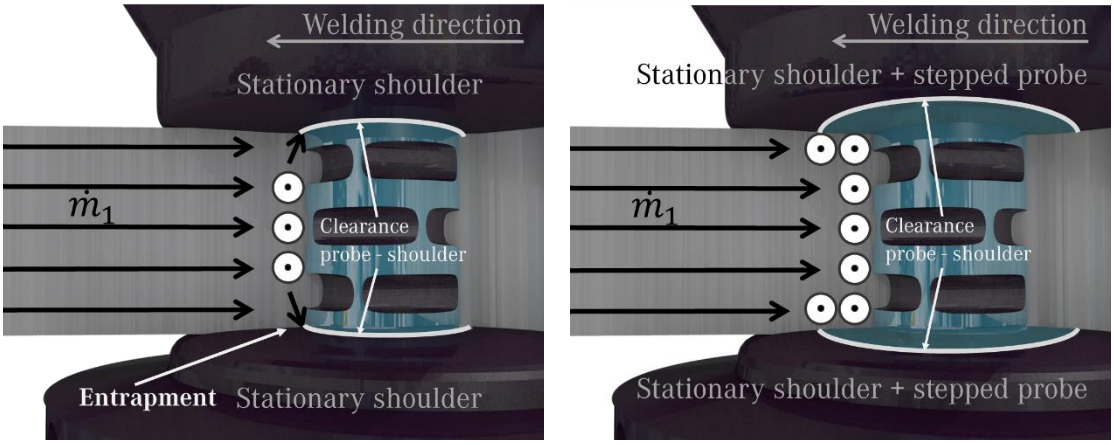

(a) (b)

Figure 55. Flow initiation through shear stress of the SSBT process variant with (a) the straight probe and the material entrapment indicated through vertical flow and (b) stepped probe.

The elevated welding and rotational speeds applied in the S^{3}BT process variants can be one reason for a stable and continuous rotating flow. Another reason can be the reduced heat input, which causes a higher viscosity of the material in the weld zone. This higher viscosity can suppress the vertical flow to the shoulders and, consequently, the entrapment of material. Yet, the reduced mass flow $\dot{m}_2$ for the SSBT process variant with the straight probe design (Section 5.5.3) induced an insufficient flow condition, and led to high forces. Increased welding speeds resulted in even higher forces and failure of the probes.

However, a redirection of the incoming mass flow $\dot{m}_1$ was also achieved with the SSBT process variant with the stepped probe design given in Figure 55 (b). The stepped probe design helped to induce flow around the probe and also gave a solid edge for redirecting the flow in the high pressure area directly on the vertical surface of the probe. The material loss due to entrapment was reduced.

A further support for the discretized shear layer approach and the assumption of no vertical flow are presented in the results of the marker material experiments in Section 5.6.1.

5.6 Validation of the Analytical Modelling

5.6.1 Marker Material Experiments

In literature, marker material experiments with the single-sided FSW process reported similar material flow patterns to those observed in the present work [65, 72, 74, 79, 90]. Simulation of particle flow supporting these findings can be found in [86-88, 90, 91]. These sources, however, describe the conventional FSW process.

The behaviour of the material flow suggested in the previous sections is supported by the experiments with marker material in the present study. The marker material studies were conducted with S^3BT-SUS process variant according to Section 4.5.1, and evaluated by X-ray analysis. In Figure 56 (a) and (b) the photograph of the welded sample with Ti-powder marker material and the X-ray image are presented, respectively.

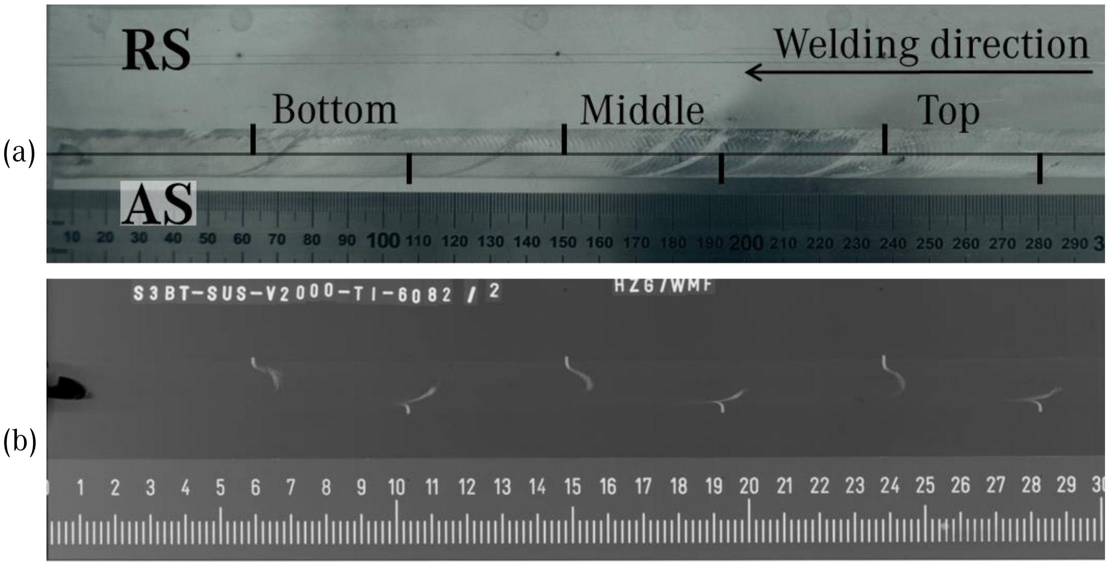

Figure 56. (a) Scheme of the marker material inserts in a pre-weld condition and (b) X-ray image from the weld conducted with the S^3BT-SUS process variant.

The distribution of the transported marker material in post-weld condition can be compared to the original position indicated in Figure 56 (a). It can be observed that the marker material distribution differs on the AS and the RS after the welding process. Magnified images of the distribution in the different levels of the work pieces thickness on the AS and RS are given in Table 8. For a better visualization, a weld centre line is added to all X-ray images.

Table 8. Detailed view from deposition of marker material on RS and AS in the different thickness levels of the weld

	Top	**Middle**	**Bottom**
Thickness level	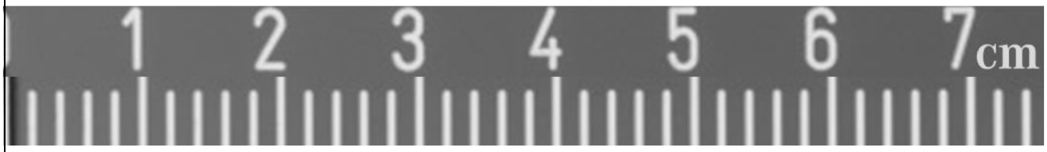		
RS	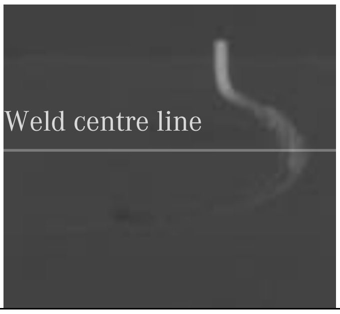	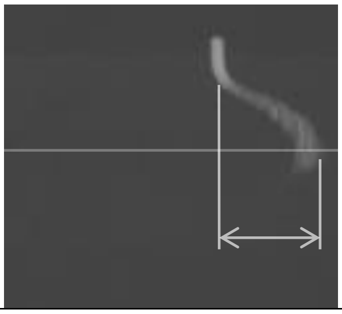	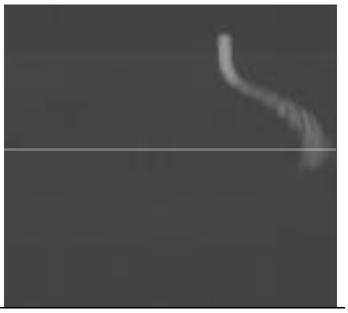
AS	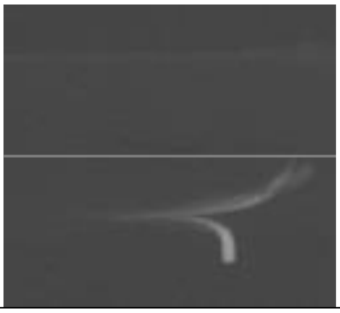	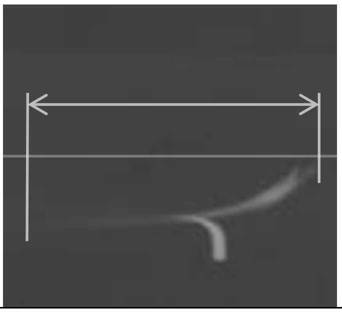	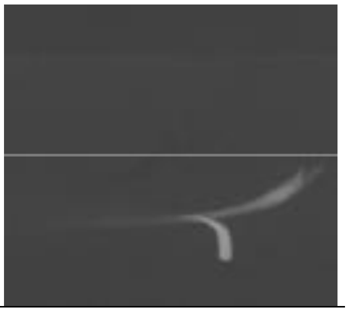
		← Welding direction	

The Ti-powder on the RS is solely transported against the welding direction. As a result, a sickle shape distribution of the marker material can be noticed on the RS. On the AS, it is shifted in the welding direction and opposite to it. The resulting shape can be compared to the tail of a comet. This distribution spreads over a longer distance of approximately 20 mm, in comparison to 9 mm on the RS. In general, the level of the marker material on the thickness of the work pieces had little influence on the allocation in post-weld condition.

Material flow in vertical direction is reported in literature for conventional FSW and for fixed-gap BT-FSW [41, 65]. In order to observe the vertical flow in the new S^{3}BT-SUS process variant, the welds were cut next to the weld seam and X-ray images from the side view were produced. As an example, the X-ray image obtained for the weld performed with the S^{3}BT-SUS process variant with a welding speed of 2000 mm/min is presented in Figure 57. No significant material flow in vertical direction for the marker material inserted in the mid-thickness level is observed in the magnified images in Figure 57. This observation of no significant vertical flow occurred at all levels of the work pieces thickness. The observed vertical flow for this process variant is not significant when compared to the reported vertical flow in the conventional FSW.

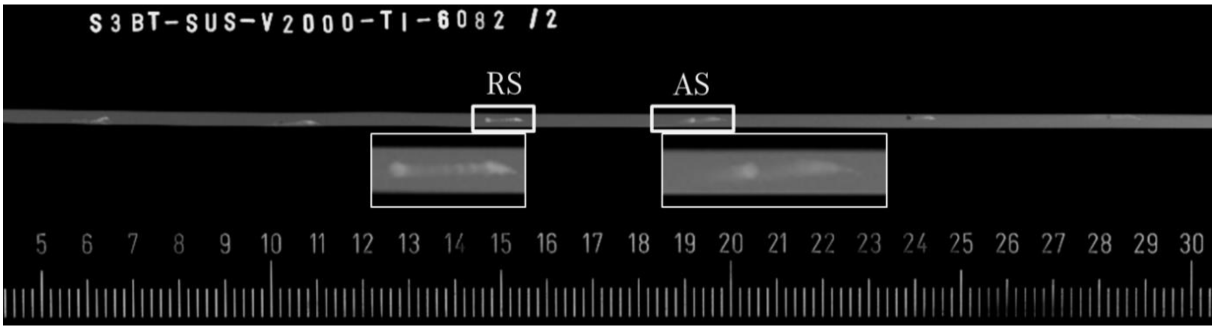

Figure 57. X-ray image from the side view of S³BT-SUS weld seam with detailed marker material in mid-thickness level for the RS and AS.

It is reported in literature that the final position of the marker material depends on its distance to the weld centre line (Figure 9). To capture the dimensions of the deposited marker material and the CFD velocity field, both are presented in Figure 58. The dimensions of the SZ on the AS are smaller and close the probe, while on the RS the SZ is wider, as seen in this figure and in the CFD velocity field of Figure 39.

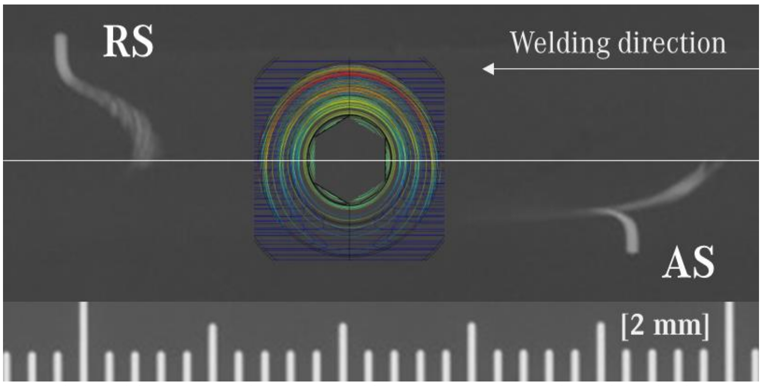

Figure 58. X-ray image of the weld after marker material experiment overlayed with the simulated velocity field.

For a further explanation of the material flow around the probe, the marker material is discretized according to the model in Step I of Figure 59. One model is proposed for the transport of the discretized marker material from the original position to the final position for the RS and another model for the AS in Figure 59 and Figure 60, respectively. The images are disposed following the welding direction (from right to left) for a better understanding of the flow mechanisms. The patterns of the marker material are taken from the X-ray images in Figure 58.

The probe interacts with the marker material particles as it moves forward in the welding direction. The closest particle to the centre of the SZ is deposited after travelling about 180 degrees around the probe, as demonstrated in Step I and II of Figure 59. The next particle enters the SZ at a greater distance to the weld centre line and travels a smaller rotational angle, before it is deposited at a comparable distance to the centre of the weld. This is demonstrated in Step II and III. Particle 3 is influenced by the plasticized material similarly, as the moved rotational angle is further decreased and the distance to the weld centre line is comparable before and after the weld. According to this simple model, the final position of the marker material is governed by its previous distance to the weld centre line. The greater the distance, the lower is the influence of the rotational movement applied on the particle.

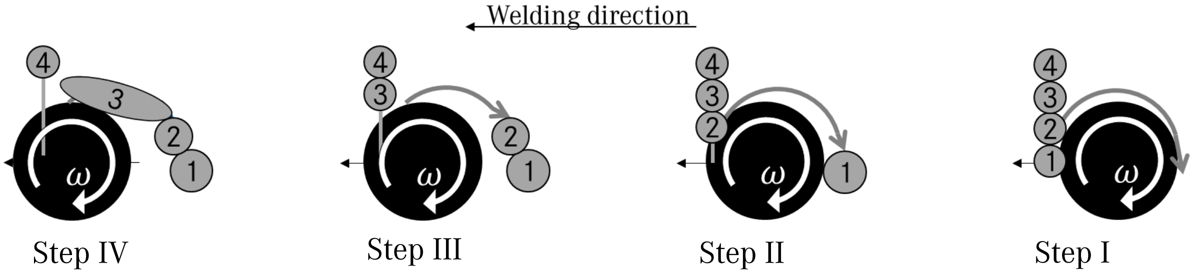

Figure 59. Scheme for the suggested mechanism of displacement for the marker material observed in X-ray images on RS: (a) first contact, (b) transportation of discretized marker material particle 1, (c) transportation of particle 2 and (d) partial transportation of particle 3.

The description of the material flow pattern on the AS is more complex. The discretized mass flows $\dot{m}_i$ introduced in Section 5.5 are used to explain the present model. The marker material represents a part of the incoming mass flow $\dot{m}_1$. As described earlier, $\dot{m}_2$ collects $\dot{m}_1$ along the foreside of the probe. The accumulation of the material starts on the AS with the incoming $\dot{m}_2$, resulting in the mass flow $\dot{m}_3$. Furthermore, it is suggested that the particle flow travels in orbital layers. Depending on the distance to the weld centre line, the collection of $\dot{m}_1$ by $\dot{m}_2$ progresses and the radius of SZ increases (Figure 46). Therefore, the vicinity of the collected material to the probe is defined.

The closest particle to the weld zone centre line on the AS in Step I of Figure 60 has a similar movement to the one described on the RS (Step I of Figure 59). Then, one part of particle 2 is deposited on the trailing side of the probe according to Step II and III of Figure 60. The other part of particle 2 stays in the vicinity of the probe and rotates in the SZ, as previously demonstrated in the macrograph of the sudden stop action technique (Figure 52). The furthest particle from the weld zone centre line is the first affected by the incoming material flow $\dot{m}_2$. Therefore, it is collected in the closest orbit of the probe and it continues rotating in the vicinity of the probe. The material deposits on the AS due to the collision with the mass flow $\dot{m}_4$, as previously described in Figure 52.

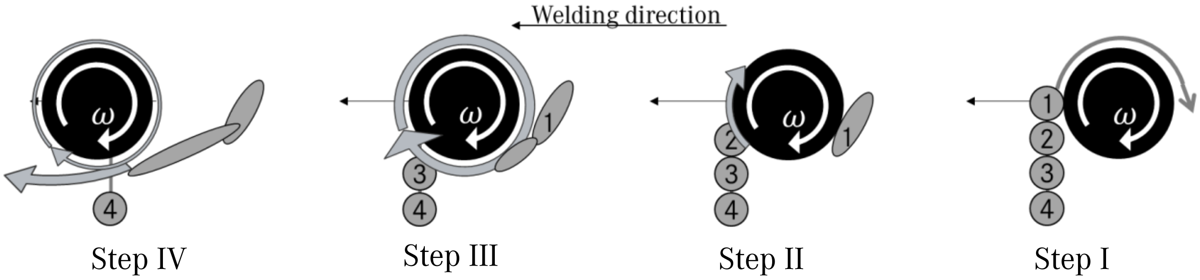

Figure 60. Scheme for the suggested mechanism of displacement for the marker material observed in X-ray images on AS. Step I) first contact; step II) transportation of discretized marker material particle 1 and contact of particle 2; step III) particle 2 is partially deposited and particle 3 starts to be captured in rotating flow around probe; and step IV) particle 3 is fully captured in rotating flow around probe and deposition occurs in combination with the collision of mass flow $\dot{m}_4$ (not displayed) ongoing with the forward movement of the tool.

The main proposal from this analytical approach is that the distance of each flow particle to the probe defines the time of permanence in the SZ. This distance is defined by the entry point of the regarded particle of the SZ. As example, the particle entering first on the AS with the $\dot{m}_2$ flow is deposited last on the AS. Figuratively, the model can be compared to a roundabout of a metropole: cars closer to the centre of the roundabout are more likely to have difficulties to get off the roundabout.

This model originates from the patterns observed in the X-ray images. Furthermore this model supports the suggested discretization of the shear layers in radial and horizontal direction, even though there can be limited interaction between the discretized layers assumed. Also supported are the described influences of the mass flows $\dot{m}_i$ and the assumed laminar flow conditions.

5.6.2 Process Forces

The governing forces in SRBT[7] process variants are the set gap force acting between the upper and lower shoulder, the resulting radial forces in welding direction (F_x) and perpendicular to the welding direction (F_y). In this section, the forces of the different process variants are evaluated from the experiments. It can be shown that the forces are related to the contact channels of the rotating tool components. An overview of the resulting forces of the different process variants is given in Table 9.

Table 9. Forces measured during the welding processes of conventional self-reacting bobbin tool (Conv. SRBT), the semi-stationary shoulder bobbin tool with the stationary upper shoulder configuration (S³BT-SUS), the stationary shoulder bobbin tool with the stepped probe design (SSBT-stepped) and straight probe design (SSBT-straight) and optional support of the stationary lower shoulder (SLS–supp.)

Weld Nº	**Process variant**	**Result**	**Welding Speed [mm/min]**	**Thickness [mm]**	**Final Gap force F_{gap} [kN]**	**Mean F_x [kN]**	**Peak-to-peak F_x [kN]**	**Mean F_y [kN]**	**Peak-to-peak F_y [kN]**
1	Conv. SRBT-6 mm	WELD	120	3	**0.83**	0.01	**-1.80**	0.27	**1.80**
2	Conv. SRBT-6 mm	WELD	300	3	**0.99**	-0.17	**-1.25**	0.35	**1.35**
3	Conv. SRBT-7 mm	WELD	300	3	**1.06**	-0.26	**-2.60**	0.61	**2.60**
7	S³BT-SUS	WELD	2000	3	**3.91**	3.54	**-0.34**	1.11	**0.10**
8	S³BT-SUS	WELD	2500	3	**3.91**	3.66	**-0.40**	0.80	**0.27**
9	S³BT-SUS	WELD	2950	3	**4.16**	3.99	**-0.38**	1.30	**0.20**
10	SSBT- stepped + SLS-supp.	WELD	100	3.6	**2.6-2.7**	3.69	**-0.09**	0.78	**0.09**
11	SSBT- straight + SLS-supp.	CAVITY	100	3.6	**2.9**	2.46	**-0.08**	1.80	**0.05**
12	SSBT- stepped	CAVITY	100	3.6	**2.6-2.7**	3.59	**-0.05**	0.69	**0.07**
13	SSBT-stepped	WELD	96	3.6	**2.8**	n.a.	**n.a.**	n.a.	**n.a.**
14	SSBT-straight	CAVITY	100	3.6	**2.8**	0.29	**-0.07**	2.30	**0.04**

---

[7] SRBT refers to all process variants of this study, since all include a self-reacting bobbin tool

5.6.3 Radial Forces

There are numerous causes to the onset of the side forces in BT-FSW. Three mechanisms have been identified in literature and in the present work to evoke these forces:

- The Magnus effect;
- The reaction forces during the collision of the discretized mass flows $\dot{m}_i$;
- The clamping of the work pieces with the rotating shoulders.

The forces perpendicular to the welding direction due to the Magnus effect are mentioned in literature [1, 50]. This effect describes a force occurring because of two movements in fluids in counter direction. The forces developed during the movement are depending – among others – on the velocity differences. In FSW, this effect can be observed on the AS, where the rotational speed of the probe is in opposite direction to the incoming mass flow $\dot{m}_4$ approaching with welding speed.

As described earlier, reaction forces must occur during the collision of the incoming rigid mass flow $\dot{m}_1$ and the plasticized mass flow $\dot{m}_2$ and, additionally, during the collision between the $\dot{m}_{3\_deposit}$ and the rigid $\dot{m}_4$ on the trailing side of the probe (Section 5.5.3 and 5.5.5).

In Figure 61, one explanation for the origin of the elevated side forces in conventional SRBT process variant is suggested. The cold material is clamped between the shoulder surfaces in an excentred position from the tool's rotational centre, as indicated in Figure 61 (a). The forces generated on the surfaces of the incoming cold material exceed the forces generated on the hot material on the trailing side of the probe, as indicated in Figure 61 (b). This condition results in a sudden and short-lived change of the rotational centre, causing a shift of the tool from the original welding path, as demonstrated in Figure 61 (c).

For the conventional SRBT process variant, the highest welding speed achieved during the present study was 300 mm/min, limited by the forces occurring during the welding. The measured radial forces components F_x and F_y on the system are presented in Table 9. Even though the mean values of F_x and F_y during the welds were comparably low to the capacity of the handling system, the machine reacted strongly to the forces visible by the naked eye. The machine was moved in an oscillating deviation perpendicular to the welding direction. During the welding process F_x and F_y fluctuated both with a peak-to-peak of 2.6 kN for the SRBT process variant with the 7 mm probe diameter. For probe diameter of 6 mm, the peak-to-peaks were 1.25 kN for F_x and 1.35 kN for F_y. The forces for the latter are plotted in the graph of Figure 62 (a).

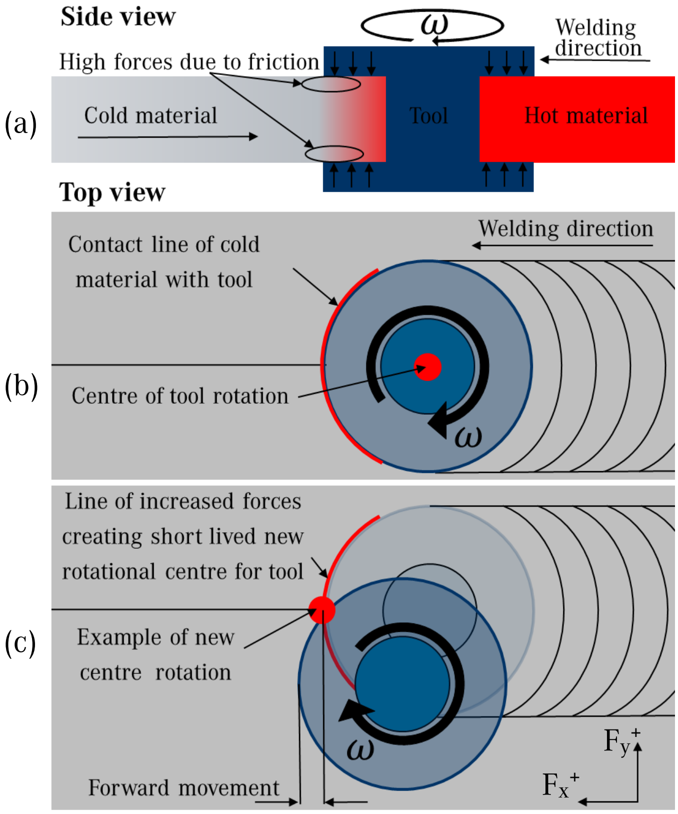

Figure 61. Scheme of the generation of side forces in conventional BT-FSW by (a) frictional forces in front of the tool due to clamping forces of shoulders. (b) Top view of the line of increased friction and (c) short lived shifting of centre of rotation, resulting forward movement.

For the conventional SRBT, negative mean values for F_x have been recorded, as displayed for welds 1 and 2 in Table 9. The change of the rotational centre resulted into a forward movement of the tool as indicated in Figure 61 (c). Thus, forces in welding direction recorded during this movement are negative. This suggestion is supported by the oscillation of the handling system during the conventional SRBT welds. Besides the forces due to the clamping mechanism, it is expected that the Magnus effect was active, because there were opposite flows on the AS. This occurrence of the Magnus effect is supported by Hilgert [1]. Moreover, it is shown that the reaction forces due to the discretized mass flows $\dot{m}_i$ are also present, as discussed in Section 5.5.3.

In comparison to the conventional SRBT, the peak-to-peaks of F_x and F_y for the S^3BT-SUS variant appeared small with ranges varying between 0.34 and 0.4 kN and 0.1 to 0.27 kN, respectively. The forces for this process variant with a welding speed of 2500 mm/min are plotted in the graph of Figure 62 (b). The clamping of the material in between two rotating shoulder elements on the foreside of the probe does not apply for the S^3BT process variants. This condition can be the reason for the reduced forces in y-direction F_y. Another positive effect might be the sliding friction force generated in the contact channel between the stationary shoulder and the work pieces. This friction can have contributed to the damping on the lateral forces.

The force F_x increased for the S^3BT-SUS variant with the increase of the welding speed from 2000 mm/min to 2950 mm/min, as given in Table 9. The change from 3.5 kN to 4 kN of the F_x seems to be small in comparison to the change in the welding speed. A correlation between the welding speed and the force F_y in the S^3BT-SUS variant could not be interpreted. Especially at the beginning of the weld the peak forces and the peak-to-peak forces are reduced. These forces are indicated in the graph of Figure 62 (b). The peak-to-peak of F_y during the beginning of the welding process was of, approximately, 7.6 kN for the conventional SRBT and 0.4 kN for the S^3BT-SUS process variant. Since the mechanisms of the stationary shoulder during the starting process are different, these values are not presented in Table 9. While there is no advance of the tool, the stationary shoulder creates a static friction between the work pieces and the handling system. Hence, the radial forces are reduced. On the other hand, the movement in welding direction has to overcome the static friction when accelerating, what explains the peak of the force F_x in the beginning of the welding sequence.

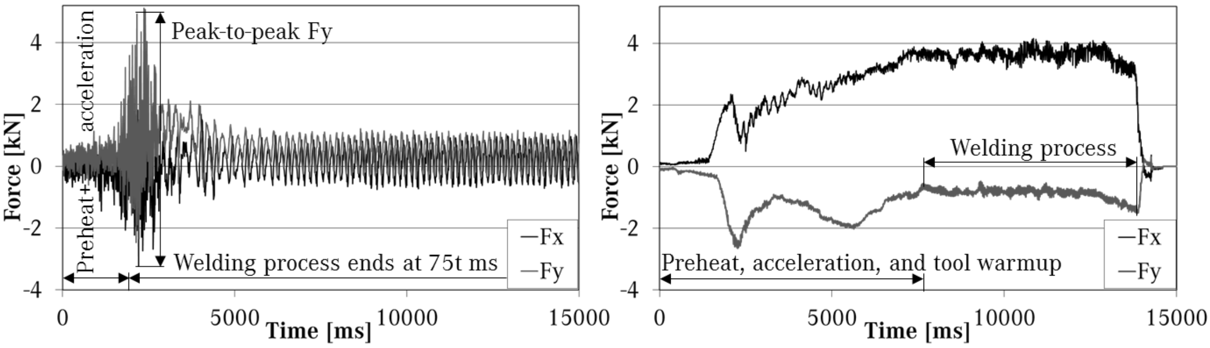

(a) (b)

Figure 62. Graphs of the radial forces of (a) SRBT with 6 mm probe diameter at 300 mm/min welding speed and (b) S^3BT-SUS process variant with 2500 mm/min welding speed.

For the S^3BT process variant the influence of the mass flows $\dot{m}_i$ is reduced, as discussed in Section 5.5.3. But according to the influence on the Magnus effect it must be mentioned that the rotational and the welding speed are remarkably high. Even though the influence of the Magnus effect can be considered elevated, the differences in the F_y forces show no dominant correlation at increase of the rotational and welding speed when comparing the welds 7 to 9 in Table 9. While the welding speed - along with the rotational speed- is increased from 2000 mmm/min to 25000 mm/min and finally to 2950 mm/min the F_y decreases in the first step from 1.11 kN to 0.8 kN and than to a final 1.3 kN.

In the SSBT experiments the forces F_x and F_y were reduced, respectively, to values between 0.05 kN and 0.09 kN, and between 0.035 kN and 0.09 kN. The higher values occurred during the experiments with the stepped probe design. The influence of the mass flows $\dot{m}_i$ was minimized for this process variant, as discussed in Section 5.5.3. The Magnus effect contribution seems rather little, since the welding and the rotational speed achieved with this process variant were low.

According to the results, it can be suggested that increased contact channels between rotating tool components and work pieces are correlated with increased amplitudes of the radial forces. The resulting increased mass flow $\dot{m}_2$ from the increased contact channels can be observed and evaluated in the simulation. With the actual CAD geometry being used for the simulation, a future approach can be the optimization of the tool design for a homogeneous mass flow $\dot{m}_2$ close to the probe.

5.6.4 Axial Forces

The gap force F_{gap}, which is the governing axial force in BT-FSW, is the parameter that controls the gap size. In the case of any SRBT process variant, the limitation of the gap size is important, since a rise above the work pieces thickness is an indication for the failure of the welding procedure. Considering that no material can be added to the weld seam in FSW, an increased gap size leads to the formation of cavity defects. In conventional SRBT quality welds were achieved with a comparable low gap force of 0.8 kN, as given in Table 9 for the weld 1. In the SSBT process variant the range of gap forces was higher.

To understand the effect of the rotating shoulder elements and of the correction of the tilted stationary lower shoulder with a support, experiments with four tool configurations of the SSBT process variant starting with the same parameters were conducted. Four bead-on-plate welds were performed, starting with a gap force F_{gap} of 2.6 kN. They were conducted with the straight and stepped probe designs, and also with and without the support of the stationary lower shoulder, as shown in the graph of Figure 63. In addition, a fifth weld including the stepped probe design with increased gap force of 2.8 kN was produced, in order to show a relation between the support of the stationary lower shoulder and the gap force F_{gap}.

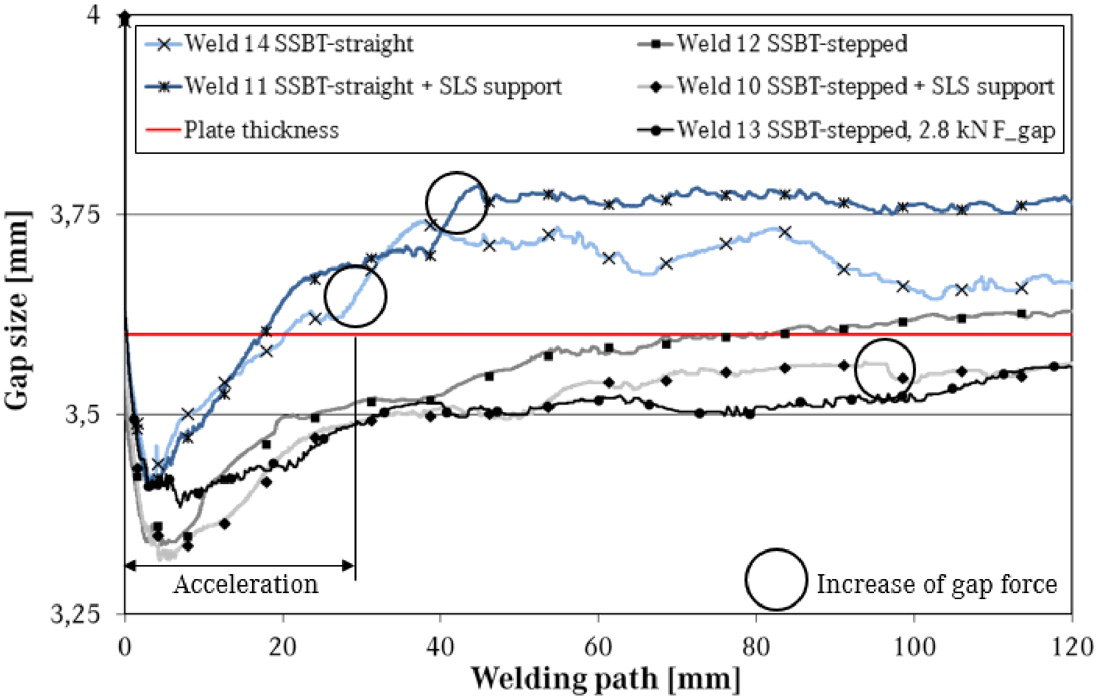

Figure 63. Comparison of SSBT welds conducted with same parameter sets and different tools.

The consolidated welds 10 and 13 in Table 9 achieved with the SSBT in stepped probe configuration, applied axial forces that varied from 2.6 kN to 2.8 kN. These welds were performed with the additional support of the stationary lower shoulder with a gap force F_{gap} of 2.6 kN and after correction 2.7 kN as well as with without the support including 2.8 kN gap force F_{gap}. Within these welds, values of gap size below the thickness of the work pieces were obtained throughout the whole welding process, as seen in the graph of Figure 63. In comparison, weld 12, obtained with the stepped probe design without the increased gap force, was produced without a cavity defect until reaching a length of 80 mm. In direct contrast, the straight probe design used in welds 14 and 11 exceeded the gap size of the welded material before reaching a weld seam length of 20 mm. With all shoulder elements stationary, even an application of a gap force of 2.9 kN could not limit the gap size during to the size of the thickness of the welded sheets.

The additional shoulder in the stepped probe design had an impact on the necessary axial forces during the welding process. The support of the stationary lower shoulder had an effect on the welding process, since the conducted weld 10 is from the behaviour of the gap size in between weld 12 with the same gap force until 95 mm and weld 13 with increased gap force. Yet, the effect is not as strong as seen from the difference of the stepped probe design. This supports the approach of the material flow initiation due to the mass flow $\dot{m}_2$ (Section 5.5.2 and 5.5.3).

The axial forces on the handling system were expected to be low and are ranging in values from -200 N to 200 N. Because the forces in axial direction are in a comparably low region, the reading of the sensors is limited in accuracy.

The forces reached of the different process variants are difficult to compare. Nevertheless, from the results of the experiments it can be suggested that:

- BTs with many active shoulder elements are limited to low speed due to increased radial forces;
- BTs with few active shoulder elements are limited to low speed due to increased axial forces;
- BTs with semi-active shoulder elements are capable of performing high speed and low force welds.

5.6.5 S^{3}BT-SUS and -SLS

During the experiments, failure of probes could not be observed in S^{3}BT-SUS process variant, but in the S^{3}BT-SLS process variant failure of the probe during the experiments were frequent. The total load on the probe is influenced by the loads on the lower shoulder and the loads on the surface of the probe. The loads on the upper shoulder are not affecting the probe directly, since there is no direct mechanical connection between them. Yet, the influence of the upper shoulder on the material influences indirectly the loads on the surface of the probe. The rotating shoulder plasticizes the material and initiates a rotational flow. The probe supports this transportation. At the stationary shoulder side, the material flow and plastification depend on the shear stress of the horizontally discretized layers and the influence of the probe (Section 5.5.4). Without the influence of the rotating shoulder on the stationary side, the probe must induce plastification and rotation of the incoming material in a higher level.

Thus, it can be assumed that the material which is moving because of the rotating shoulder is not applying as much pressure on the probe's surface as the material closer to the stationary shoulder. Therefore, an elevated force opposite to the welding direction on the probe is proposed for the surfaces close to the stationary shoulder side. According to this, the material on the upper side during the S^{3}BT-SLS process applies less force on the probe than the material in vicinity of the stationary lower shoulder. The high force in lower regions of the probe results in high bending, due to the long arm of lever.

During the S^{3}BT-SUS process variant, the material influenced by the rotating shoulder is at the bottom side of the work pieces. Hence, the pressure on the probe is reduced in this region. While at the upper level in the vicinity of the stationary upper shoulder, higher pressure is applied on the probe. This pressure results more in shear stress on the probe, but less in bending, since the arm of lever is small or even close to zero. Torque might be the governing load case in S^{3}BT-SUS.

Additionally, in S^{3}BT-SLS process variant the bending of the probe might be influenced by two other phenomena. First, the necessary tilt angle for the pressure on the RS mentioned in Section 5.2.1. And second, the bending occurring from the friction induced forces on the stationary lower shoulder. This results into a further bending in opposite direction of the welding speed.

The influence of probe's geometry on the bending due to the rotation is significant. The non-rotational symmetry of the featured probe can lead to different surface strain at a constant bending angle over rotational degree. The stiffness of the probe, which depends on the moment of inertia of the cross section, changes according to the rotation degree of the applied loads. During the rotation of the probe from an angle of low stiffness to an angle of high stiffness a peak strain in a thin outer region can be caused, since the bending angle must adapt rapidly to the change of stiffness. This can cause crack initiation and propagation.

6. Conclusions

In the present work, four bobbin tool stationary shoulder process variants have been successfully investigated. The macrostructure and mechanical properties of the processes with acceptable experimental feasibility have been determined and related to the characteristics of the process variant in question. The incoming kinetic energy of the rotating mass flow $\dot{m}_2$ entering the leading side of the weld zone on the advancing side (AS) has been identified as a critical value from the modelling. This value can give an indication of the experimental feasibility of new process variants. Furthermore, the effect of new tool geometries can be evaluated within simulation. In this matter, two new parameters have been introduced. As a first, the relative rotating kinetic energy of the mass flows (R_{Rot}KE) is the relation of the kinetic energy of the mass flow $\dot{m}_2$ entering the leading side and the kinetic energy of the mass flow $\dot{m}_3$ leaving the trailing side on the retreating side (RS). And second, the relative to reference kinetic energy of the mass flows (R_{Ref}KE) is the relation of the kinetic energy of the mass flow $\dot{m}_2$ entering the leading side of one process variant and the same kinetic energy of the mass flow of a referenced process variant. Together, they establish a connection between the behaviour of the material during the experimental research and the feasibility of the process variant.

Discretized Mass Flows and their Kinetic Energies

Processes with high R_{Rot}KEs (approximately >90%) are executable at lower welding speed because the incoming energy is comparable with the outgoing energy and therefore indicates a continuous flow around the probe, if the according R_{Ref}KE indicates that the total mechanical power, wich is the kinetic energy of the mass flow $\dot{m}_2$, is high enough to initiate material flow. Too low R_{Ref}KEs result in challenges of material transport and feasibility of the process during experimental research, as it was the case for the process variant with stationary shoulder bobbin tool (SSBT) with the straight probe design (R_{Ref}KE = 1%). It could be shown that very high R_{Ref}KEs in combination with high R_{Rot}KEs result in high reaction forces during the welding procedure. In case of the conventional self-reacting bobbin tool (SRBT) process variant, it is suggested that these energies lead to oscillating deviation of the welding spindle. Process variants with mid-range R_{Rot}KE are working very stable at high welding speeds and are depending on the R_{Ref}KE values, which rise with the increase of the welding speed. As an example, the semi-stationary shoulder bobbin tool with the stationary upper shoulder (S^3BT-SUS) process variant with mid-range R_{Rot}KE (around 55%) is reaching higher welding speeds (1850 and 2000 mm/min) with a comparable R_{Ref}KE (72% and 88%) to the SRBT with a welding speed of 300 mm/min. This process variant results in the most stable behaviour during the welding. For the S^3BT-SUS, the R_{Rot}KE stays within the range of 49% to 55% at any welding speed conducted in the experiments. The R_{Rot}KE is continuously decreasing with increasing welding speed, while the R_{Ref}KE is increasing in non-linear behaviour. Since the computational fluid dynamics (CFD) model, from which the values originated, was based on the computer aided design of the tool used in the process, there is a wide possibility for further research and improvements of BT-FSW process variants. The kinetic and thermal energy flux transported with the mass flow $\dot{m}_2$ on the AS influence the necessary axial forces of the tool gap, as well as the radial forces on the handling system. The induction of mass flow and, consequently, the volume transported depend on the active shoulder elements of the tool concept and the welding speed. The simulation and the data received from the experimental procedure indicate that tool concepts with a high amount of active shoulder elements lead to the reduction of necessary gap forces, but also to elevated radial forces during experiments. In direct contrast, tool concepts with few active shoulder elements lead to elevated gap forces, but reduced amplitudes in radial forces.

The critical spot has been identified as the region of the stirred zone least influenced by the rotating parts of the tool. This region presents, hence, the least shear induced flow, which is furthest away from the main flow. This spot was observed to be located on the AS of the weld, where the highest effect of the incoming material flow is present. Particularly with respect to these assumptions, the shear induced flow is governing in the process. New tool designs can be adjusted within the CFD simulation according to this knowledge.

The shape of the weld zone is dominated by the material flows on the trailing side of the probe. The pressure from the mass flow $\dot{m}_3$ which is passing through the RS applied on the trailing side of the probe on the AS widens the stirred zone. The region of the collision shifts from the vicinity of the rotating shoulder to mid-thickness level. The influence of the rotating shoulder on the mass flow $\dot{m}_2$ leads to the formation of the weld zone close to the centre of the probe, while at mid-thickness level the mass flow $\dot{m}_2$ is reduced and, therefore, the influence of the incoming rigid material on the AS increases, moving the impulse transfer into the region on the trailing side of the probe.

The results from the COMSOL Multiphysics CFD model correlate to the evaluation of the marker material experiments with X-ray inspection. It was observed that the material originally on the AS travels around the probe passing through the RS and accumulates on the AS again. The material from the RS shows similar behaviour, yet the travelled path is shorter. In a model with divided flow into discrete orbits, the observed patterns in X-ray images could be fully explained. The model originated from the marker material experiments supports the discretization of the flows and the influence of the mass flows in the SZ.

Process development

The welding spindle newly designed in the present study is capable of producing high quality welds with four different BT-FSW process variants. During the process development, the flexibility of the programming has shown great advantages regarding the adaptation to new welding situations and repeatability of welds. Furthermore, the newly developed tool sets functioned well during the welding process and facilitated the disassembly and cleaning process.

S^3BT

The new semi-stationary shoulder bobbin tool (S^3BT) process variants unite the low force advantages of BT-FSW with the high speed capability of the single-sided FSW application. The semi-stationary process variants are superior in speed and stiffness requirement of the handling system to other FSW processes for thin sheet application. During the process development, a welding speed of 3000 mm/min has been achieved, which represents an increase of factor five to the reported values in literature. While increasing the welding speed, the amplitudes of forces have been reduced. Since the mean value of the process forces are in the present range of articulated arm robots, this BT-FSW variant broadens the field of industrial application. The results of the thermo camera, thermal simulation, and hardness[8] measurements support the recorded reduced heat input in comparison to the conventional process variants. Furthermore, the tensile tests with 92% ultimate tensile strength of the base material and bending testing showed good results. In marker material experiments, it has been seen that vertical flow is limited and not necessary for high quality welds. The S^3BT with a stationary lower shoulder has the drawback the complexity of the tool. Especially the bearing supported lower shoulder suffers from elevated temperatures during long welding processes. For the laboratory environment, this configuration works well, yet for industrial application it should be improved. The occurring probe failures are another challenge of the S^3BT process variant with the stationary lower shoulder. It is suggested that excessive bending induces this failure. With the S^3BT including a stationary upper shoulder, the drawbacks of the stationary lower shoulder process variant are not occurring. With the stationary upper shoulder solution, the tool loses the complexity of the supported lower shoulder, but keeps the superior welding abilities.

SSBT

The most challenging process variant to accomplish during the experiments was the SSBT, which consists of two stationary shoulders. Continuously from the first version of the SSBT, it was seen that the several introduced improvements lead to better welding conditions. It was shown that the initiation of a continuous flow around the probe is the key to a stable weld. One approach with experimental feasibility is the SSBT process variant with the stepped probe configuration. In contrast, with the straight probe design the volume of the fluxes are comparably low due to the reduced shear contact channels and additionally the loss of material from the weld zone prevent the consolidation of the weld. The seriousness of this loss can be divided into the amount of energy subtracted from the system and the influence due to cavity defect formation. A loss of material volume from the weld zone cannot be balanced with a smaller gap size. Furthermore, it leads to increased axial forces beyond the capability of the present tool geometry. The idea of the SSBT process variant is to produce colder and more homogeneous welds. The SSBT process variant gives challenges for further research especially since the parametric window of the SSBT process variant showed to be narrower than the S^3BT, which in turn showed to be narrower than the conventional SRBT process variant.

---

[8] Mechanical Testing is found in the Appendix B

Appendix

A. Lists

List of Figures

List of Tables

Bibliography

[1] J. Hilgert, "Knowledge based process development of bobbin tool friction stir welding " PhD Thesis, Helmholtz-Zentrum Geesthacht, Technische Universität Hamburg-Harburg, Geesthacht, 2012.

[2] W. M. Thomas, E. D. Nicholas, J. C. Needham, M. G. Murch, P. Temple-Smith, and C. J. Dawes, "Friction stir welding " Pat. US5460317 A, 1991.

[3] W. M. Thomas, E. D. Nicholas, J. C. Needham, M. G. Murch, P. Templesmith, and C. J. Dawes, "Improvements relating to friction welding " Pat. EP0615480 B1, 1991.

[4] Kuka Roboter GmbH. (2012, 19.02.2015). *KUKA lance une cellule standard de FSW* Available: http://www.kuka.com/nl_media/12/KUKA_fachartikel-fsw-zelle-fr.pdf

[5] Apple Inc. (2015, 19.02.2015). *Seamless design of iMac* Available: https://www.apple.com/imac/design/

[6] P. L. Threadgill, "Section 6 - The future of friction stir welding " in *Friction stir welding: from basics to applications*, D. Lohwasser and Z. Chen, Eds., ed The Welding Institute (TWI), Cambridge, UK: Woodhead Publishing, 2010, pp. 164-182.

[7] Daimler AG, "CAD image of a longitudinal member for integral subframe in a passenger car ", unpublished ed, PT/TVP, 2012.

[8] R. Zettler, "Section 3 - Material deformation and joint formation in friction stir welding " in *Friction stir welding: from basics to applications*, D. Lohwasser and Z. Chen, Eds., ed The Welding Institute (TWI), Cambridge, UK: Woodhead Publishing, 2010, pp. 42-72.

[9] K. J. Colligan, "Section 2 - The friction stir welding process: an overview " in *Friction stir welding: from basics to applications*, D. Lohwasser and Z. Chen, Eds., ed The Welding Institute (TWI), Cambridge, UK: Woodhead Publishing, 2010, pp. 15-41.

[10] G. Völlner, "Rührreibschweißen mit Schwerlast-Industrierobotern " PhD Thesis, Institute für Werkzeugmaschinen und Betriebswissenschaften, Technische Universität München, Herbert Utz Verlag, Müchen, 2010.

[11] Gatwick Technologies Ltd. (2015, 19.02.2015). *Catalogue of friction stir welding machines* Available: http://www.gatwicktechnologies.com/products/friction-welding-machines

[12] W. Arbegast, S. Howard, J. Kellar, G. Stone, M. Langerman, L. Kjerengtroen, *et al.*, "Multi-axis friction stir welding and laser processing at the Advanced Materials Processing Center " presented at the Aeromat 2002: ASM International's 13th Advanced Aerospace Materials and Processes Conference and Exposition, Orlando, FL, USA, 2002.

[13] Helmholtz-Zentrum Geesthacht GmbH. (2015, 19.02.2015). *Scientific and technical infrastructure of the Institute of Materials Mechanics, department of Solid State Joining Processes* Available: http://www.hzg.de/institutes_platforms/materials_research/materials_mechanics/solid_state_joining_processes/techniques/index.php.en

[14] ESAB Holdings Ltd. (2015, 19.02.2015). *ESAB FSW programme* Available: http://www.esab.com/automation/en/products/FSW-programme.cfm

[15] S. Sheikhi, "Herstellung und Bewertung der Umformbarkeit von reibrührgeschweissten tailored blanks aus Aluminiumlegierungen " PhD Thesis, Fakultät für Ingenieurwissenschaften, Maschinenbau und Verfahrenstechnik, Universität Duisburg-Essen, 2006.

[16] R. S. Mishra and M. W. Mahoney, *Friction stir welding and processing* vol. 1. Materials Park, OH, USA: ASM International, 2007.

[17] C. B. Smith, "Robotic friction stir welding using a standard industrial robot " *Kei Kinzoku Yosetsu (Journal of Light Metal Welding and Construction),* vol. 42, pp. 40-41, 2004.

[18] ESAB Holdings Ltd. (2011, 19.02.2015). *ESAB Rosio friction stir welding robot* Available: http://www.esab.com/

[19] N. Mendes, P. Neto, and A. Loureiro, "Robotic friction stir welding aided by hybrid force / motion control " in *proceedings of Emerging Technology and Factory Automation (ETFA)*, 2014, pp. 1-4.

[20] H. Wu, Y. C. Chen, D. Strong, and P. Prangnell, "Systematic evaluation of the advantages of static shoulder FSW for joining aluminium " *Materials Science Forum,* vol. 794-796, pp. 407-412, 2014.

[21] S. Ji, X. Meng, L. Ma, H. Lu, and S. Gao, "Vertical compensation friction stir welding assisted by external stationary shoulder " *Materials & Design,* vol. 68, pp. 72-79, 2015.

[22] B. T. Gibson, D. H. Lammlein, T. J. Prater, W. R. Longhurst, C. D. Cox, M. C. Ballun, *et al.*, "Friction stir welding: process, automation, and control " *Journal of Manufacturing Processes,* vol. 16, pp. 56-73, 2014.

[23] P. S. Davies, B. P. Wynne, W. M. Rainforth, M. J. Thomas, and P. L. Threadgill, "Development of microstructure and crystallographic texture during stationary shoulder friction stir welding of Ti-6Al-4V " *Metallurgical and Materials Transactions A,* vol. 42, pp. 2278-2289, 2011.

[24] H. J. Liu, J. Q. Li, and W. J. Duan, "Friction stir welding characteristics of 2219-T6 aluminum alloy assisted by external non-rotational shoulder " *The International Journal of Advanced Manufacturing Technology,* vol. 64, pp. 1685-1694, 2013.

[25] M. M. Z. Ahmed, B. P. Wynne, W. M. Rainforth, and P. L. Threadgill, "Through-thickness crystallographic texture of stationary shoulder friction stir welded aluminium " *Scripta Materialia,* vol. 64, pp. 45-48, 2011.

[26] Grenzebach Maschinenbau GmbH. (2012, 19.02.2015). *Produkt Vorstellung* Available: http://www.grenzebach.com/index.php/grenzebach/technologien/sonderanwendungen/ruehr_reibschweissen

[27] H. Wu, Y. C. Chen, D. Strong, and P. Prangnell, "Assessment of the advantages of static shoulder FSW for joining aluminium aerospace alloys " *Materials Science Forum,* vol. 783-786, pp. 1770-1775, 2014.

[28] S. D. Ji, X. C. Meng, J. G. Liu, L. G. Zhang, and S. S. Gao, "Formation and mechanical properties of stationary shoulder friction stir welded 6005A-T6 aluminum alloy " *Materials & Design,* vol. 62, pp. 113-117, 2014.

[29] J. Hilgert, H. N. B. Schmidt, J. F. Dos Santos, and N. Huber, "Thermal models for bobbin tool friction stir welding " *Journal of Materials Processing Technology,* vol. 211, pp. 197-204, 2011.

[30] J. Hilgert, H. Schmidt, and J. F. Dos Santos, "Bobbin tool FSW - a moving geometry model " presented at the COMSOL Conference 2009, Boston, USA, 2009.

[31] J. Hilgert, L. L. Hütsch, J. F. Dos Santos, and N. Huber, "Material flow around a bobbin tool for friction stir welding " presented at the COMSOL Conference 2010, Paris, France, 2010.

[32] J. Hilgert and J. F. dos Santos, "Vorrichtung zum Reibrührschweißen " Pat. DE102011015831 B3, 2011.

[33] J. Hilgert, J. F. Dos Santos, and N. Huber, "Numerical simulation in bobbin tool FSW process development " presented at the 9th International Symposium on Friction Stir Welding, The Welding Institute (TWI), Cambridge, UK, 2012.

[34] J. Hilgert, J. F. Dos Santos, and N. Huber, "Shear layer modelling for bobbin tool friction stir welding " *Science and Technology of Welding and Joining,* vol. 17, pp. 454-459, 2012.

[35] W. Y. Li, T. Fu, L. Hütsch, J. Hilgert, F. F. Wang, J. F. dos Santos, *et al.*, "Effects of tool rotational and welding speed on microstructure and mechanical properties of bobbin tool friction stir welded Mg AZ31 " *Materials & Design,* vol. 64, pp. 714-720, 2014.

[36] T. P. Neumann, "Friction stir welding of Al 2024-T351 using a self-reacting bobbin tool " PhD Thesis, Fakultät Maschinenbau, Technsiche Universität Ilmenau, Verelagshaus Mainz GmbH, Aachen, 2009.

[37] M. Skinner and R. L. Edwards, "Improvements to the FSW process using the self-reacting technology " in *proceedings of THERMEC 2003*, Madrid, Spain, 2003, pp. 2849-2854

[38] K. Tamashiro, M. Kamai, Y. Morisada, and H. Fujii, "Miniaturization of FSW equipment using counterbalanced tool concept " in *proceedings of the 1st International Joint Symposium on Joining and Welding*, 2013, pp. 155-157.

[39] M. K. Sued, D. Pons, J. Lavroff, and E. H. Wong, "Design features for bobbin friction stir welding tools: development of a conceptual model linking the underlying physics to the production process " *Materials & Design,* vol. 54, pp. 632-643, 2014.

[40] K. Okamoto, A. Sato, S. H. C. Park, and S. Hirano, "Microstructure and mechanical properties of friction stir welded aluminum extrusion with bobbin tools " *Materials Science Forum,* vol. 706-709, pp. 990-995, 2012.

[41] S. J. Chen, A. L. Lu, D. L. Yang, S. Lu, J. H. Dong, and C. L. Dong, "Analysis on flow pattern of bobbin tool friction stir welding for 6082 aluminum " in *proceedings of the 1st International Joint Symposium on Joining and Welding*, H. Fujii, Ed., ed: Woodhead Publishing, 2013, pp. 353-358.

[42] H. W. Zhang, M. Wang, X. Zhang, and G. Yang, "Microstructural characteristics and mechanical properties of bobbin tool friction stir welded 2A14-T6 aluminum alloy " *Materials & Design,* vol. 65, pp. 559-566, 2015.

[43] X. M. Liu, J. S. Yao, Y. Cai, H. Meng, and Z. D. Zou, "Simulation on the temperature field of bobbin tool friction stir welding of AA 2014 aluminium alloy " *Applied Mechanics and Materials,* vol. 433-435, pp. 2091-2095, 2013.

[44] L. Wan, Y. Huang, Z. Lv, S. Lv, and J. Feng, "Effect of self-support friction stir welding on microstructure and microhardness of 6082-T6 aluminum alloy joint " *Materials & Design,* vol. 55, pp. 197-203, 2014.

[45] L. Wan, Y. Huang, W. Guo, S. Lv, and J. Feng, "Mechanical properties and microstructure of 6082-T6 aluminum alloy joints by self-support friction stir welding " *Journal of Materials Science & Technology,* vol. 30, pp. 1243-1250, 2014.

[46] J. Schneider, A. C. Nunes Jr, and M. S. Brendel, "The influence of friction stir weld tool form and welding parameters on weld structure and properties: nugget bulge in self-reacting friction stir welds " presented at the 8th International Friction Stir Welding Symposium, Timmendorfer Strand, Germany, 2010.

[47] P. L. Threadgill, M. M. Z. Ahmed, J. P. Martin, J. G. Perrett, and B. P. Wynne, "The use of bobbin tools for friction stir welding of aluminium alloys " in *Materials Science Forum*, 2010, pp. 1179-1184.

[48] K. R. Horton, "Microhardness, strength and strain field characterization of self-reacting friction stir and plug welds of dissimilar aluminum alloys " PhD Thesis, Department of Interdisciplinary Studies, The University of Alabama, Tuscaloosa, Alabama, USA, 2011.

[49] T. Zappia, C. Smith, K. Colligan, H. Ostersehlte, and S. W. Kallee, "Section 4 - Friction stir welding equipment " in *Friction stir welding: from basics to applications*, D. Lohwasser and Z. Chen, Eds., ed The Welding Institute (TWI), Cambridge, UK: Woodhead Publishing, 2010, pp. 73-117.

[50] H. Atharifar, D. Lin, and R. Kovacevic, "Numerical and experimental investigations on the loads carried by the tool during friction stir welding " *Journal of Materials Engineering and Performance,* vol. 18, pp. 339-350, 2009.

[51] K. Krasnowski, C. Hamilton, and S. Dymek, "Influence of the tool shape and weld configuration on microstructure and mechanical properties of the Al 6082 alloy FSW joints " *Archives of Civil and Mechanical Engineering,* 2014.

[52] A. Steuwer, M. J. Peel, and P. J. Withers, "Dissimilar friction stir welds in AA5083–AA6082: The effect of process parameters on residual stress " *Materials Science and Engineering: A,* vol. 441, pp. 187-196, 2006.

[53] T. Jene, G. Dobmann, G. Wagner, and D. Eifler, "Oxide Fragments in Friction Stir Welds – Distribution and Effects on Crack Initiation " presented at the 6th Symposium in Friction Stir Welding, Saint Sauveur, Canada, 2006.

[54] J. P. Wulfsberg and H. Loitz, "Prozesssicherheit beim robotergestützen Rührreibschweißen ", ed: Laboratorium Fertigungstechnik, Helmut Schmidt Universität Hamburg, 2009.

[55] J. Wulfsberg, H. Loitz, and J. F. dos Santos, "Roboterreibrührschweißen. Roboterbasierte Anlagentechnik zum Fügen durch Reibrührschweißen " *Werkstattstechnik online,* vol. 94, pp. 462-466, 2004.

[56] J. P. Wulfsberg, H. Loitz, and J. F. dos Santos, "Robotergestütztes Reibrührschweißen " *VDI-Berichte 1841, Beitrag Robotik,* 2004.

[57] H. J. Liu, J. C. Hou, and H. Guo, "Effect of welding speed on microstructure and mechanical properties of self-reacting friction stir welded 6061-T6 aluminum alloy " *Materials & Design,* vol. 50, pp. 872-878, 2013.

[58] J. Chen, H. Fujii, Y. Sun, Y. Morisada, and K. Kondoh, "Effect of material flow by double-sided friction stir welding on weld structure and mechanical properties of magnesium alloy " in *proceedings of the 9th International Symposium on Friction Stir Welding*, The Welding Institute (TWI), Cambridge, UK, 2012, pp. 451-456.

[59] W. M. Thomas, C. S. Wiesner, D. J. Marks, and D. G. Staines, "Conventional and bobbin friction stir welding of 12% chromium alloy steel using composite refractory tool materials " *Science and Technology of Welding & Joining,* vol. 14, pp. 247-253, 2009.

[60] International Organization for Standardization (ISO), "Friction stir welding -aluminium- " in *International Sandard ISO 25239-1 to -5* vol. ISO 25239:2011, ed. Switzerland: ISO, 2011.

[61] T. Suda, Y. Sakamoto, T. Miyamichi, and T. Sato, "A feasibility study for stationary shoulder self-reacting pin tool welding " in *Proceedings of the 9th international symposium on friction stir welding,* Huntsville, Alabama, 2012, pp. 257-266.

[62] S. H. C. Park, S. Hirano, S. Kaga, M. Onose, N. Tominaga, and Y. Yoshimura, "Development of Tatsumaki friction stir welding " in *proceedings of Friction Stir Welding and Processing VI*, San Diego, California, USA, 2011, pp. 139-146.

[63] K. N. Krishnan, "On the formation of onion rings in friction stir welds " *Materials Science and Engineering: A*, vol. 327, pp. 246-251, 2002.

[64] Z. W. Chen and S. Cui, "On the forming mechanism of banded structures in aluminium alloy friction stir welds " *Scripta Materialia*, vol. 58, pp. 417-420, 2008.

[65] K. Colligan, "Material flow behavior during friction stir welding of aluminum " *Welding Journal*, pp. 229-237, 1999.

[66] K. J. Colligan and S. Chopra, "Examination of material flow in friction stir welding of aluminum using stop action technique " presented at the 5th International Symposium on Friction Stir Welding, Metz, France, 2004.

[67] K. Colligan, "Dynamic material deformation during friction stir welding of aluminum " presented at the 1st International Symposium on Friction Stir Welding, Thousand Oaks, CA, USA, 1999.

[68] W. J. Arbegast, "A flow-partitioned deformation zone model for defect formation during friction stir welding " *Scripta Materialia*, vol. 58, pp. 372-376, 2008.

[69] R. Zettler, S. Lomolino, J. F. dos Santos, and D. Lohwasser, "Effect of tool geometry and process parameters on material flow in FSW of aluminum alloys " presented at the 2nd FSW Modelling and Flow Visualisation Seminar, Geesthacht, Germany, 2005.

[70] R. Zettler, T. Donath, J. F. dos Santos, F. Beckman, and D. Lohwasser, "Validation of marker material flow in 4mm thick friction stir welded Al 2024-T351 through computer microtomography and dedicated metallographic techniques " *Advanced Engineering Materials*, vol. 8, pp. 487-490, 2006.

[71] M. Guerra, C. Schmidt, J. C. McClure, L. E. Murr, and A. C. Nunes, "Flow patterns during friction stir welding " *Materials Characterization*, vol. 49, pp. 95-101, 2002.

[72] A. P. Reynolds, "Flow visualization and simulation in FSW " *Scripta Materialia*, vol. 58, pp. 338-342, 2008.

[73] T. U. Seidel, "The development of a friction stir welding process model using computational fluid dynamics " PhD Thesis, Department of Mechanical Engineering, University of South Carolina, 2002.

[74] H. B. Schmidt, T. L. Dickerson, and J. H. Hattel, "Material flow in butt friction stir welds in AA2024-T3 " *Acta Materialia*, vol. 54, pp. 1199-1209, 2006.

[75] H. B. Schmidt and J. Hattel, "Material flow in friction stir welding – investigation of the shear layer " *Mathematical Modelling of Weld Phenomena,* vol. 8, 2006.

[76] Z. W. Chen, T. Pasang, Y. Qi, and R. Perris, "Tool-workpiece interface and shear layer formed during friction stir welding " presented at the 6th Symposium in Friction Stir Welding, Saint Sauveur, Canada, 2006.

[77] Z. W. Chen, T. Pasang, and Y. Qi, "Shear flow and formation of nugget zone during friction stir welding of aluminium alloy 5083-O " *Materials Science and Engineering: A,* vol. 474, pp. 312-316, 2008.

[78] Z. W. Chen and R. Maginness, "Formation of weld zones during friction stir welding of aluminum alloys " presented at the 5th International Symposium on Friction Stir Welding, Metz, France, 2004.

[79] O. Lorrain, V. Favier, H. Zahrouni, and D. Lawrjaniec, "Understanding the material flow path of friction stir welding process using unthreaded tools " *Journal of Materials Processing Technology,* vol. 210, pp. 603-609, 2010.

[80] P. Dong, F. Lu, J. K. Hong, and Z. Cao, "Coupled thermomechanical analysis of friction stir welding process using simplified models " *Science and Technology of Welding and Joining,* vol. 6, pp. 281-287, 2001.

[81] F. Al-Badour, N. Merah, A. Shuaib, and A. Bazoune, "Coupled Eulerian Lagrangian finite element modeling of friction stir welding processes " *Journal of Materials Processing Technology,* vol. 213, pp. 1433-1439, 2013.

[82] A. Arora, R. Nandan, A. P. Reynolds, and T. DebRoy, "Torque, power requirement and stir zone geometry in friction stir welding through modeling and experiments " *Scripta Materialia,* vol. 60, pp. 13-16, 2009.

[83] N. S. binti Sataruddin, M. Awang, and K. Z. K. Shaari, "Material flow study during friction stir welding process using computational fluid dynamics simulation " presented at the National Postgraduate Conference (NPC), 2011.

[84] A. Arora, Z. Zhang, A. De, and T. DebRoy, "Strains and strain rates during friction stir welding " *Scripta Materialia,* vol. 61, pp. 863-866, 2009.

[85] H. Schmidt and J. Hattel, "CFD modelling of the shear layer around the tool probe in friction stir welding " presented at the Friction Stir Welding and Processing III, San Francisco, California, USA, 2005.

[86] Z. Zhang, "Comparison of two contact models in the simulation of friction stir welding process " *Journal of Materials Science,* vol. 43, pp. 5867-5877, 2008.

[87] H. W. Zhang, Z. Zhang, and J. T. Chen, "The finite element simulation of the friction stir welding process " *Materials Science and Engineering: A,* vol. 403, pp. 340-348, 2005.

[88] Z. Zhang and H. W. Zhang, "Numerical studies on controlling of process parameters in friction stir welding " *Journal of Materials Processing Technology,* vol. 209, pp. 241-270, 2009.

[89] X. Deng and S. Xu, "Two-dimensional finite element simulation of material flow in the friction stir welding process " *Journal of Manufacturing Processes,* vol. 6, pp. 125-133, 2004.

[90] S. Xu, X. Deng, A. P. Reynolds, and T. U. Seidel, "Finite element simulation of material flow in friction stir welding " *Science and Technology of Welding & Joining,* vol. 6, pp. 191-193, 2001.

[91] Z. Zhang and H. W. Zhang, "A fully coupled thermo-mechanical model of friction stir welding " *The International Journal of Advanced Manufacturing Technology,* vol. 37, pp. 279-293, 2008.

[92] J. Zhang, Y. Shen, B. Li, H. Xu, X. Yao, B. Kuang, *et al.*, "Numerical simulation and experimental investigation on friction stir welding of 6061-T6 aluminum alloy " *Materials & Design,* vol. 60, pp. 94-101, 2014.

[93] P. A. Colegrove and H. R. Shercliff, "3-Dimensional CFD modelling of flow round a threaded friction stir welding tool profile " *Journal of Materials Processing Technology,* vol. 169, pp. 320-327, 2005.

[94] L. Shi, C. S. Wu, and M. A. Chen, "Numerical analysis of heat transfer and material flow in reverse dual-rotation friction stir welding " in *Proceedings of the 1st International Joint Symposium on Joining and Welding,* H. Fujii, Ed., ed: Woodhead Publishing, 2013, pp. 325-331.

[95] H. B. Schmidt and J. H. Hattel, "Thermal and material flow modelling of friction stir welding using Comsol " presented at the COMSOL Conference, Hannover, Germany, 2008.

[96] Z. Zhang and J. T. Chen, "The simulation of material behaviors in friction stir welding process by using rate-dependent constitutive model " *Journal of Materials Science,* vol. 43, pp. 222–232, 2008.

[97] P. A. Colegrove and H. R. Shercliff, "CFD modelling of friction stir welding of thick plate 7449 aluminium alloy " *Science and Technology of Welding & Joining,* vol. 11, pp. 429-441, 2006.

[98] H. W. Zhang, Z. Zhang, and J. T. Chen, "3D modeling of material flow in friction stir welding under different process parameters " *Journal of Materials Processing Technology,* vol. 183, pp. 62-70, 2007.

[99] H. W. Zhang, Z. Zhang, and J. T. Chen, "Corrigendum to “3D modeling of material flow in friction stir welding under different process parameters” " *Journal of Materials Processing Technology,* vol. 199, p. 456, 2008.

[100] H. Pashazadeh, J. Teimournezhad, and A. Masoumi, "Numerical investigation on the mechanical, thermal, metallurgical and material flow characteristics in friction stir welding of copper sheets with experimental verification " *Materials & Design,* vol. 55, pp. 619-632, 2014.

[101] Z. Zhang and H. W. Zhang, "Numerical studies on the effect of transverse speed in friction stir welding " *Materials & Design,* vol. 30, pp. 900-907, 2009.

[102] Z. Zhang and H. W. Zhang, "Material behaviors and mechanical features in friction stir welding process " *The International Journal of Advanced Manufacturing Technology,* vol. 35, pp. 86-100, 2007.

[103] T. Sheppard, "Extrusion of AA2024 Alloy " *Materials Science and Technology,* vol. 9, pp. 430-440, 1993.

[104] T. Sheppard and A. Jackson, "Constitutive equations for use in prediction of flow stress during extrusion of aluminium alloys " *Materials Science and Technology,* vol. 13, pp. 203-209, 1997.

[105] T. Sheppard and D. S. Wright, "Determination of flow-stress part 1: constitutive equation for aluminium-alloys at elevated temperature " *Metal Technology,* vol. 6, pp. 215–223, 1979.

[106] F. Miyasaka, G. Yoshikawa, and S. Matsuzawa, "Development of mathematical modeling for FSW with particle method " in *Proceedings of the 1st International Joint Symposium on Joining and Welding,* Osaka, Japan, 2013, pp. 287-290.

[107] T. Aukrust and S. LaZghab, "Thin shear boundary layers in flow of hot aluminium " *International Journal of Plasticity,* vol. 16, pp. 59-71, 2000.

[108] S. Spigarelli, E. Evangelista, and H. J. McQueen, "Study of hot workability of a heat treated AA6082 aluminum alloy " *Scripta Materialia,* vol. 49, pp. 179-183, 2003.

[109] A. Albers, S. Matthiesen, and G. Lechner, "Konstruktionsmethodisches Grundmodell zum Zusammenhang von Gestalt und Funktion technischer Systeme " *Konstruktion,* pp. 55-60, 2002.

[110] S. Matthiesen, "Ein Beitrag zur Basisdefinition des Elementmodells "Wirkflächenpaare & Leitstützstrukturen" zum Zusammenhang von Funktion und Gestalt technischer Systeme " PhD Thesis, Institut für Maschinenkonstruktionslehre und Kraftfahrzeugbau, Universität Karlsruhe (TH), Karlsruhe, 2002.

[111] H. S. Patil and S. N. Soman, "Experimental study on the effect of welding speed and tool pin profiles on AA6082-O aluminium friction stir welded butt joints " *International Journal of Engineering, Science and Technology,* vol. 2, pp. 268-275, 2010.

[112] P. Cavaliere, A. Squillace, and F. Panella, "Effect of welding parameters on mechanical and microstructural properties of AA6082 joints produced by friction stir welding " *Journal of Materials Processing Technology,* vol. 200, pp. 364-372, 2008.

[113] M. Cabibbo, A. Forcellese, M. El Mehtedi, and M. Simoncini, "Double side friction stir welding of AA6082 sheets: microstructure and nanoindentation characterization " *Materials Science and Engineering: A,* vol. 590, pp. 209-217, 2014.

[114] B. Zhang and T. N. Baker, "Effect of the heat treatment on the hot deformation behaviour of AA6082 alloy " *Journal of Materials Processing Technology,* vol. 153–154, pp. 881-885, 2004.

[115] C. Kammer, *Aluminium Taschenbuch, Band 1: Grundlagen und Werkstoffe* vol. 15. Düsseldorf: Aluminium-Verlag, 1995.

[116] C. Kammer, *Aluminium Taschenbuch, Band 3: Weiterverarbeitung und Anwendung* vol. 16. Düsseldorf: Aluminium-Verlag, 2011.

[117] AMAG Rolling GmbH, "AA6082-T4 Abnahmeprüfzeugnis Inspection certificate 3.1 (EN 10204) " 2014.

[118] O. Midling, L. Oosterkamp, and J. Bersaas, *Joints in aluminium, Proceedings of INALCO '98 the 7th International Conference* The Welding Institute (TWI), Cambridge, UK: Woodhead Publishing, 1998.

[119] J. Backlund, A. Norlin, and A. Anderson, "Friction stir welding - weld properties and manufacturing techniques " presented at the 7th International Conference Joints in Aluminum, The Welding Institute (TWI), Cambridge, UK, 1998.

[120] K. J. Colligan, J. Xu, and J. R. Pickensm, "Welding tool and process parameters effects in FSW of aluminium alloys " in *Proceedings of Friction Stir Welding and Processing II*, 2003, pp. 181-190.

[121] P. A. Colegrove and H. R. Shercliff, "Experimental and numerical analysis of aluminum alloy 7075-T7351 friction stir welds " *Science and Technology of Welding and Joining,* vol. 8, pp. 360-368, 2003.

[122] S. P. Vaze, J. Xu, R. J. Ritter, K. J. Colligan, J. J. J. Fisher, and J. R. Picken, "Friction stir processing of aluminum alloy 5083 plate for cold bending " *Material & Science Forum,* vol. 426-432, pp. 2979-2986, 2003.

[123] F. R. Morral, *Wrought superalloys, properties and selection: stainless steels, tool materials, and special pourpose metals* 9th ed. vol. 3. Metals Handbook: American Society for Metals, 1980.

[124] Timken Latrobe Steel. (1986, 19.02.2015). *MP159 data sheet* Available: http://www.bti-2xl.com/_Uploads/dbsAttachedFiles/MP159.pdf

[125] F. C. Hagan, H. W. Antes, M. D. Boldy, and J. S. Slaney, "Mechanical properties of a new higher-temperature multiphase superalloy " The Minerals, Metals & Materials Society (TMS), Latrobe, PA, USA, 1984.

[126] Uddehom GmbH. (2014, 19.02.2015). *Uddehom Hotvar properties* Available: http://www.uddeholm.com/files/hotvar-english.pdf

[127] O. T. Midling and G. Rørvik, "Effect of tool shoulder material on heat input during friction stir welding " presented at the 1st International Symposium on Friction Stir Welding, Thousand Oaks, CA, USA, 1999.

[128] A. P. Reynolds, "Visualisation of material flow in autogenous friction stir welds " *Science and Technology of Welding and Joining,* vol. 5, pp. 120-124, 2000.

[129] A. M. El-Batahgy, B. Terad, and A. Omar, "Effect of friction stir welding parameters on properties of AA6061 aluminum alloy butt welded joints " in *proceedings of the 1st International Joint Symposium on Joining and Welding*, Osaka, Japan, 2013, pp. 33-40.

[130] COMSOL AG, "CFD Module User´s Guide ", ed. Version 4.4 of Comsol Multiphysics Software, 2013.

[131] COMSOL AG, "Introduction to CFD Module ", ed. Version 4.4 of Comsol Multiphysics Software, 2013.

[132] W. M. Thomas, K. I. Johnson, and C. S. Wiesner, "Friction stir welding – recent developments in tool and process technologies " *Advanced Engineering Materials,* vol. 5, pp. 485-490, 2003.

[133] H. B. Schmidt, "Modelling the thermomechanical conditions in friction stir welding " PhD Thesis, Department of Manufacturing Engineering and Management, Technical University of Denmark, Lyngby, Denmark, 2004.

[134] T. R. McNelley, S. Swaminathan, and J. Q. Su, "Recrystallization mechanisms during friction stir welding/processing of aluminum alloys " *Scripta Materialia,* vol. 58, pp. 349-354, 2008.

[135] T. R. McNelley, K. Oh-ishi, and A. P. Zhilyaev, "Microstructure evolution and microstructure-property relationships in friction stir processing of NiAl bronze " *Materials Science Forum,* vol. 539, pp. 3745-3750, 2007.

[136] A. Askari, S. Silling, B. London, and M. Mahoney, "Modeling and analysis of friction stir welding processes " in *proceedings of Friction Stir Welding and Processing*, Warrendale, USA, 2001, pp. 43–54.

[137] P. Heurtier, C. Desrayaud, and F. Montheillet, "A thermomechanical analysis of the friction stir welding process " *Materials Science Forum,* vol. 396, pp. 1537-1542, 2002.

[138] P. Heurtier, M. Jones, C. Desrayaud, J. H. Driver, F. Montheillet, and D. Allehaux, "Mechanical and thermal modelling of friction stir welding " *Journal of Materials Processing Technology,* vol. 171, pp. 348-357, 2006.

[139] H. J. McQueen, "Elevated-temperature deformation at forming rates of 10^−2 to 10^2 s-1 " *Metallurgical and Materials Transactions A,* vol. 33, pp. 345-362, 2002.

[140] H. B. Schmidt and J. H. Hattel, "Thermal modelling of friction stir welding " *Scripta Materialia,* vol. 58, pp. 332-337, 2008.

[141] H. Schmidt, J. Hattel, and J. Wert, "An analytical model for the heat generation in friction stir welding " *Modelling and Simulation in Materials Science and Engineering,* vol. 12, p. 143, 2004.

[142] H. Schmidt and J. Hattel, "Modelling heat flow around tool probe in friction stir welding " *Science and Technology of Welding & Joining,* vol. 10, pp. 176-186, 2005.

[143] A. Malcherek, "Scribtum Hydromechanik für Bauingenieure ", ed. Institut für Wasserwesen, Fakultät für Bauingenieur- und Vermessungswesen Universität BW München, 2014, p. 435.

[144] K. Kumar and S. V. Kailas, "The role of friction stir welding tool on material flow and weld formation " *Materials Science and Engineering: A,* vol. 485, pp. 367-374, 2008.

[145] Technische Komitee CEN/TC 121, "DIN EN ISO: 4136:2011.05 Querzugversuch " in *3.10 Zerstörende Prüfung,* ed. B-1050 Brüssel: CEN Europäisches Komitee für Normung, 2011.

[146] International Organization for Standardization (ISO), "Metallic materials - Tensile testing - Part 1: Method of test at room temperature (ISO 6892-1:2009); German version EN ISO 6892-1:2009 ", ed: ISO/TC 164/SC 1, 2009.

[147] Normausschuss Schweißtechnik (NAS), DIN Deutsches Institut für Normung e.V., "Zerstörende Prüfungen von Schweißnähten an metallischen Werkstoffen – Biegeprüfungen (ISO 5173:2009); Deutsche Fassung EN ISO 5173:2010 ", ed. Berlin: Beuth Verlag GmbH, 2010.

B. Mechanical Testing

The welds produced during the present study were tested to evaluate the mechanical properties. Tensile and bending tests, as well as hardness measurements were conducted.

Tensile

Tensile tests at HZG were done according to norm DIN EN ISO: 4136:2011.05. In this norm the dimension of the specimens are defined as a function of the welded sheet thickness [145]. The technical drawing of a specimen is presented in Figure B.1 (a). Tests for the Daimler AG were conducted according to the standard of DIN ISO 6892-1:2009 B [146]. The examination was proceeded on weld 6 of Table 5, which is a S^{3}BT process variant with a stationary upper shoulder with 1850 mm/min welding speed. The size of the tensile testing specimen was reduced in comparison to the standard DIN EN 4136. The technical drawing is presented in Figure B.1 (b).

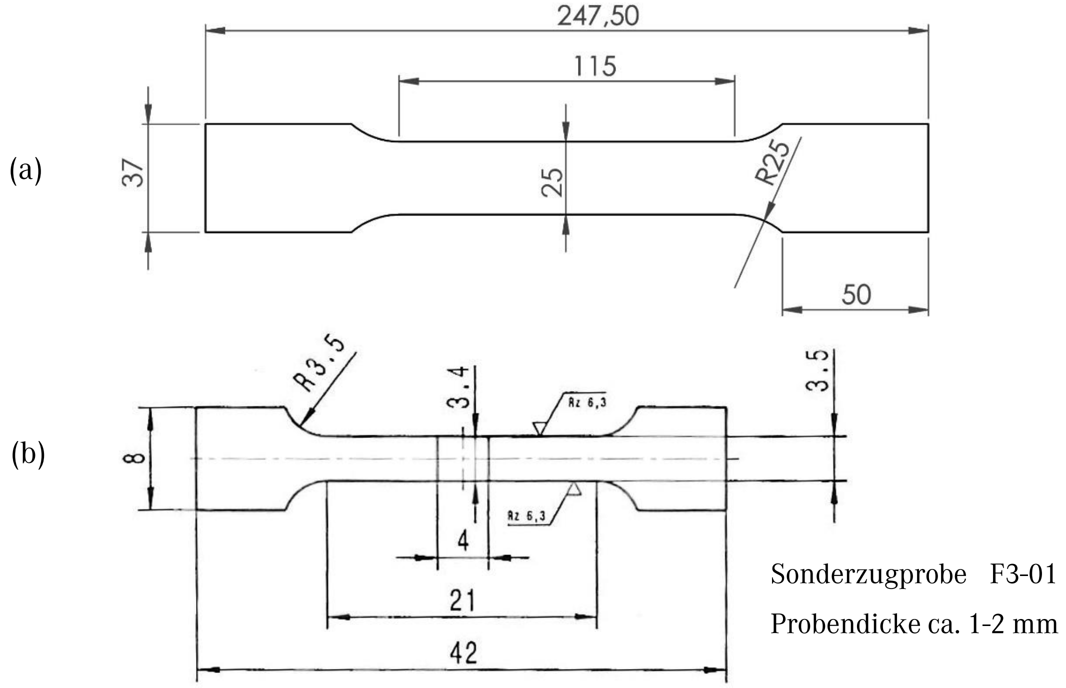

Sonderzugprobe F3-01
Probendicke ca. 1-2 mm

Figure B.1. Technical drawings of tensile test specimens with dimensions in mm, according to (a) DIN 4136 and (b) DIN ISO 6892-1.

The strain rate of the test was 1 mm/min, with a preload of 100 N and the strain was evaluated by an extensimeter with a size of 50 mm. Tensile tests were conducted on the welds and on the base material under different conditions. Five samples of base material were tested, as well as three specimens for each process variant. The welds were conducted on 3.0 mm work pieces except for the S^{3}BT-SLS process variant with a material thickness of 3.6 mm. A list of the tested welds is seen in Table B.1. All tested welds of the new process variant S^{3}BT-SUS are above the value of the conventional SRBT process variant. In Figure B.2, example graphs of stress-strain behaviour are given for the S^3BT-SUS process variant with a welding speed of 2950 mm/min. The specimen 1 and 3 show a very comparable behaviour. Specimen 2 failed before reaching the strain rate of samples 1 and 3, but reached an ultimate tensile strength R_m above 95% of base material. In comparison to the conventional SRBT process variant the S^3BT-SUS with the welding speed of 2950 mm/min could improve in average the ultimate yield tensile strength $R_{p0.2}$ by 13.2 % and the R_m by 11.6 %. The measured strain $\mathbf{A_g}$ appears to have reduced by numbers after the welding process. Yet, the base material has a global strain applied to the sample, since the microstructure is more homogeneous than the microstructure of the weld. The strain on the welded specimens applies locally and therefore the total amount of strain is reduced.

Table B.1. Results of tensile tested welds according to DIN EN ISO: 4136:2011.05

Process variant & welding speed [mm/min]		**$R_{p0.2}$ [MPa]**	**% BM**	**R_m [MPa]**	**% BM**	**A_g [%]**
Base Material	-	160 ± 2	100%	262 ± 3	100%	29 ± 1
SRBT	300	126 ± 6	79%	211 ± 13	81%	12 ± 2
S^3BT-SLS	1800	142 ± 3	89%	237 ± 2	90%	12 ± 1
S^3BT-SUS	2000	134 ± 9	84%	228 ± 10	87%	16 ± 0
S^3BT-SUS	2500	139 ± 4	87%	231 ± 4	88%	15 ± 5
S^3BT-SUS	2950	147 ± 5	92%	241 ± 7	92%	13 ± 1

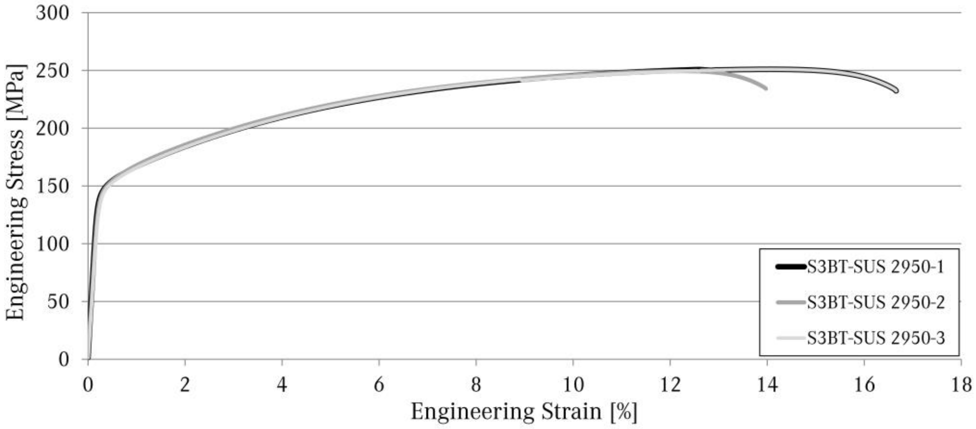

Figure B.2. Results of tensile tests of S^3BT-SUS welds with a welding speed of 2950 mm/min.

The dimensions of the tensile testing specimen according to DIN ISO 6892-1:2009 B allowed to test in different zones of the weld. The tests were performed longitudinal to the weld seam in the SZ, the TMAZ on the RS and AS. Additionally, testing of the welded work pieces were conducted on RS and AS. For each zone 3 tests were proceeded. The results are given in Figure B.3 and Table B.2.

In Figure B.3 it can be observed that the tensile tested samples failed with a similar behaviour. This behaviour is also shown in Table B.2, where the ultimate tensile strength varies in between 253 [MPa] and 265 [MPa] in all examined areas of the weld. The efficiency of the weld is in a high region of 93%

to 95% according to the ultimate tensile strength R_m. One specimen from the TMAZ on the AS reached 97% R_m.

Table B.2. Results from tensile tests with small specimens

Location	$R_{p0.2}$ [MPa]	% BM	R_m [MPa]	% BM	A_g [%]	% BM
BM AS	167 ± 0	100%	273 ± 1,2	100%	15 ± 0	100%
BM RS	166 ± 0	100%	274 ± 0	100%	15 ± 0	100%
SZ	154 ± 1	92%	256 ± 2	94%	16 ± 1	105%
TMAZ AS	156 ± 4	93%	260 ± 6	95%	15 ± 1	100%
TMAZ RS	152 ± 1	92%	255 ± 2	93%	15 ± 0	99%

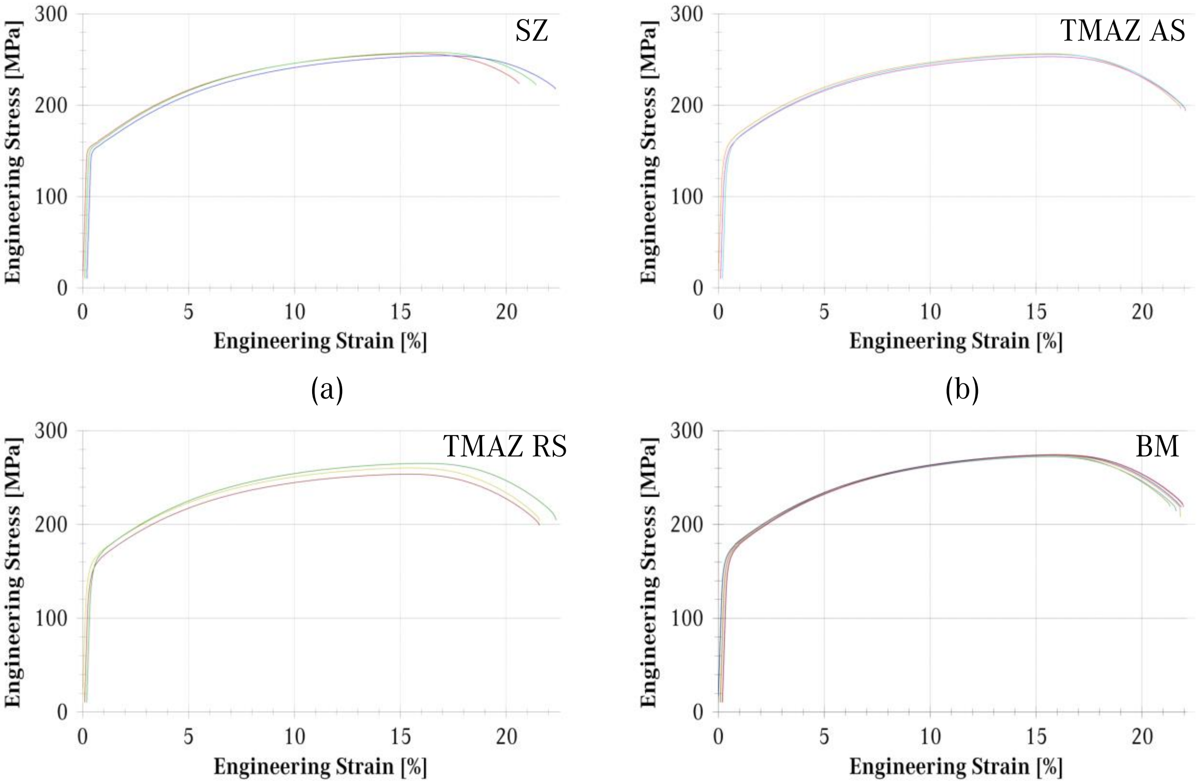

(a) (b) (c) (d)

Figure B.3. Results of longitudinal tensile tests of weld 6 obtained with S^3BT-SUS process variant.Three specimens were taken for each location: (a) SZ, (b) TMAZ on the AS and (c) TMAZ on the RS. (d) Six specimens of the BM, three from the work piece on the RS and 3 from the work piece on the AS, were also tested.

Bending

Bending tests were conducted on the welded specimens according to the norm DIN EN ISO 5173:2009 [147]. The norm specifies for a weld seam width of 15 mm to use 20 mm width specimens, a diameter of the bending rod of 12 mm over a distance of 22 mm. Tests were conducted from both sides of the welded specimens.

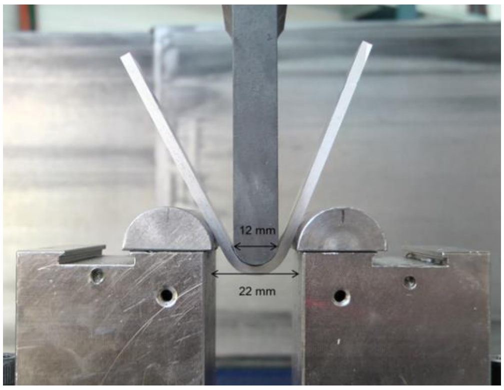

Figure B.4. Bending test according to Norm DIN EN ISO 5173:2009.

The samples for bending test were cut in the dimensions of 20mm x 150 mm for all process variants conducted during the present work. All samples achieved a 170° angle from bending tests without a sign of crack initiation. Tests were conducted on the base material, the conventional SRBT, and the new S^{3}BT processes. Latter ones were evaluated in both directions that including bending over the top side and with a second testing over the bottom side. The welding parameters were for conventional SRBT 300 mm/min with 6 and 7 mm probe, and for the S^{3}BT-SLS process variant with a welding speed of a 1800 mm/min and in addition the S^{3}BT-SUS process variant with 1850, 2000, 2500 and 2950 mm/min. The tested welds are in agreement of the Welds 2 and 4 to 9 of Table 5. An example of the tested bending specimens is shown in Figure B.5.

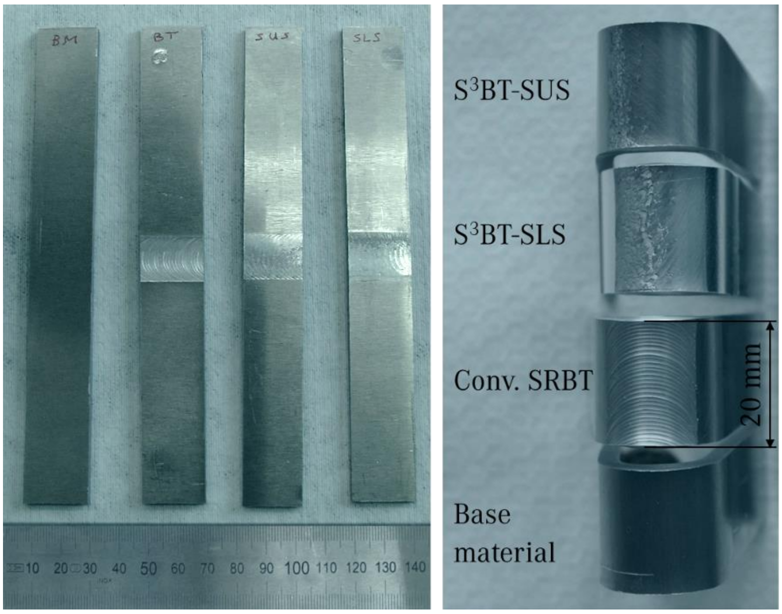

Figure B.5. Example of samples before and after the bending tests.

Hardness

Micro hardness was evaluated across the SZ, the TMAZ and the HAZ on a Zwick/Roell ZHV hardness testing machine. For this purpose, each weld was prepared as a macro section and then tested with a load of 200 gf (HV0.2) was applied for 10 s. The hardness profiles were obtained at three levels of the cross section along lines of 35 mm length. One line was defined at 500 μm from the top side (Top), one in the middle of the sample and one at 500 μm from the bottom side (Bottom). The distance between the indentations was chosen to be 650 μm.

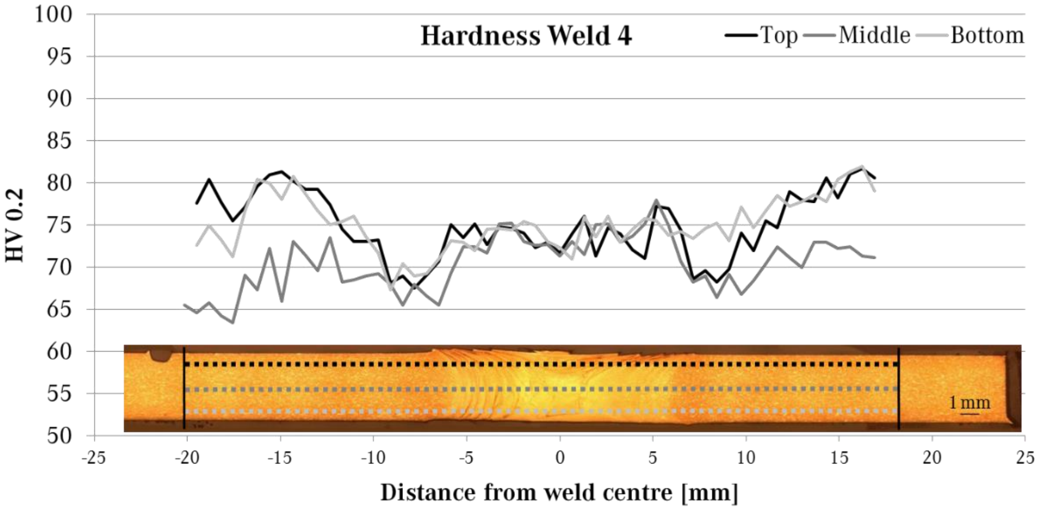

Figure B.6. Hardness line of SRBT weld with welding speed of 300 mm/min.

Micro hardness was tested on cross sections of the welds 4, 5 and 6 of Table 5 shortly after the welding procedure to avoid natural aging of the material. The hardness results for the conventional SRBT weld with a welding velocity of 300 mm/min are presented in Figure B.6. The W-shape hardness pattern across the welding zone which is commonly observed in aluminium alloy welds in FSW, can be found in the evaluated hardness lines. Typically for this alloy is a shelf, which seemed to correlate with the tool shoulder diameter. The line in shape of a shelf mentioned by Mishra et al. [16] might be visible for the middle line, but is not as much distinct as mentioned in the literature.

Wan et al. reported increasing microhardness in correlation with increasing welding speed between 10 to 200 mm/min [44]. The hardness lines of the S^3BT process variants are given in the graphs of the Figure B.7 and Figure B.8. Especially in the graph of Figure B.8 the increase of hardness can be observed. The W-shape pattern is not as much clearly visible, since the drop of hardness is reduced. Interesting to observe is that the drop of hardness occurs far away from the welding zone. Especially on the AS of the weld the hardness drops at 11 or 12 mm away from the centre of the weld. This is compared to the literature a new behaviour.

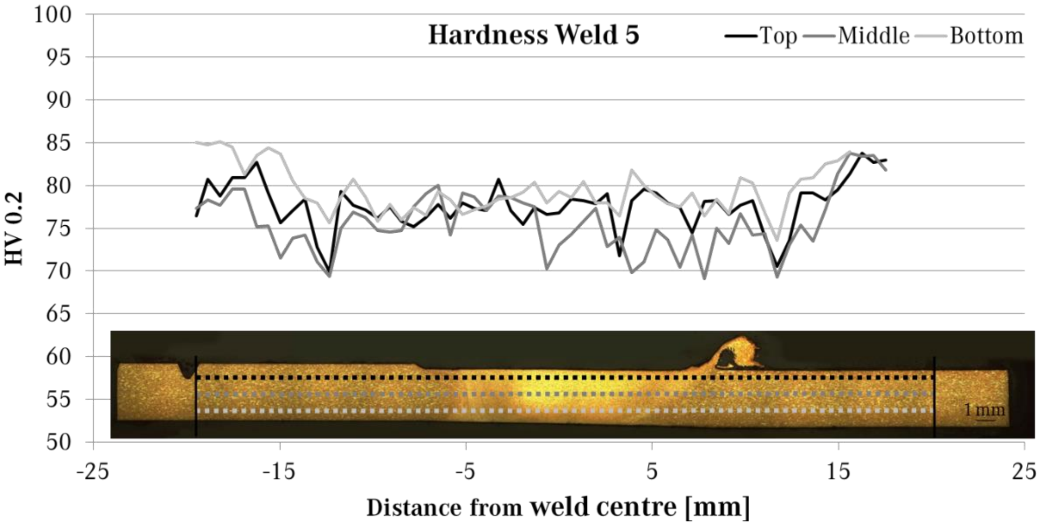

Figure B.7. Hardness measurements of S³BT-SLS weld with welding speed of 1800 mm/min.

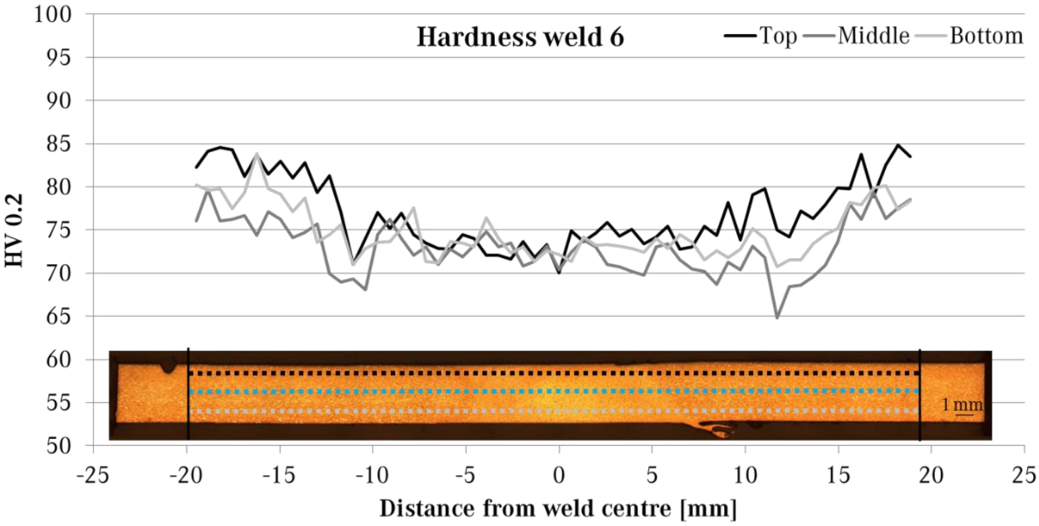

Figure B.8. Hardness measurement of S³BT-SUS weld with welding velocity of 1850 mm /min.

Average values of the measured lines are given in the graph of Figure B.9. While the hardness in the mid-level of the welds of the new processes could be increased in comparison to the base material value, a reduced hardness can be found in top and bottom level region. Overall the new process variants have increased values compared to the conventional SRBT. The relationship between line-energy and hardness is interesting to observe: While the conventional SRBT process is conducted with a line-energy of 460 kJ/m, the line energy of the S³BT process variants is lower. The S³BT-SLS process was done with a line energy of 164 kJ/m, and with the stationary upper shoulder configuration with even lower 134 kJ/m. If a relationship between heat input and hardness values is assumed, the conventional SRBT weld was produced at elevated temperature, while the S³BT-SLS process variant appeared to apply better heat condition. Even though the energy input was further reduced with the S³BT-SUS process variant, the hardness values shows are not increased in comparison to the S³BT-SLS process variant. As the graph of Figure B.10 shows the highest difference is in the hardness values of the lower shoulder region.

A reason for the different values of S^3BT process variants could be the unequally applied heat source. There is a temperature difference between the S^3BT-SUS and –SLS, since the heat sink of the upper shoulder to the spindle is higher than the heat sink to the convective cooling by air of the lower shoulder. The process with the heat source closer to the greater heat sink, as it is the case for the rotating upper shoulder, will show a smaller difference between the temperatures of the two shoulders. Furthermore, the bearings of the stationary lower shoulder produce frictional heat and the convective cooling is reduced due to no rotational speed on the outside surfaces. This adds to the smaller temperature difference between lower shoulder with the bearings and the rotating upper part in the S^3BT-SLS process in comparison to the differences S^3BT-SUS process. The upper shoulder at the S^3BT-SUS process is stationary; limited heat is produced due to friction on the surface of the material. While the lower shoulder produces heat and also convectional cooling due to its rotational and translational speed. Yet, the shoulder heat up to elevated temperature during the process. The elevated temperatures of the rotating lower shoulder lead to degradation of the material which is comparable to the conventional SRBT process variant.

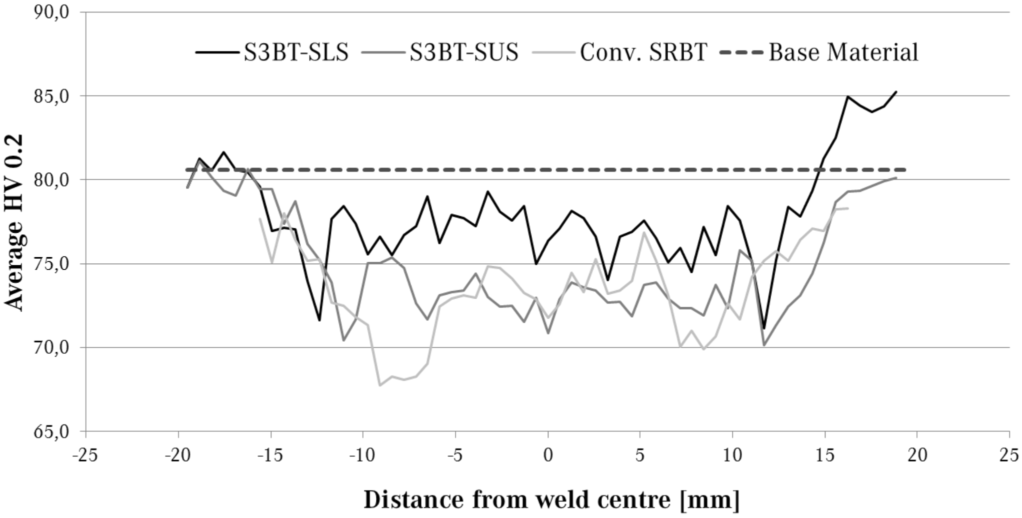

Figure B.9. Average hardness measurements of the process variants.

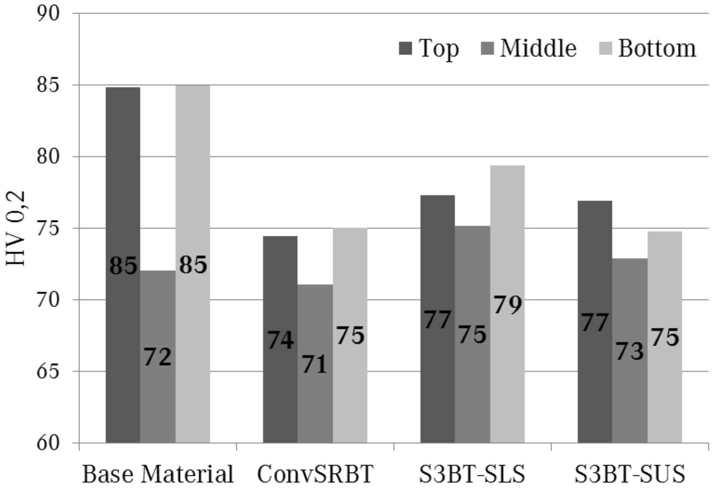

Figure B.10. Average of hardness in different height levels and process variants.

C. Tables

Technical Details of the Welding Spindle

Table C.1. Technical data and specifications of new welding spindle

Max. rotation per minute	3000 rpm
Max. gap force	4 kN
Max. axial path	6 mm
Power	5.5 kW
Max. torque	50 Nm (@ 300 rpm)
Weight	110 kg
Dimensions	640 mm x 500 mm x 240 mm

Simulation results based on viscosity model with $sinh^{-1}$

Table C.2. Results from CFD simulation with viscosity model based on $sinh^{-1}$ with the upper limit of the viscosity set to 10^9 and the symmetric probe geometry. The conventional self-reacting bobbin tool (SRBT) equipped with 6 and 7 mm probe, the semi-stationary shoulder bobbin tool with the stationary upper shoulder configuration (S^{3}BT-SUS), the stationary shoulder bobbin tool with the stepped probe design (SSBT-stepped) and straight probe design (SSBT-straight)

	Welding speed [mm/s]	$\frac{\dot{V}_1}{\dot{V}_3}$	$\frac{\dot{V}_2}{\dot{V}_3}$	$\frac{\dot{E}_{kin2}}{\dot{E}_{kin3}}$ $R_{Rot}KE$	$\frac{\dot{E}_{kin2}}{\dot{E}_{kin2Ref}}$ $R_{Ref}KE$
S^{3}BT-SUS	2950	37%	63%	51%	236%
S^{3}BT-SUS	2500	33%	67%	55%	216%
S^{3}BT-SUS	2000	32%	68%	56%	119%
S^{3}BT-SUS	1850	31%	69%	56%	95%
SRBT 6mm	300	5%	95%	91%	100%
SRBT 7mm	300	4%	96%	94%	268%
SSBT-stepped	100	3%	97%	93%	16%
SSBT-straight	100	18%	82%	77%	1%